NAVAL POSTGRADUATE SCHOOL

MONTEREY, CALIFORNIA

DISSERTATION

ECHO STATISTICS OF AGGREGATIONS OF SCATTERERS IN A RANDOM WAVEGUIDE: APPLICATION TO BIOLOGIC SONAR CLUTTER

by

Benjamin A. Jones

September 2012

Dissertation Supervisors: John A. Colosi
Timothy K. Stanton

Approved for public release; distribution is unlimited

Reissued 10 Jan 2014 to remove revision marks.

THIS PAGE INTENTIONALLY LEFT BLANK

REPORT DOCUMENTATION PAGE			Form Approved OMB No. 0704–0188
Public reporting burden for this collection of information is estimated to average 1 hour per response, including the time for reviewing instruction, searching existing data sources, gathering and maintaining the data needed, and completing and reviewing the collection of information. Send comments regarding this burden estimate or any other aspect of this collection of information, including suggestions for reducing this burden, to Washington headquarters Services, Directorate for Information Operations and Reports, 1215 Jefferson Davis Highway, Suite 1204, Arlington, VA 22202–4302, and to the Office of Management and Budget, Paperwork Reduction Project (0704–0188) Washington DC 20503.			
1. AGENCY USE ONLY ***(Leave blank)***	**2. REPORT DATE** September 2012	**3. REPORT TYPE AND DATES COVERED** Dissertation	
4. TITLE AND SUBTITLE: Echo Statistics of Aggregations of Scatterers in a Random Waveguide: Application to Biologic Sonar Clutter		**5. FUNDING NUMBERS**	
6. AUTHOR(S) Benjamin A. Jones			
7. PERFORMING ORGANIZATION NAME(S) AND ADDRESS(ES) Naval Postgraduate School Monterey, CA 93943–5000		**8. PERFORMING ORGANIZATION REPORT NUMBER**	
9. SPONSORING / MONITORING AGENCY NAME(S) AND ADDRESS(ES) N/A		**10. SPONSORING / MONITORING AGENCY REPORT NUMBER**	
11. SUPPLEMENTARY NOTES The views expressed in this thesis are those of the author and do not reflect the official policy or position of the Department of Defense or the U.S. Government. IRB Protocol number _____N/A_____.			
12a. DISTRIBUTION / AVAILABILITY STATEMENT Approved for public release; distribution is unlimited		**12b. DISTRIBUTION CODE**	

13. ABSTRACT (maximum 200 words)

Reverberation, echoes from the water column boundaries and non-target scatterers within the water column, often limits active sonar system performance. Fish can constitute a significant portion of sonar reverberation under certain conditions, such as a horizontally looking sonar system operating at mid-frequencies (1–9 kilohertz), where scattering by fish with resonant gas-filled swimbladders can dominate over bottom or surface reverberation. This study examines the contributions of various elements of an active sonar system ensonifying aggregations of water column scatterers to determine relative contributions of various physical factors to producing target-like echoes (i.e., clutter). Elements of the system that are considered include 1) a shallow-water waveguide, 2) a stochastic, range-dependent sound-speed profile, 3) a directional acoustic source, 4) a variable scattering response, and 5) an extended scattering volume. Numerical modeling predictions are compared with analytical models and observations. Modeling is validated with long-range, broadband (1.5 to 5 kilohertz) sonar measurements of aggregations of fish in the Gulf of Maine. Key results include the classification of a mixed assemblage of swimbladder-bearing fish, with target-sized aggregations, that produce a significant number of echoes that are at least 15 decibels above background levels. These sparsely distributed scatterers produce highly non-Rayleigh distributions of echo magnitudes that are well-modeled by a computationally efficient, physics-based model.

14. SUBJECT TERMS Active sonar, shallow-water acoustics, waveguide acoustics, echo statistics, sonar clutter, active sonar reverberation, bio-clutter, scintillation index, K distribution, two-way parabolic equation, phasor summation, fish aggregations, mixed assemblages of fish	**15. NUMBER OF PAGES** 167
	16. PRICE CODE

17. SECURITY CLASSIFICATION OF REPORT	**18. SECURITY CLASSIFICATION OF THIS PAGE**	**19. SECURITY CLASSIFICATION OF ABSTRACT**	**20. LIMITATION OF ABSTRACT**
Unclassified	Unclassified	Unclassified	UU

NSN 7540–01–280–5500 Standard Form 298 (Rev. 2–89)
Prescribed by ANSI Std. 239–18

THIS PAGE INTENTIONALLY LEFT BLANK

Approved for public release; distribution is unlimited

ECHO STATISTICS OF AGGREGATIONS OF SCATTERERS IN A RANDOM WAVEGUIDE: APPLICATION TO BIOLOGIC SONAR CLUTTER

Benjamin A. Jones
Lieutenant Commander, United States Navy
B.S., United States Naval Academy, 1997
M.S., Massachusetts Institute of Technology, 2006

Submitted in partial fulfillment of the
requirements for the degree of

DOCTOR OF PHILOSOPHY IN PHYSICAL OCEANOGRAPHY

from the

NAVAL POSTGRADUATE SCHOOL
September 2012

Author: _____
Benjamin A. Jones

Approved by:

_____	_____
John Colosi Professor of Oceanography Dissertation Co-Supervisor/ Committee Chair	Timothy K. Stanton Senior Scientist Woods Hole Oceanographic Institution Dissertation Co-Supervisor
_____	_____
Ching-Sang Chiu Distinguished Professor of Oceanography	Lawrence Ziomek Professor of Electrical and Computer Engineering

_____
D. Benjamin Reeder
Research Associate Professor of Oceanography

Approved by: _____
Mary Batteen, Chair, Department of Oceanography

Approved by: _____
Douglas Moses, Vice Provost for Academic Affairs

THIS PAGE INTENTIONALLY LEFT BLANK

ABSTRACT

Reverberation, echoes from the water column boundaries and non-target scatterers within the water column, often limits active sonar system performance. Fish can constitute a significant portion of sonar reverberation under certain conditions, such as a horizontally looking sonar system operating at mid-frequencies (1–9 kilohertz), where scattering by fish with resonant gas-filled swimbladders can dominate over bottom or surface reverberation. This study examines the contributions of various elements of an active sonar system ensonifying aggregations of water column scatterers to determine relative contributions of various physical factors to producing target-like echoes (i.e., clutter). Elements of the system that are considered include 1) a shallow-water waveguide, 2) a stochastic, range-dependent sound-speed profile, 3) a directional acoustic source, 4) a variable scattering response, and 5) an extended scattering volume. Numerical modeling predictions are compared with analytical models and observations. Modeling is validated with long-range, broadband (1.5 to 5 kilohertz) sonar measurements of aggregations of fish in the Gulf of Maine. Key results include the classification of a mixed assemblage of swimbladder-bearing fish, with target-sized aggregations, that produce a significant number of echoes that are at least 15 decibels above background levels. These sparsely distributed scatterers produce highly non-Rayleigh distributions of echo magnitudes that are well-modeled by a computationally efficient, physics-based model.

THIS PAGE INTENTIONALLY LEFT BLANK

TABLE OF CONTENTS

I. INTRODUCTION 1
A. DEFINITIONS AND KEY CONCEPTS 1
B. BACKGROUND 2
1. Early Acoustic Measurements of Fish 2
2. Major Sources of Variability in Acoustic Scattering by Fish 2
3. Fish as a Source of Sonar Clutter 4
4. Acoustic Scattering in an Waveguide 5
C. NAVY RELEVANCE 6
D. SUMMARY OF RELATED WORK AND DISSERTATION OVERVIEW 7

II. MODELING ECHO STATISTICS OF AGGREGATIONS OF SCATTERERS IN THE WATER COLUMN OF A RANDOM, OCEANIC WAVEGUIDE 11
A. INTRODUCTION 11
B. PROBABILITY DENSITY FUNCTIONS ASSOCIATED WITH ACOUSTIC BACKSCATTER 14
1. Rayleigh Distribution 14
2. Exponential Distribution 15
3. K Distribution 16
4. Chu-Stanton Theory 16
C. NUMERICAL METHODS 18
1. Two-way Parabolic Equation Model 18
2. Internal Wave Model 21
3. Phasor Summation Method for Generating Echo PDFs 23
4. Validation of Models using Direct Path Geometry 24
D. SIMULATIONS OF ECHOES FROM A SINGLE SCATTERER IN A DETERMINISTIC WAVEGUIDE 25
1. Delta Function Scatterer Ensonified by an Omnidirectional Source in a Constant Sound-Speed Environment (Case A, Table 2.3) 25
2. Effects of a Depth-Dependent Sound-Speed Profile (Case C, Table 2.3) 26
3. Effects of a Vertically Directional Beampattern (Case D, Table 2.3) 27
4. Scatterer of Varying Spatial Extent with a Variable Scattering Response (Rayleigh Scatterer) (Case B, Table 2.3) 28
E. SIMULATIONS OF ECHOES FROM SCATTERERS IN A RANDOM WAVEGUIDE 30
1. Single Scatterer in a Directional Beampattern in the Vertical Plane (Case E, Table 2.3) 31
2. Multiple Scatterers in a Directional Beampattern in the Vertical Plane (Case E, Table 2.3) 31

F. SIMULATION OF ECHOES FROM SCATTERERS IN A THIN LAYER WITHIN A RANDOM WAVEGUIDE 32
1. Single Scatterer in a Vertically Directional Beampattern (Case F, Table 2.3) 33
2. Effects of an Azimuthally Directional Beampattern (Case G, Table 2.3) 35
3. Extended, Finite-Sized Rayleigh Scatterers (Case H, Table 2.3) 36
G. DISCUSSION AND CONCLUSIONS 37
1. Effects of a Shallow Waveguide 37
2. Effects of a Random Waveguide 38
3. Effects of a Directional Source 39
4. Extended Scatterers with a Variable Scattering Response in a Waveguide 41
5. Modeling Echo Envelopes in an Acoustic Waveguide 42
III. CLASSIFICATION AND STATISTICS OF LONG-RANGE, MID-FREQUENCY SONAR MEASUREMENTS OF AGGREGATIONS OF FISH 63
A. INTRODUCTION 63
B. 2011 GULF OF MAINE EXPERIMENT 65
1. Long-Range, Horizontally Looking Sonar System (NRL) 66
2. Downward-Looking Narrowband Echo Sounder (NOAA-NMFS) 66
3. Biological Sampling (NOAA-NMFS) 67
4. Water Column Sampling (NOAA-NMFS) 67
C. REVERBERATION MODELS 67
1. Sonar Simulation Toolset 68
2. Two-Way Parabolic Equation Model 68
D. RESULTS 69
1. Characteristics of Fish Schools Derived from Downward-Looking Echo-Sounder Measurements 70
2. Biologic Sampling 71
3. Classification of Broadband, Long-Range Echoes 72
4. Echo Statistics 76
E. DISCUSSION 81
1. Echo Classification 81
2. Echo Statistics 83
F. CONCLUSION 84
IV. CONCLUSION 109
A. MODELING AND ANALYSIS 109
B. MEASUREMENTS 111
C. CONTRIBUTIONS OF THIS DISSERTATION 112
1. Contributions to the Ocean Acoustic Community 112
2. Contributions to the United States Navy Sonar Community 112
D. RECOMMENDATIONS FOR FUTURE WORK 113

APPENDIX A: DERIVATION OF THE SPLIT-STEP PADÉ SOLUTION TO THE PARABOLIC EQUATION 115

APPENDIX B: COMPARISON OF TWO DERIVATIVES OF THE RANGE-DEPENDENT ACOUSTIC MODEL (RAM): PE 5.5 AND MRAMGEO 119

APPENDIX C: BENCHMARKING THE TWO-WAY PARABOLIC EQUATION MODEL WITH LLOYD'S MIRROR PATTERN 123

APPENDIX D: GENERATION AND STATISTICAL ANALYSIS OF PROBABILITY DENSITY FUNCTIONS OF ECHO ENVELOPES 127

APPENDIX E: SCATTERING MODEL FOR AGGREGATIONS OF FISH 129

APPENDIX F: ACOUSTIC SCATTERING BY GAS-FILLED-SWIMBLADDER BEARING FISH 135

LIST OF REFERENCES 139

INITIAL DISTRIBUTION LIST 145

THIS PAGE INTENTIONALLY LEFT BLANK

LIST OF FIGURES

Figure 2.1 Benchmark test of parabolic equation starter field modeling a circular piston ($ka = 32.06$). 46

Figure 2.2 Munk sound-speed profile fit to observed data, with and without internal waves....47

Figure 2.3 Observed water column profiles from 2010 Gulf of Maine cruise. 48

Figure 2.4 Predicted sound-speed perturbation due to diffuse, broadband internal waves in shallow water using an empirically validated model.[63] 48

Figure 2.5 Predicted echo PDFs of various numbers of scatterers, each with a Rayleigh distributed scattering amplitude, randomly located in the main lobe of a directional sonar beam (3 kHz source with a 5° beamwidth) in a direct path geometry. 49

Figure 2.6 Predicted transmission loss from a 3 kHz source in an oceanic waveguide with varying levels of complexity....50

Figure 2.7 Predicted PDFs associated with a 3 kHz *omnidirectional source* at a depth of 50 m ensonifying a single scatterer randomly located in depth at a range of 1000 m in a waveguide with a *constant sound-speed profile*....51

Figure 2.8 Predicted PDFs associated with a 3 kHz *omnidirectional source* at a depth of 50 m ensonifying a single scatterer randomly located in depth at a range of 1000 m (left two panels) and 3500 m (right two panels) in a waveguide with a *canonical Munk sound-speed profile*. 52

Figure 2.9 Predicted echo PDFs associated with a 3 kHz *directional source* at a depth of 50 m ensonifying a single scatterer located *azimuthally on axis* and randomly in depth at various ranges in a waveguide with a *canonical Munk sound-speed profile*....53

Figure 2.10 Predicted echo PDFs associated with a 3 kHz omnidirectional source at a depth of 50 m ensonifying a single spherical Rayleigh scatterer of various radii, r_v....54

Figure 2.11 Predicted echo PDFs associated with a 3 kHz *directional source* at a depth of 50 m ensonifying a single scatterer located *azimuthally on axis* and randomly in depth at various ranges in a *random waveguide* with a canonical *Munk sound-speed profile* perturbed by diffuse internal waves.....55

Figure 2.12 Predicted echo PDFs associated with a 3 kHz *directional source* at a depth of 50 m ensonifying various numbers of scatterers. 56

Figure 2.13 Predicted transmission loss from a 3 kHz directional source located at 10 m depth in a random waveguide. 57

Figure 2.14 Predicted normalized intensity variance (scintillation index, SI) associated with a 3 kHz directional source at 10 m depth ensonifying a single scatterer randomly located azimuthally on axis in a thin layer in a random oceanic waveguide. 58

Figure 2.15 Predicted echo PDFs associated with a 3 kHz directional source at a depth of 10 m ensonifying a single scatterer randomly located within the full

180° beampattern, azimuthally, and in a shallow thin layer vertically (10–20 m), in a random oceanic waveguide. 59
Figure 2.16 Predicted echo PDFs associated with a 3 kHz directional source at a depth of 10 m ensonifying various numbers of scatterers with *a constant scattering response*. 60
Figure 2.17 Predicted echo PDFs associated with a 3 kHz directional source at a depth of 10 m ensonifying various numbers of *extended scatterers* with a distribution of magnitudes of scattering responses that are *Rayleigh distributed*. 61
Figure 2.18 K distribution shape parameter, α_k, as a function of the number of scatterers ensonified by a directional beam in a shallow water oceanic waveguide. 62
Figure 3.1 Map of the Gulf of Maine showing bathymetry and cruise tracks of FRV *Delaware II* from 11th-15th of September 2011, (white line) and RV *Oceanus* from 15:30 – 19:50 local on the 11th of September 2011 (red line). 90
Figure 3.2 Deployed configuration of NRL long-range, horizontal-looking sonar system. 91
Figure 3.3 Cartoon illustrating the split-window normalization technique (from Fialkowski et al., 2010)[2]. 91
Figure 3.4 Trawl tows conducted from FRV *Delaware II* between the 11th and 15th of September 2011. 92
Figure 3.5 Map of CTD cast stations from FRV *Delaware II* during times of 0:00 to 11:59 local (white) and 12:00 to 23:59 local (black) between the 11th and 15th of September 2011. The red line is the track of the RV *Oceanus* on the 11th of September 2011. 93
Figure 3.6 Temperature, salinity, and sound-speed profiles (left to right) derived from CTD casts taken from FRV *Delaware II* during times of 12:00 to 23:59 local (see Figure 3.5) between the 11th and the 15th of September 2011. 94
Figure 3.7 Normalized histograms of fish school characteristics (mean depth – top panel, length – middle panel, mean thickness – bottom panel) derived from *day* measurements of a downward-looking, multi-frequency echosounder from the FRV *Delaware II*. 95
Figure 3.8 Normalized histograms of fish school characteristics (mean depth – top panel, length – middle panel, mean thickness – bottom panel) derived from *night* measurements of a downward-looking, multi-frequency echosounder from the FRV *Delaware II*. 96
Figure 3.9 Normalized histograms of densities of schools of Atlantic herring derived from daytime (white) and nighttime (black) measurements of a downward-looking, multi-frequency echosounder from the FRV *Delaware II*. 97
Figure 3.10 Catch density and length distribution of three species of fish caught during *day* trawls from FRV *Delaware II* 98
Figure 3.11 Catch density and length distribution of three species of fish caught during *night* trawls from FRV *Delaware II*.....99

Figure 3.12 Mixed assemblage model (red) fit to observed spectra (black) for four sets of data.....100
Figure 3.13 Comparison between observed reverberation level (black) and SST predictions averaged over forward beams (top panel) and aft beams (lower panel).....101
Figure 3.14 Water column profiles associated with observed mean profile (thick black curves, Figure 3.6) from Franklin Swell area in the Gulf of Maine from September 2011. 102
Figure 3.15 Transmission Loss for four realizations of internal wave fields. 103
Figure 3.16 Sample comparison between an acoustic measurement by a long-range, horizontal-looking sonar (left panels) and a model prediction (right panels). 104
Figure 3.17 Theoretical beampatterns in terms of pressure envelope at 3.75 kHz (black) for beam 25 of a shaded 32-element HLA (top panel) and a shaded 10-element VLA (bottom panel). 105
Figure 3.18 Comparison of observed echo magnitude PDFs (black asterisks) for scatterers at various ranges from Sets C2, D and E, with predictions by numerical phasor summation mehtod (red solid), and the K distribution (blue-dashed).....106
Figure 3.19 Comparison of observed echo magnitude PDFs (black asterisks) for scatterers in a single range bin (≈ 4018.2 to 4518.2 m) from Sets C2, D and E, with a mixture model using a two-part Rayleigh mixture and no beampattern effects (dashed), and a phasor summation calculation including beampattern effects and no mixture (red solid). 107
Figure B.1 Comparison between two implementations of RAM, PE 5.5 (left panels) and MRAMGEO (right panels). 121
Figure C.1 Two-way PE predictions of Lloyd's mirror effect for a vertical receiver co-located in range with an omnidirectional source (red) compared with theory (black). 126
Figure E.1 Kullback-Leibler distances comparing a Rayleigh PDF with normalized echo envelope PDFs from numerical simulations, where the number of scatterers within a sonar resolution cell is varied from 1 to 50. 133
Figure E.2 Mapping observed morphology to scattering centers. 134

THIS PAGE INTENTIONALLY LEFT BLANK

LIST OF TABLES

Table 2.1. Shallow water internal wave modeling parameters. 43
Table 2.2. Model parameters simulating direct path geometry.....43
Table 2.3. Key modeling parameters used in numerical simulations. 44
Table 2.4 Predicted echo envelope PDFs for various cases of a monostatic sonar system with *N* scatterers positioned randomly in a saturated pressure field....45
Table 3.1 Parameters of signals analyzed in this study including signal type, bandwidth, *W*, minimum frequency, f_{min}, maximum frequency, f_{max}, and pulse length, T_P 86
Table 3.2 Long-range acoustic data sets defined by time of transmission and range of receiver beams from which data was drawn.....86
Table 3.3 Resonant swimbladder scattering model parameters. 87
Table 3.4 Relative densities of various species of fish used in mixed-assemblage spectral modeling of echoes from aggregations of fish. 87
Table 3.5 Parameters used in reverberation calculations using the Sonar Simulator Toolset (SST). 88
Table 3.6 Two-way parabolic equation modeling parameters. 89
Table B.1 Model parameters for two-way PE 5.5 and MRAMGEO comparison. 120
Table C.1 Model parameters for two-way parabolic equation simulation of Lloyd's mirror effect. 125

THIS PAGE INTENTIONALLY LEFT BLANK

LIST OF ACRONYMS AND ABBREVIATIONS

2D	two dimensional
3D	three dimensional
ACB	Advanced Capability Build
CASE	Common Acoustic Simulator Environment
CASS	Comprehensive Acoustic System Simulation
CLT	central limit theorem
cm	centimeter
cph	cycles per hour
CTD	conductivity, temperature and depth
dB	decibel
FRV	Fisheries Research Vessel
FSS	Fish Scattering Strength algorithm
GRAB	Gaussian Ray Bundle
HLA	horizontal line array
Hz	hertz
IW	internal waves
kHz	kilohertz
km	kilometer
kn	knot
LFM	linear frequency modulated
m	meter
MFA	mid-frequency active
N	north
NAVAIR	Naval Air Systems Command
NAVSEA	Naval Sea Systems Command
NOAA-NMFS	National Oceanic and Atmospheric Association's National Marine Fisheries Service
NRL	Naval Research Laboratory
NSPE	Navy Standard Parabolic Equation (NSPE)
Pa	Pascal

PDF	probability density function
PE	parabolic equation
PS	phasor summation
rad	radians
RAM	Range-dependent Acoustic Model
rms	root mean square
RV	Research Vessel
s	second
SAST	Surface Anti-Submarine Warfare Synthetic Trainer
SBE	Seabird Electronics
SI	scintillation index
SNR	signal-to-noise ratio
SSP	sound-speed profile
SST	Sonar Simulation Toolset
U.S.	United States
VLA	vertical line array
W	west
WHOI	Woods Hole Oceanographic Institution

ACKNOWLEDGMENTS

The research presented here would not have been possible without the support of leadership within the Naval Oceanography community, in particular CAPT John O'Hara and CDR Greg Ireton, and the financial support of the Oceanographer of the Navy and the Office of Naval Research.

The decision to pursue a future in scientific research while balancing a naval career has been greatly influenced by the enthusiasm and inspiring mentorship of my co-advisor Dr. Tim K. Stanton (WHOI), to whom I am supremely grateful. Additionally, I have had the great fortune of being co-advised by Dr. John Colosi, who is a role model for how to enjoy both science and life. I am further grateful to the members of my dissertation committee, Dr. Ching-Sang Chiu, Dr. Larry Ziomek, and Dr. D. Ben Reeder, who have all provided thoughtful guidance and reviews of this work. I owe a special thanks to the members of the Ocean Acoustic Laboratory at the Naval Postgraduate School, especially Dr. Tarun Chandrayadula for helping guide me through the complexities of acoustic signal processing, and Mr. Chris Miller for his support and expertise on all laboratory equipment. Acquisition of the long-range acoustic data presented in this research was a collaborative effort of a great team of researchers from the Naval Research Laboratory led by Dr. Roger Gauss. I am appreciative of their ongoing support, especially that of Mr. Joe Fialkowski, who has been undeterred by my barrage of questions and requests for data. Further thanks to Dr. J. Mike Jech of the National Marine Fisheries Service who provided fish observations and water column samples presented here and to Dr. Tom Weber who graciously provided multibeam sonar observations of fish school morphology for use in this research.

This effort would not have been possible or enjoyable without the love and encouragement of my spouse, Sylvie, and daughters, Melody and Mabel. Also, I am indebted to my parents-in-law, Ron and Sue Rusay, who have been a pillar of support for our family. Finally, I would not have begun this endeavor without two traits, instilled at a young age: a curiosity in science and an appreciation of a conscientiously accomplished task, no matter how large or small. Thank you, Mom and Dad.

THIS PAGE INTENTIONALLY LEFT BLANK

I. INTRODUCTION

A. DEFINITIONS AND KEY CONCEPTS

For an active sonar system, reverberation is the sum of all sound scattered from inhomogeneities within an ensonified volume and its boundaries as measured at a receiver.[1] Inhomogeneities are characterized as regions of varying material properties (i.e., sound speed and density). Clutter, a closely related attribute of an active sonar system, is the general term for non-target echoes that generate false alarms in a sonar system after processing and normalization techniques are performed on the received signal. Reverberation can be largely separated into three major classes: sea-surface reverberation, bottom reverberation, and volume reverberation. While sea-surface and bottom reverberation include boundary or near-boundary scattering, volume reverberation includes scattering by all inhomogeneities within the water column away from the boundaries. Examples of scatterers in the ocean that can contribute to volume reverberation include air bubbles, zooplankton, and schools of fish.

Reverberation is further classified into two distinct types based on the spatial properties of the scatterer. The first type is termed distributed which includes many closely spaced scatterers which produce indistinguishable, interfering echoes (e.g., rippled seabed, large aggregations of fish or phytoplankton). The second type is termed discrete which refers to high intensity echoes from non-target features that may be individually resolved by the sonar system (e.g., ship wrecks, sea mounts, compact aggregations of fish). Importantly, clutter can arise from either discrete features with one or more target-like characteristics (e.g., echo duration or amplitude) or distributed features with a non-Rayleigh distribution of echo magnitudes[2] (i.e., a higher proportion of high magnitude echoes than expected from Rayleigh-distributed reverberation).

B. BACKGROUND

1. Early Acoustic Measurements of Fish

Several post-WWII studies determined that fish could be measured with active sonar systems,[3,4] and subsequent studies beginning in the mid-1960s provided evidence that fish could be a significant source of volume reverberation for long-range, active sonar systems.[5–7] Early acoustic measurements of fish identified several key characteristics of this type of biologic reverberation. Significant shifts in the frequency of the maximum scattering strength, related to diurnal vertical migration of swimbladder-bearing fish, was observed in the acoustic measurements.[8] Variability in the echo magnitudes at a given frequency was also observed and correctly hypothesized to be due to a combination of fusion and dispersion of fish shoals and the depth-dependent scattering response of the fish.[6] Additionally, it was found that, under certain shallow water circumstances, volume scattering from fish could become the dominate mechanism contributing to reverberation at medium to long ranges. This effect is due to the selective attenuation of steeper angle energy due to bottom interactions allowing the shallow angle energy, which interacts most strongly with scatterers in the water column such as fish, to dominate the reverberation.[6]

2. Major Sources of Variability in Acoustic Scattering by Fish

In the ensuing decades a considerable body of literature was published on the various sources of variability in acoustic scattering by fish and fish aggregations. Of first-order importance are the depth-dependent frequency response of scattering by swimbladder-bearing fish and aggregation characteristics. Gaseous-swimbladder-bearing fish are of specific interest to the Navy as their swimbladders can be resonant in the frequency band of mid-frequency active (MFA) systems (i.e., 1–9 kilohertz, kHz) as was shown in early broadband studies using explosive charges that identified fish resonances below 5 kHz.[9,10] The depth-dependence of the resonant acoustic response of swimbladdered fish has also been observed experimentally for individual fish. For example, Sand and Hawkins observed a change in the resonance peak for live cod of approximately 800 hertz (Hz) for the depth change of 20 meters.[11] Additionally, several

in-situ observations have confirmed that the volume scattering strength and corresponding resonance peaks of large layers of fish vary significantly with depth.[12–14] This depth-dependent scattering by the swimbladder organ has been analytically modeled as a gas-filled spherical shell with elastic properties by Andreeva[15] and with viscous properties by Love.[16] The widely-used Love model has been experimentally validated by volume scattering measurements of aggregations of fish.[13,14,17]

The study of the aggregation morphology of fish schools is the second important area related to acoustic scattering variability. Two recent studies have quantified the variability in size and shape of fish schools. Observations by Gerlotto and Paramo of hundreds of fish schools in the tropical Atlantic Ocean using a 455 kHz multibeam sonar have shown non-uniform distributions of fish that can include large vacuoles within a generally amorphous external shape.[18] Through multiple observations of a single fish school by a 400 kHz multibeam sonar Weber et al. have further shown that aggregations can have strong temporal variability in size and shape.[19] In this study significant fusion, fragmentation, and dispersion of a fish school are observed over the period of approximately one hour.

In order to connect fish aggregation morphology to variability in the acoustic scattering response, one must consider the sonar resolution cell (i.e., the acoustic sample volume of the ensonifying system). The sonar resolution cell defines an effective volume that contains any number of scatterers that significantly contribute to an individual echo. This volume is a function of the sonar beamwidth, the range to the scattering volume, and parameters of the waveform which dictate the range resolution of the sonar. For a narrow beam ensonifying a large, patchy aggregation of fish (large when compared with the sonar resolution cell) the reverberation level will vary as the sonar beam sweeps across regions of varying density of fish. This case, of a sonar beam ensonifying patchy aggregations, has been shown to have significant effects on the statistics of the echo magnitudes[20].

In addition to these first-order effects, other factors contributing to variability in scattering by fish schools include Doppler effects and collective resonance for swimbladder bearing fish. Doppler effects due to relative motion of fish within a school

(head-tail aspect) and body/tail motion (side aspect) were observed by Holliday resulting in Doppler shifts of a 30 kHz continuous wave pulse on the order of 10–30 Hz.[21] Diachok observed a significant decrease in the resonance frequency over theoretical values for individual fish when sardines were observed in densely packed schools.[22] However, other studies have shown good agreement for resonance of fish in aggregations with theoretical models for individual fish.[17,23,24] The importance of capturing these effects is likely determined by the specific behavior of the fish being modeled.

3. Fish as a Source of Sonar Clutter

A statistical definition of clutter is given by Abraham who states that clutter is the presence of an inordinate number of false alarms compared to that expected from Rayleigh-distributed reverberation envelopes[25] (i.e., the magnitude of the complex pressure at the receiver). A growing body of evidence suggests that aggregations of fish can be a significant source of clutter for active sonar systems.[20,26,27] This is due, in large part, to the fact that scattering from patches of fish by a directional sonar beam can induce highly non-Rayleigh echo statistics.[20] These data highlight the importance of developing an understanding of the physical basis for the statistical distributions of echo magnitudes of active sonar clutter. Such work by Gelb et al. to broadly classify clutter[28] and by Chu and Stanton to analytically model echo statistics from volume reverberation[29] has recently been conducted. The former study statistically distinguishes between three classes of clutter: 1) bottom-like (spatially distributed and temporally invariant), 2) compact-stationary (spatially discrete and temporally invariant), and 3) compact-nonstationary (spatially discrete and temporally varying—i.e., moving). Environmental effects such as multi-path propagation are neglected in these studies as all data are lumped into these three categories. Notably, the compact-nonstationary data that are correlated with biologic activity had the most non-Rayleigh distribution (clutter-like). Meanwhile, the latter study by Chu and Stanton develops a physics-based formulation to predict the echo statistics associated with individual and small patches of scatterers ensonified by a directional sonar beam.

4. Acoustic Scattering in an Waveguide

Over the past two and a half decades much work has been conducted taking advantage of semi-analytical and numerical techniques to form predictions of scattering by discrete, bounded objects in a waveguide. A method which couples the far-field scattering function for a bounded object with the normal mode description of the waveguide has been applied to single scatterers in depth dependent waveguides.[30–32] Hackman and Sammelmann have developed a transition matrix (T-matrix) approach coupled with a normal mode propagation method for scattering by elastic, arbitrary shapes in range independent environments.[33] This method has been used to investigate how a scattered signal from an elastic shell is modified by propagation effects through deep water waveguides.[34] Finally an approach coupling a general scattering model with a parabolic equation (PE) propagation model has been implemented for taking advantage of the computational efficiency of the PE model in two-dimensional (2D), and three-dimensional (3D) layered waveguides[35] and range-dependent waveguides.[36] It has been shown that the effects of both depth- and range-dependent characteristics of the waveguide can be significant. For example, Kusel and Ratilal have shown that predictions of scattering by an extended (large compared to the wavelength) gas-filled cylinder in a refractive environment can underestimate echo levels by over 10 decibels (dB) at 20 kilometers (km) range when using a depth-independent sound-speed profile.[36] In the same study predictions of echo levels in a range-independent environment varied by over 10 dB at 10 km from predictions using a range-dependent (sloped-bottom) environment.

While the aforementioned studies of scattering in a waveguide have generally focused on scattering by an individual or a few objects of simple shapes, literature is sparse on scattering by large aggregations of scatterers in an acoustic waveguide. The most closely related work to that presented here is the work conducted by Ratilal et al. and Andrews et al. on modeling of scattering by aggregations of fish in a waveguide.[37–40] All of these studies entail coupling of the waveguide Green's function with the free-field scattering by aggregations of small ($ka \ll 1$) scatterers using a three-dimensional PE propagation model. None of these studies, however, attempts to model the complex

morphology of fish schools or the effects of a narrow sonar beam. Rather, the fish aggregations are treated as generally ellipsoidal and the waveguide is assumed to be uniformly energized, in the vertical dimension, by the source.

Another set of studies relevant to this work is that of Abraham and Holland who have studied the effects of deterministic multipath on reverberation statistics.[25,41] In these studies the K distribution, a two-parameter analytical distribution function often used to model radar clutter[42,43], is applied to reverberation from the sea floor and shipwrecks. It is shown that the shape parameter of bottom reverberation with a K distribution varies with an increasing number of paths in a multipath environment.

C. NAVY RELEVANCE

Clutter is a significant problem for both surface and subsurface platforms that use mid-frequency sonar to aid in detection, classification, and tracking of underwater targets. While the degree to which fish contribute to sonar clutter is not known (largely due to the lack of studies that characterize the volume reverberation during sonar exercises), it is believed that a significant portion of compact, non-stationary clutter is due to biologics.[28,44] This is due to the fact that fish can be temporally variable, spatially patchy and often are resonant in the band of mid-frequency sonar systems. These factors can lead to echo envelopes that have a highly non-Rayleigh distribution where the probability of observing high amplitude echoes is higher than that given by a Rayleigh distribution[20]. In this case the probability of false alarm (i.e., the probability that the matched-filtered output exceeds a given threshold) is increased.

The existing Navy model for volume reverberation by fish for acoustic frequencies below 10 kHz, termed Fish Scattering Strength algorithm version 1.0 (FSS v1.0), that is currently in the accreditation process, calculates the scattering by a layer of fish as the incoherent sum of scattering by uniformly distributed fish with a depth dependent frequency response modeled using the Love swimbladder model.[45] The primary weakness of such a model is that it does not inherently account for the patchiness of fish schools which, as discussed, can directly contribute to echoes that have a higher probability of false alarm. Importantly, the model does include treatment of near-

boundary, multipath effects such as time spread and ray interference; however, these effects are for specialized cases when the layer is near the surface or bottom boundaries.

A model that accurately treats both the variable nature of fish schools and accounts for complicated waveguide physics should provide more accurate predictions of reverberation from fish. Such a model would aid in the training of sonar operators whose job, at times, is to discriminate between targets and clutter in a very challenging, littoral environment littered with false targets such as shipwrecks, sea mounts, marine mammals and fish. Additionally predictions of reverberation by fish could provide baseline probabilities of false alarm given the local bathymetry, sound-speed profile, fish abundance, and operating frequency.

D. SUMMARY OF RELATED WORK AND DISSERTATION OVERVIEW

Studies of echo statistics associated with horizontally looking sonar systems have largely focused on bottom or near-bottom reverberation.[25,41,46,47] These studies have addressed some factors affecting the echo statistics including sonar parameters such as the bandwidth and elevation-dependent beampattern and environmental factors such as deterministic multipath in shallow water. Meanwhile, a few studies, involving horizontal-looking sonar systems, have analyzed statistics of echoes from aggregations of objects (e.g., aggregations of fish) in the water column.[2,48] These studies have used analytic distributions (e.g., the K distribution and the Poisson-Rayleigh distribution) fit to the echo distributions to help characterize the scatterers and, in one case, reduce active sonar clutter. A significant effect, not specifically addressed in these studies, is the effect of the source and receiver beampatterns. While LePage does explicitly address the effect of an elevation-dependent beampattern in reducing multipath interference,[46] there is no mention of the statistical effects of weighting the scattering response by the source beampattern or weighting the received echo by a beam-formed receiver response. These effects have been explicitly addressed through development of an analytical formulation for the direct path case (i.e., no boundary interactions from the surface or seafloor). This formulation, termed here the Chu-Stanton theory, predicts echo magnitude distributions associated with aggregations of scatterers in the water column ensonified by a directional sonar beam.[29] This theory has been applied to measurements of a single fish by a

broadband mid-frequency downward-looking echo sounder[20] as well as mid-frequency military sonar data that is limited to echoes arriving in a direct path geometry.[49]

Taking advantage of this theoretical work on echo statistics associated with a directional sonar ensonifying scatterers in a direct-path geometry, this dissertation focuses on echo statistics associated with a horizontally-looking directional sonar in a shallow waveguide. Specifically, the goal of this research is to develop an understanding of the physical factors, both environmental and sonar system related, that affect the echo statistics associated with aggregations of scatterers in the water column of a random oceanic waveguide. A key component of this work is the development of an acoustic model that combines an empirically validated free-field model of acoustic scattering by fish with a shallow water acoustic propagation model. Characteristics of the ensonifying system accounted for by this model include: 1) broadband waveforms, 2) a directional source, and 3) a multi-element receiver. The modeling further accounts for the following characteristics of scattering by fish: 1) depth-dependent frequency response associated with a gas-filled swimbladder and 2) complex fish aggregation morphology. Finally the model accounts for the following key features of an oceanic waveguide: 1) depth-dependent mean sound-speed profile, 2) stochastic range-dependent perturbations of the sound-speed profile, and 3) range-dependent bathymetry.

In Chapter II the effects on the echo statistics of scattering in a waveguide, randomness of the water column, directionality of the beampattern, and spatial extent of the scattering volume are each examined through Monte Carlo simulations. Furthermore, the echo statistics of thin layers of scatterers ensonified by a shallow acoustic source is examined. Comparisons are made with the K distribution and predictions of echo statistics using a phasor summation method, a numerical formulation based, in part, on the Chu-Stanton theory that explicitly accounts for waveguide effects. In Chapter III numerical predictions for scattering at long ranges (1–10 km), using the phasor summation method, are compared with first-of-a-kind, long-range, broadband acoustic measurements of sparse aggregations of fish in shallow water collected in September 2011 in the Gulf of Maine. This section includes both classification of the echoes and calculations of echo statistics. Key results include the classification of echoes, with

normalized levels at least 15 dB above the background levels, from target-sized aggregations of swimbladder-bearing fish. Furthermore, the strongly non-Rayleigh distributions of echo magnitudes from these aggregations are well modeled by the computationally efficient phasor summation method. Chapter IV summarizes this work and makes recommendations for future work.

THIS PAGE INTENTIONALLY LEFT BLANK

II. MODELING ECHO STATISTICS OF AGGREGATIONS OF SCATTERERS IN THE WATER COLUMN OF A RANDOM, OCEANIC WAVEGUIDE

A. INTRODUCTION

The physical complexities of a shallow water environment directly impact acoustic measurement systems including both military and scientific sonar systems. An understanding of how this complex environment affects echo statistics associated with scatterers in the water column can aid operators in predicting sonar performance, lead to more realistic simulations for use in training sonar operators, and help researchers develop automated discriminators that could filter clutter (i.e., non-target echoes) from echoes from scatterers of interest in sonar data. In addition to military applications, the modeling of echo statistics from aggregations of scatterers in the water column has biologic survey applications such as species discrimination and abundance estimation (e.g., see review by Horne).[50] Understanding the acoustic response to the various complexities that exist in shallow water is crucial to predicting and interpreting echo statistics in these regions. The intent of this study is to illuminate the effects of various environmental and sonar system characteristics on the statistics of long range echoes from scatterers in the water column.

For mid frequency (i.e., 1–9 kilohertz - kHz) horizontal-looking sonar systems operating at long-ranges (i.e., distances much greater than the water depth), shallow water regions of the ocean resemble a waveguide trapping sound energy between the pressure release boundary at the surface and a penetrable bottom. The waveguide is characterized by many factors that can be subdivided into deterministic and stochastic factors. To first order, the deterministic factors affecting the echo statistics are: 1) average water column sound-speed profile and 2) bathymetry. Stochastic factors can include 1) sound-speed perturbations due to internal waves, 2) bottom roughness, 3) surface roughness, 4) noise, and 5) reverberation.

In addition to the waveguide itself, characteristics of the acoustic system (i.e., the source and receiver) can affect the echo statistics. For example, in the case of scatterers

randomly located in a directional acoustic beam, the beampattern value applied to each scatterer becomes a statistical quantity that can be considered a stochastic component.[29]

A scatterer can have several characteristics, both deterministic and stochastic, that affect the echo statistics. Characteristics such as shape and location may be well known (e.g., a rock outcropping) or may be highly variable or even random in time and space (e.g., a mobile school of fish with a time varying morphology).[19] Depending on the ratio of the acoustic wavelength to the scatterer size and the scatterer shape, the scattering object may have a directional beampattern (e.g., large fish or marine mammals at high frequencies) or an isotropic point-scatterer-like beampattern (e.g., swimbladder-bearing fish at frequencies near resonance). Finally, the scattering response may have a stochastic component leading to a statistical distribution of the magnitude and phase of the response. This factor, termed the scatterer probability density function (PDF), is a function of the sonar volume resolution cell and the number of individual scattering objects within that cell. For example, an object with fixed orientation may have a delta function PDF; whereas, many closely spaced scatterers of similar scattering amplitude would tend towards a Rayleigh PDF.

Understanding and predicting statistics of echoes from underwater scatterers has been the source of much research over the past several decades. Several physics-based models have been developed to simulate reverberation from both the scatterers in the water column and near boundaries as well as the surface and bottom themselves. Models of direct-path (i.e., no boundary effects) reverberation by scatterers in the water column have included complexities such as a physics-based spatial distribution of fish near the surface[48] and a fully directional sonar beam;[29] while, models of bottom reverberation in a shallow-water waveguide have accounted for deterministic multipath,[25] and a vertically directional beam with deterministic multipath.[46] However, none of these acoustic reverberation models attempts to simulate a 2D directional beampattern in a realistic, shallow-water, oceanic environment. In order to accurately model such an environment both deterministic and stochastic environmental effects should be addressed.

Predictions of echo statistics, from aggregations of scatterers modeled as point sources that are located in the water column of an oceanic waveguide and are ensonified

by a long-range (i.e., horizontally steered) sonar, are presented for various levels of environmental and system complexity. The goal is to understand the contributions to the echo statistics of several key characteristics of the sonar-waveguide-scatterer system: 1) directional source with a narrow beam, 2) depth-dependent sound-speed profile, 3) random depth- and range- dependent sound-speed perturbations, 4) scatterers with Rayleigh-distributed scattering responses before beampattern and waveguide effects. It is believed that this combination of characteristics reasonably represents many of the first-order effects that may be observed in echo statistics from scatterers in the water column ensonified by a directional sonar system. Although some complexities are not accounted for (e.g., large scale bathymetry, bottom and sea surface roughness, etc.), these results should provide a basis from which to extrapolate an understanding of echo statistics by water column scatterers in a real ocean waveguide. For example, the incorporation of diffuse internal waves (IWs) is just one of many sources of random fluctuations in the waveguide that could have been chosen. Since diffuse IWs are present anywhere in the world that a stratified ocean layer exists, this seems like a reasonable characteristic to induce a range-dependent, random component in the waveguide. It is expected that other stochastic waveguide characteristics such as a rough surface would have statistical similarities in that it would increase the phase and amplitude variation of the pressure field. Echo magnitude PDFs generated by the physics-based approach used in this study are compared, in some key cases, with the K distribution, an empirically validated method commonly used in describing echo statistics in long-range sonar applications.

This chapter is organized as follows. Section B, Probability Density Functions associated with Acoustic Backscatter, describes the theory and application of four analytic echo magnitude PDFs used in this study. Section C, Numerical Methods, describes the two-way parabolic equation model and its various components, including the internal wave model, as well as the phasor summation method both of which are used to generate echo statistics in this study. Sections D-F describe the echo statistics of scatterers randomly located in depth in a simple, deterministic waveguide (Sec. D), of scatterers randomly located in depth in a stochastic waveguide randomized by diffuse

broadband internal waves (Sec. E), and of thin layers of scatterers in a random waveguide (Sec. F). Section G is the discussion with concluding remarks.

B. PROBABILITY DENSITY FUNCTIONS ASSOCIATED WITH ACOUSTIC BACKSCATTER

Many acoustic reverberation studies have focused on identifying candidate PDFs to characterize echoes from objects in the water column. An echo PDF can be sensitive to characteristics of the scatterer, the environment, the ensonifying system, and even processing techniques used to extract echoes from the data. In this study comparisons are made with four distributions that have varied application under a wide-range of conditions.

1. Rayleigh Distribution

In signal theory a zero-mean complex Gaussian distribution arises when a received signal, measured at a random delay time or receiver location, is composed of the sum of many independent signals with random amplitude and phase given a few, somewhat flexible, assumptions.[51] This resultant field is considered *saturated*. The magnitude of the received signal is Rayleigh distributed which is described by a PDF with a single parameter, h, as

$$\mathrm{p}\{\hat{x}\} = \frac{\hat{x}}{h^2} e^{-\hat{x}^2/2h^2} \quad , \tag{2.1}$$

where $\mathrm{p}\{\cdot\}$ indicates the probability density of the random variable enclosed in braces and denoted by a hat. An example of this distribution occurs when many randomly located scatterers, with identically distributed scattering amplitudes, are ensonified by an acoustic system in a direct path environment the echo envelope (i.e., the magnitude of the complex pressure at the receiver) becomes Rayleigh distributed as the number of scatterers gets large. This effect, observed as early as 1960 in volume reverberation from a high frequency acoustic system,[52] has become the benchmark for determining the likelihood of a scatterer causing a false-alarm for a military sonar system.[28,53] Thus, echo envelopes that have a PDF with an elevated, high amplitude tail when compared with a Rayleigh distribution are considered clutter and have a higher probability of causing a false alarm. All echo envelope distributions modeled in this study are, therefore,

compared with a Rayleigh distribution to gain physical insight and to measure the contribution of specific parameters towards this characteristic of clutter.

2. Exponential Distribution

It is well known that the intensity PDF of a fully saturated field (i.e., uniform, random phase on the interval 0 to 2π) is the chi-square distribution with two-degrees of freedom (a.k.a., the exponential distribution).[54] However, an exponential distribution can also arise in the echo envelope PDF of a monostatic system ensonifying a single scatterer in the saturated field of a waveguide as will be shown in this study. Consider the case of an omni-directional source ensonifying an isotropic (monopole) scatterer. In this case the acoustic modes from the forward problem are relevant to the back propagation (i.e., reciprocity applies) and the pressure at the receiver is expected to be proportional to the square of the pressure at the scatterer

$$P_{\mathrm{r}} \propto P_{\mathrm{s}}^2. \tag{2.2}$$

Given a known statistical nature of the pressure field at the scatterer location, this relationship makes it is possible to deduce the statistics at the receiver for some simple cases. For a random location in depth or delay time the pressure field at some scatterer can be represented as a complex random variable

$$P_{\mathrm{s}} = \hat{X} + \mathrm{i}\hat{Y} \tag{2.3}$$

with an envelope of $\hat{\epsilon}_{\mathrm{s}} = \sqrt{\hat{X}^2 + \hat{Y}^2}$. For the case of N interfering scatterers Eq. (2.3) can be substituted into Eq. (2.2) and summed over all contributing scatterers to give the pressure at a receiver of a monostatic system

$$\hat{P}_r = \sum_{n=1}^{N} \left(\hat{X}_n + \mathrm{i}\hat{Y}_n \right)^2. \tag{2.4}$$

The envelope at the receiver is then given as

$$\hat{\epsilon}_r = \left[\left(\sum_{n=1}^{N} \hat{X}_n^2 - \hat{Y}_n^2 \right)^2 + \left(\sum_{n=1}^{N} 2\hat{X}_n \hat{Y}_n \right)^2 \right]^{(1/2)} \tag{2.5}$$

which conveniently reduces, for the case of $N = 1$, to

$$\hat{\epsilon}_r = \hat{X}^2 + \hat{Y}^2 = \hat{\epsilon}_{\mathrm{s}}^2. \tag{2.6}$$

An important application of this result is in the case of a single scatterer located in a waveguide. At some range, r_{sat}, it is assumed that the pressure field becomes saturated by interference of the forward-scattered acoustic wave. At this range, sampling the pressure field $\hat{P}_s(r_{\text{sat}})$ at various depths or delay times results in a complex Gaussian random variable with an envelope, $\hat{\epsilon}_s$, that is Rayleigh distributed. According to Eq. (2.6), then, the envelope at the receiver, $\hat{\epsilon}_r$, is a Rayleigh random variable squared, that is, a random variable drawn from the exponential distribution:

$$\mathrm{p}\{\hat{\epsilon}_r\} = \frac{1}{\langle \hat{\epsilon}_r \rangle} e^{-1/\langle \hat{\epsilon}_r \rangle}. \tag{2.7}$$

3. K Distribution

One distribution that has been widely used in both radar and sonar theory for describing echo envelopes is the K distribution. This distribution has been used to model the high amplitude "tail" of PDFs of echoes envelopes from seafloor reverberation as well as shipwrecks.[25,41] The K distribution is a two-parameter distribution

$$\mathrm{p}\{\hat{x}\} = \frac{4}{\sqrt{\lambda_k}\Gamma(\alpha_k)} \left(\frac{\hat{x}}{\sqrt{\lambda_k}} \right)^{\alpha_k} K_{\alpha_k - 1}\left(\frac{2\hat{x}}{\sqrt{\lambda_k}} \right), \tag{2.8}$$

where $K_\nu(z)$ is a modified Bessel function of the second kind, $\Gamma(y)$ is a Gamma function, α_k is a shape parameter, and λ_k is a scale parameter. As the shape parameter increases the K distribution tends towards a Rayleigh distribution, so that this parameter is used as a proxy for the likelihood of a false alarm (i.e., a K distribution with a low shape parameter represents a higher probability of false alarm).

4. Chu-Stanton Theory

Combining the work of Ehrenberg et al.[55,56] and Barakat,[57] Chu and Stanton provide an analytical model for the echo statistics of a finite number of scatterers each with an arbitrary probability density function (PDF) and each randomly located within a directional sonar beam.[29] The model provides an efficient, physics-based method of calculating the echo PDF in a direct path environment when it is important to include beampattern effects. In these cases, such as a narrow beampattern or few scatterers, the

echo envelope PDF tends to be strongly non-Rayleigh even when the scatterer itself has a Rayleigh distributed scattering response.

The PDF of the magnitude of the complex echo from *N* scatterers in a directional beam is given as

$$\mathrm{p}_e\left\{\hat{\epsilon}\right\} = 2\hat{\epsilon}\sum_{m=1}^{\infty}\frac{\phi_{R,I}^{\Sigma}\left(\frac{\eta_m}{\epsilon_{\max}}\right)}{\left[\epsilon_{\max}J_1(\eta_m)\right]^2}J_0\left(\eta_m\frac{\hat{\epsilon}}{\epsilon_{\max}}\right) \tag{2.9}$$

where, ϵ and $\epsilon_{\max}$ are the magnitude (or envelope) of the echo and maximum value of ϵ, respectively. J_ν is the Bessel function of the first kind of order ν, and η_m are the positive roots of $J_0(x)=0$. The summation is over $m=1,2,...$ roots of the Bessel function. The variable $\phi_{R,I}^{\Sigma}$ is the characteristic function (CF) of the real or imaginary component of the complex echo arising from the sum of echoes from *N* scatterers that is,

$$\phi_{R,I}^{\Sigma}(\omega) = \prod_{n=1}^{N}\phi_{R,I}(\omega;\beta_n) \tag{2.10}$$

where, β_n is a parameter vector for the nth characteristic function.

The distribution of scattering amplitudes due to the scattering response and the beampattern effect is captured in the characteristic function of each scatterer which is expressed as

$$\phi_{R,I}(\omega,\beta_n) = \int_0^{\infty}\left(\int_{\hat{\epsilon}}^{\infty}\frac{1}{\tilde{x}}\mathrm{p}_{A_n}\{\tilde{x}\}\mathrm{p}_B\left\{\frac{\hat{\epsilon}}{\tilde{x}}\right\}d\tilde{x}\right)J_0(\omega\hat{\epsilon})d\hat{\epsilon}, 0\le b\le 1 \tag{2.11}$$

where, $\tilde{x} = ka\sin\alpha$. For a piston transducer with an axisymmetric beampattern, as modeled in this study, *ka* is the product of the acoustic wavenumber and the piston radius, respectively, and α is the polar angle of a scatterer within the beam. The function p_{A_n} is the PDF of the modulus of the scattering amplitude of the nth scatterer without beampattern effects and p_B is the PDF of the beampattern when the location of the scatterer in the beam is taken as a random variable. An approximate solution for p_B is

given by Eq. 9 of ref. 29 for the case of a circular piston transducer where α is limited to the angle where the beampattern value first falls to the value of the maximum value of the first side lobe.

C. NUMERICAL METHODS

1. Two-way Parabolic Equation Model

a. Overview

Modeling echoes from scatterers in the ocean requires accounting for both variability due to waveguide effects and scattering effects. The approach taken here is to connect a range-dependent, shallow water propagation model with a free-field, point-scatterer model. In selecting a propagation model for use in generating echo statistics it is necessary to use an algorithm that accurately and efficiently predicts transmission loss through a complex waveguide at the frequency, or frequency band, of interest (e.g., 3 kHz in this study). Ray-based solutions can be highly efficient, but as a high-frequency approximation, these algorithms become less accurate with decreasing frequency; while, normal mode solutions are highly accurate, but can be very inefficient at mid to high frequencies as the number of modes required increases with frequency. Parabolic equation (PE) models, in contrast, provide a good blend of accuracy and efficiency in shallow water environments. PE models generally implement a range-marching method to solve the parabolic equation which is particularly well suited to range-dependent problems (see Appendix A for derivation of parabolic equation method used in this study). The scattering model used in this study, a point scatterer or collection of point scatterers represented by one or more omnidirectional sources, is chosen to represent scatterers in the water column that are small compared to the wavelength of a mid-frequency system (e.g., small- to medium-sized fish, bubbles, zooplankton). In this regime these scatterers act as monopoles.

The numerical model, as implemented in this study, is a single frequency, monostatic, three-dimensional (3D) acoustic model using an N×2D framework (i.e., a 3D environment modeled using N two-dimensional (2D) vertical slices at varying azimuthal angles from a source). The major limitation of the N×2D method is that out of plane

propagation or scattering is not considered and this effect is not treated in this study. It should be noted that the methods presented here can be extended to broadband, bistatic cases with only minor modifications. The model incorporates three major and somewhat independent components: 1) a PE algorithm for propagation, 2) a directional source field and 3) a free-field scattering model. The environmental parameters are all considered stationary for the two-way travel duration of the acoustic signal and thus, are simply reversed for the back propagation as described in the following work-flow description.

b. Propagation Algorithm and Workflow

The propagation component of the model is a MATLAB-based derivative of the Range-dependent Acoustic Model (RAM)[58] developed by Fabre called MRAMGEO.[59] Using a Padé approximation MRAMGEO solves the parabolic equation for a range-dependent environment using a finite element method (see Appendix B for comparison between RAM and MRAMGEO).

A MATLAB shell manages the overall flow of the model which runs as follows:

1. Generate the MRAMGEO input script to include parameters based on source, environmental, and scatterer characteristics as well as algorithm specific parameters.

2. Calculate a directional PE starter field based on source parameters.

3. Calculate the complex field for the forward propagation and extract the complex pressure at the scatterer location.

4. Calculate omnidirectional PE starter fields at the range of each scatterer based on the forward propagation output at the depth of the scatterer and the scatterer frequency response.

5. Reverse the environmental parameters (i.e., bathymetry, sound-speed profile, bottom parameters) and calculate the scattered field from each scatterer back to the receiver.

6. Sum the complex field at the receiver across all scatterers.

c. Parabolic Equation Starter Fields (Source and Scatterer Models)

Two types of starter fields are used as initial conditions for the propagation algorithm. At the acoustic source a directional beampattern is modeled by the starter field; whereas, at each scatterer an omnidirectional beampattern is generated to model a point scatterer.

The starter field at the acoustic source, $\Psi(\mathrm{f};z)$, is generated using the Fourier transform relationship between the wavenumber and the spatial domain

$$\Psi(\mathrm{f};\theta,z) \xleftrightarrow{\text{FT}} b(\mathrm{f};\theta,k_z). \tag{2.12}$$

The beampattern, *b*, is expressed as a function of frequency, f, the azimuthal angle, θ, and the vertical component of the wavenumber vector, k_z, where $k_z = |\mathbf{k}_0|\sin(\phi)$, a function of $\mathbf{k}_0$, the wavenumber vector at the source, and the elevation angle, ϕ.

As an example, a circular piston with a 5 degree 3 decibel (dB) beamwidth (i.e., the width where the beampattern level first falls 3 dB below the on-axis peak) was simulated in deep water (no boundary effects) using 8 Padé terms in the PE model. A comparison is made between the predictions normalized to the minimum transmission loss and the analytical formula for the composite, two-way beampattern of a circular piston

$$b(\alpha) = \left[\frac{2J_1 ka(\sin\alpha)}{ka(\sin\alpha)}\right]^2, \tag{2.13}$$

where α is the polar angle, J_1 is the first-order Bessel function of the first kind and ka is the product of the wavenumber and the piston radius.

The resulting calculation is in excellent agreement in the main lobe with an error of less than 0.3 dB and an error of less than 1 dB out to ± 5 degrees angle of propagation outside of the deep nulls (Figure 2.1). A significant increase in error at increasing angles (~5 dB at 20 degrees) does occur; however, these errors should not be significant for shallow water modeling where energy at high angles is significantly attenuated by boundary interactions.

The starter field at the scatterer is generated by taking the complex output of the PE algorithm, $\Psi(\mathrm{f}; r_s, z_s)$, at the scatterer range, r_s, and depth, z_s, and applying an effective backscattering amplitude, $\hat{f}_{\mathrm{bs}}^{\mathrm{eff}}$, and a weighting function, w

$$\Psi(\mathrm{f}, r_0, z) = \Psi(\mathrm{f}; r_s, z_s)\, \hat{f}_{\mathrm{bs}}^{\mathrm{eff}}(\mathrm{f}; z_s) w(\mathrm{f}; z) \tag{2.14}$$

where $w(z)$ is the Greene's source function, a weighted Gaussian function used as an initial field for a PE calculation with good wide angle properties[60]

$$w(z) = \sqrt{k_0}[1.4467 - 0.4201 k_0^2 (z - z_s)] \exp\left(\frac{-k_0^2 (z - z_s)^2}{3.0512} \right). \tag{2.15}$$

The effective backscattering amplitude, $\hat{f}_{\mathrm{bs}}^{\mathrm{eff}}$, is a random variable, drawn from either a delta function (i.e., $\hat{f}_{\mathrm{bs}}^{\mathrm{eff}} = 1$), in the case of a constant frequency response, or a complex Gaussian distribution, in the case of a Rayleigh scatterer.

2. Internal Wave Model

a. Sound-speed Perturbations due to Diffuse Internal Waves

One way to model sound-speed variability in an oceanic waveguide is to incorporate a diffuse, broadband internal wave model such as the Garrett-Munk model[61,62] parameterized to fit shallow water observations.[63] The mean squared sound-speed variability is described as

$$\left\langle \mu(z)^2 \right\rangle = \frac{\zeta_0^2}{c_0^2} \frac{N_0}{N_B(z)} \left(\frac{dc_{pot}(z)}{dz} \right)^2 \tag{2.16}$$

where, the brackets represent the mean with respect to range or time delay, the fractional change in sound speed, $\mu = \delta c / c_0$, ζ_0 is a reference displacement in meters (m), c_0 is a reference sound speed in meters per second (s), and N_0 is a reference buoyancy frequency of 5.24×10^{-3} radians (rad) per s (3 cycles per hour - cph). Finally, c_{pot} is the sound speed in m/s based on the potential temperature at a given depth , z.

The Brunt-Vaisala frequency, N_B, can be calculated from observations and is generally expressed in rad/s as

$$N_B^2(z) = -\frac{g}{\rho_{\text{sw}}(z)} \frac{\partial \sigma_T(z)}{\partial z} \tag{2.17}$$

where, g is gravity in m/s^2 , ρ_{sw} is the seawater density in kg/m^3, and σ_T is the density anomaly with the pressure reduced to atmospheric pressure in kg/m^3.

b. Implementation of Sound-Speed Perturbations in Propagation Model

A representative sound-speed profile (SSP) for a stratified water column, obtained during an experiment in the Gulf of Maine in September of 2010, was fitted with an analytic SSP following the canonical form of the Munk sound-speed profile[64]

$$c(z) = c_{\text{min}} \left[1 + \xi \left(\eta + e^{-\eta} - 1 \right) \right] \tag{2.18}$$

where, $\eta = 2(z - z_{\text{axis}}) / h_0$ and $c_{\text{min}} = 1472$ m/s is the minimum sound speed located at $z_{\text{axis}} = 68$ m. Empirical parameter values used to fit with the observed profile are $\xi = 2.88 \times 10^{-3}$, which is dimensionless, and $h_0 = 48$ m. The resulting profile (Figure 2.2, left panel) is used as the unperturbed SSP for all simulations incorporating depth-dependent sound-speed profiles described in this study.

Internal wave induced perturbations to the analytic SSP were generated via the Colosi and Brown method[65] using empirical values for buoyancy frequency, $N_B(z)$, and potential sound speed, $c_{\text{pot}}(z)$, derived directly from the observed profile (Figure 2.3) and heuristic parameters describing the internal waves given in Table 2.1. The internal wave parameters, j_{max}, the number of internal wave modes, j^*, the mode parameter, and ζ_0, the internal wave displacement, were selected to reasonably represent a shallow water internal wave field with a range-averaged, root-mean-squared sound-speed perturbation, δc_{rms}, of approximately 2–5 m/s in the main thermocline (Figure 2.3). Finally, the sound-speed perturbations, $\delta c(r)$, as a function of range, r, were added to the analytic sound-speed profile in Eq. (2.18) and incorporated every 10 m in the propagation algorithm (Figure 2.4). The range step for new sound-speed profiles was

selected to reasonably represent the minimum horizontal wavelength for the band of the shallow water internal wave spectrum where most of the energy resides (50 m to 300 kilometers - km).[66]

3. Phasor Summation Method for Generating Echo PDFs

The distribution of complex echo amplitudes, described analytically by the characteristic function in Eq. (2.10), can be determined numerically using a Monte Carlo simulation in which the beampattern values, scattering amplitude and phase are treated as random variables. Each realization of the simulation entails summing *N* random phasors representing the coherent sum of the scattered field from *N* scatterers as measured at a receiver:

$$\hat{s} = \sum_{n=1}^{N} \frac{\hat{\xi}_n}{2|\hat{\mathbf{r}}_n|} \hat{b}_n^{\mathrm{S}}(\theta_{\mathrm{S}}, \phi_{\mathrm{S}}) \hat{b}_n^{\mathrm{R}}(\theta_{\mathrm{R}}, \phi_{\mathrm{R}}) e^{2ik|\hat{\mathbf{r}}_n|} \tag{2.19}$$

where, $\hat{b}_n^{\mathrm{S}}$ and $\hat{b}_n^{\mathrm{R}}$ represent the source and receiver beampattern weighting, respectively, as a function of the location within an arbitrary beam. In this case θ is the azimuthal angle and ϕ is the angle of elevation from the source, subscript "S," and to the receiver, subscript "R." In a direct path case (i.e., no waveguide effects) the term $\hat{\xi}_n$ represents the complex amplitude of the nth scatterer randomly located at position $\hat{\mathbf{r}}_n$. This random variable is drawn from the distribution of scatterer amplitudes underlying the envelope PDF, p_A. For example, if p_A is a Rayleigh PDF, then $\hat{\xi}_n$ is drawn from a zero-mean complex Gaussian distribution. In the case of a waveguide, it is shown in this study that $\hat{\xi}_n$ can be used to represent the combination of the scattering response and waveguide effects. Upon completing the Monte Carlo simulation the echo magnitude PDF, $\mathrm{p}_\epsilon\{\hat{\epsilon}\}$, is then determined from the normalized histogram of the echo envelopes, $\hat{\epsilon} = |\hat{s}|$.

In order to position the scatterers randomly in the beam, while ensuring a uniform distribution of phase of the scattered signal, the locations of the scatterers must be uniformly distributed on a spherical shell. Importantly, at the long ranges examined in this study, the intersection of a spherical shell centered on the source and a vertical

transect of waveguide, closely approximates a vertical column. So this method simulates scatterers randomly located in depth over some small extent of ranges. The width of the shell, in the direct path cases, is determined by the wavelength of the signal. A width of one half of a wavelength ensures uniform distribution of phases over the interval 2π for a two way path of the signal while keeping geometric spreading losses to a minimum. Arndt conveniently provides an analytical method for generating a uniform distribution of points on a spherical shell[67]

$$\left|\hat{\mathbf{r}}\right| = \left[\left(r_1^3 - r_0^3\right)\hat{n}_1 + r_0^3\right]^{(1/3)} \tag{2.20}$$

where $\hat{\mathbf{r}}$ is the random position of the points and r_0 and r_1 are the inner and outer shell radii, such that $r_1 - r_0 \geq \lambda / 2$.

$$\phi_{el} = \frac{\pi}{2} - \cos^{-1}(1 - 2\hat{n}_2) \tag{2.21}$$

$$\theta_{az} = 2\pi\hat{n}_3 \tag{2.22}$$

The terms, $\hat{n}_i$, are random variables drawn from a uniform distribution on the interval [0,1]. For cases where the spherical shell is truncated either in azimuth, θ, or in elevation, ϕ, the intervals for $\hat{n}_2$ and $\hat{n}_3$ are limited such that ϕ_{el} and θ_{az} are limited to the appropriate angles.

4. Validation of Models using Direct Path Geometry

The Chu-Stanton theory (Eq. (2.9)), was used to validate both the two-way PE model and the numerical phasor summation (PS) solution (Eq. (2.19)). A direct path (i.e., no boundary effects) scenario was used for validation with *N* scatterers located within the main lobe of a directional beam where *N* = 1, 2, 3, 10. Given the propagation angle limitation of the PE model (i.e., the model cannot accurately predict acoustic propagation at very wide angles), limiting the beam to the main lobe provides a way to benchmark the model. In this case the main lobe is defined by the angle at which the main lobe decreases to the value of the highest side lobe (θ_{SL}). Since the Chu-Stanton theory applies to a sonar ensonifying scatterers in a direct path geometry, the parameters for the two-way PE model were selected to ensure boundary reflected echoes did not interfere with the direct path signal (Table 2.2).

Results of these calculations showed excellent agreement between all three models (Figure 2.5). Due to the computationally intensive nature of the PE calculations, many fewer Monte Carlo instances, N_{MC}, were used ($N_{MC,PE}$ = 1200) than in the phasor summation solution ($N_{MC,PS} = 5\times10^5$) resulting in a greater error between the PE calculation and the analytic solution, Eq. (2.9). However, the results of the PE simulation still accurately predict the increased probability in the high amplitude portion of the PDF over a Rayleigh distribution (i.e., the "heavy tail" of the PDF) in all cases (see Appendix C for more benchmarks of two-way PE model).

D. SIMULATIONS OF ECHOES FROM A SINGLE SCATTERER IN A DETERMINISTIC WAVEGUIDE

In order to illuminate the effects of various aspects of the sonar-waveguide-scatterer system on the echo statistics, three sets of simulations are presented using a combination of analytic and numerical models described in Sec.II.B-C This first set of simulations analyzes the effects of three influences on sonar echo statistics: a depth dependent sound-speed profile, a directional sonar system, and a variable scattering response. The first case, a single scatterer with a constant, or delta function, scattering response (termed here a *delta function scatterer*) ensonified by a point source in a Pekeris waveguide, provides a baseline for comparison with models of greater complexity. It is seen that this case results in strong deterministic multipath caused by the reflection of acoustic energy from the sea surface and bottom at all ranges. Each subsequent case is then compared with this result to understand how varying environmental conditions and sonar specifications cause the echo statistics to deviate from this simple case.

1. Delta Function Scatterer Ensonified by an Omnidirectional Source in a Constant Sound-Speed Environment (Case A, Table 2.3)

The first case investigated is that of a 3 kHz omnidirectional source ensonifying a single scatterer, with a constant scattering response, in a Pekeris waveguide (see Table 2.3 for key model parameters). In this case the source is located at 50 m in 100 m of water depth. The resulting intensity field is characterized by a highly structured pattern caused by interference between numerous reflections of acoustic energy from both the sea surface and bottom boundaries (Figure 2.6a). At relatively short ranges the pressure

field, when randomly sampled in depth, is shown to be Rayleigh distributed. PE simulations predict the magnitude of the pressure field will approach a Rayleigh distribution by 500 m (results not shown) and will reach a Rayleigh distribution by 1 km (Figure 2.7). A Lilliefors test comparing the real and imaginary components of the pressure distribution at 1 km, individually, with a normal distribution produce the following *p*-values: $p_{real/}p_{imag.} = 2.23\times10^{-1} / 8.90\times10^{-2}$ (see Appendix D for details of statistical methods used in this study).

Simulations of echo statistics at the receiver predict a PDF that is nearly exponentially distributed at 500 m (results not shown) and exponentially distributed at 1 km ($p = 0.35$) as shown in Figure 2.7. The exponential distribution arises from the squaring effect of the pressure field induced by the two-way propagation through the waveguide (Eq. [2.2]).

2. Effects of a Depth-Dependent Sound-Speed Profile (Case C, Table 2.3)

A significant amount of environmental realism can be added to the model by incorporating a realistic sound-speed profile that mimics the average depth-dependence in the ocean (fixed in range). An observed shallow water profile, taken during a research cruise in the Gulf of Maine in September of 2010, is used as a template for a stratified, shallow water profile. A Munk sound-speed profile, Eq. (2.18), is fitted to this observation giving an analytic approximation to a realistic shallow water profile (Figure 2.2).

The result of adding this depth-dependent sound-speed profile is to refract some of the energy into a sound channel that is weakly detectable in a transmission loss plot (Figure 2.6b). In this case, the pressure field, when randomly sampled in depth, reaches a saturated state by 3.5 km ($p_{real/}p_{imag.} = 0.83 / 0.36$) compared with 1 km in the constant sound-speed case (Figure 2.8). The PDF of the echoes at the receiver do not pass a statistical test for an exponential distribution at either range modeled; however, it is clear that the distribution is approaching an exponential (Figure 2.8) as can be seen by the small Kullback-Leibler distances, d_{KL}, ($d_{\mathrm{KL}} = 2.19\times10^{-2}$ at 1 km; $d_{\mathrm{KL}} = 2.95\times10^{-2}$ at 3.5 km) compared with that at 500 m ($d_{\mathrm{KL}} = 4.75\times10^{-2}$ – figure not shown).

3. Effects of a Vertically Directional Beampattern (Case D, Table 2.3)

A key parameter affecting echo statistics is the sonar beampattern.[20] In order to investigate the effects of a directional source, a circular piston transducer with a wavenumber-radius product, *ka*, of 37.06 is modeled. This size source produces an axisymmetric beampattern with a narrow 5 degree 3 dB beamwidth. In order to identify effects corresponding only to the directionality of the beam in the vertical plane, the scatterer in this simulation was randomly located in depth, but azimuthally on-axis. Thus, these simulations are akin to a vertical line array with a beampattern that is elevation-depression dependent, but constant in azimuth.

The most noticeable effect of the addition of the directional source is to produce a distinct shadow zone in the forward pressure field as can be seen in the transmission loss plot (Figure 2.6c). Simulations were conducted with a single scatterer randomly located in depth within two separate regions: 1) the shadow zone (0 to 40 m depth) and 2) the energetic zone (40–100 m depth). At the ranges investigated, only a weak range-dependence exists in the echo statistics distributions (Figure 2.9). For the shadow zone, the statistics are strongly non-Rayleigh and non-exponential as seen in the tail of the distribution. It should be noted, however, that the mean of the echo amplitudes is very low in the shadow zone and few conclusions can be drawn from these PDFs. In the energetic zone, the pressure field does not reach a Rayleigh distribution at any of the ranges simulated up to 9.5 km ($4.61\times10^{-2} \le d_{\mathrm{KL}} \le 1.48\times10^{-1}$ – figure not shown). At the receiver, the echo PDFs are initially (at a range of 500 m) strongly non-exponential ($d_{\mathrm{KL}} = 7.17\times10^{-2}$), but become more exponential-like at ranges from 3.5 to 9.5 km ($2.65\times10^{-2} \le d_{\mathrm{KL}} \le 5.73\times10^{-2}$). In all cases the distribution failed a Lilliefors test for goodness of fit with an exponential distribution. These results suggests that, at least at these short ranges where much of the sound energy is coherently refracted into the sound channel, the limited deterministic boundary interactions may not be sufficient to induce an exponential distribution as seen in Case A with the omnidirectional source.

4. Scatterer of Varying Spatial Extent with a Variable Scattering Response (Rayleigh Scatterer) (Case B, Table 2.3)A spatially compact aggregation of a large number of scatterers all with similar scattering amplitudes (e.g., a small school of uniformly sized fish) induces a free-field scattering response that, when taking the modulus, is Rayleigh distributed[68] and is termed here a *Rayleigh scatterer*. For direct path calculations, such a scatterer can be efficiently modeled by a single point scatterer with a Rayleigh distributed response (e.g., see Chu and Stanton, 2010).[20] However, in a waveguide the scattering response is strongly sensitive to the spatial extent of the scatterer leading, in some cases, to a distribution of echo envelopes that is strongly non-Rayleigh before considering beampattern effects. An explanation of this sensitivity can be shown using a simple transfer function model for the echo distribution.

Let the frequency response of the one-way path in the waveguide be defined in phasor notation as

$$\hat{H}(\mathrm{f},\hat{\mathbf{r}}) = \hat{H}_0(\mathrm{f},\hat{\mathbf{r}})e^{\mathrm{i}k\hat{s}} \tag{2.23}$$

where, $\hat{H}_0$ is the slowly varying magnitude of the waveguide response which is dependent upon frequency, f, and a random location in the waveguide, $\hat{\mathbf{r}}$. The phase, then, is dependent on the one-way path length from the source to this random location, $\hat{s}$. In keeping with the methodology used throughout this analysis, the waveguide response is considered a random variable as sampled randomly in depth at a fixed range. The echo magnitude, also a random variable, is then given as

$$\hat{\epsilon} = \left| \sum_{n=1}^{N_s} S(\mathrm{f})\hat{H}_0^2(\mathrm{f},\hat{\mathbf{r}}_n)e^{2\mathrm{i}k\hat{s}_n} \right| \tag{2.24}$$

where, $S(\mathrm{f})$ is the source amplitude and N_s is the number of point scatterers that contribute to a single Rayleigh scatterer. These point scatterers, each with the same fixed scattering response, are located randomly within some scattering volume at position $\hat{\mathbf{r}}_\mathbf{n}$ with path length $\hat{s}_n$. The waveguide response has been squared for the two-way scattering case based on reciprocity of the acoustic paths for an omnidirectional source and a point scatterer as shown in Sec II.B.2.

When the radius of the scattering volume, r_V, is small compared with some correlation length of the waveguide intensity field, the slowly varying magnitude of the waveguide response, $\hat{H}_0$, can be assumed to be independent of the individual point scatterers paths and, thus, pulled out of the summation. The echo magnitude then becomes

$$\hat{\epsilon} \simeq S(\mathrm{f})\hat{H}_0^2 \left| \sum_{n=1}^{N_s} e^{2ik\hat{s}_n} \right|. \tag{2.25}$$

If the product of the wavenumber and the two-way path length, $2k\hat{s}_n$, is uniformly distributed on the interval 2π, then the magnitude of the summation becomes a Rayleigh random variable by the central limit theorem (CLT). Thus, in the case of a saturated pressure field, where we have shown that the echo envelope for any single scatterer with constant scattering response, $\hat{H}_0^2$, is exponentially distributed, the echo envelope, $\hat{\epsilon}$, for a Rayleigh scatterer is the product of an exponential random variable and a Rayleigh random variable.

However, when the radius of the scattering volume is large compared with the minimum distance over which the intensity field becomes uncorrelated, $\hat{H}(\mathrm{f}, r_n)$ cannot be considered independent of the location of each point scatterer. So, for a saturated pressure field as r_V becomes large enough, the summation in Eq. (2.24) is over N_s independent and identically distributed (i.i.d.) random variables, $\hat{H}^2$. By the CLT, then, $\hat{\epsilon}$ becomes a Rayleigh random variable.

This result is validated through simulations of spherical Rayleigh scatterers of varying radii located in a saturated acoustic pressure field. Each Rayleigh scatterers is modeled using 10 point scatterers uniformly distributed within a sphere of a given radius. A Monte Carlo simulation with an omni-directional source and 10 scatterers in a direct path geometry shows that 10 scatterers is sufficient to generate a Rayleigh PDF ($p_{real}/p_{imag.}$ = 0.86 / 0.88 – figure not shown). To simulate Rayleigh scatterers of varying size, the radius of a sphere incorporating the 10 point scatterers, r_V, is varied from 0.125

m (a two-way travel distance across the scatterer of ~1 wavelength) to 4.0 m (two-way travel of ~32 wavelengths).

Monte Carlo simulations were conducted comparing a Rayleigh point target (i.e., an infinitesimally small scatterer located at a single point with a magnitude drawn from a Rayleigh distribution for each random instance) with a Rayleigh target of varying size (Figure 2.10). In the case of a very small radius, r_V = 0.125 m, the echo magnitude distribution is exponential-like with a slightly heavier tail very similar to the result of the Rayleigh point target. According to the theory, the distribution in this case approaches the product of an exponential and a Rayleigh random variable. As the radius increases the distribution begins to approach a Rayleigh distribution as predicted ($d_{\mathrm{KL}} = 7.14\times10^{-2}$ for $r = 2.0$ m and 1.35×10^{-2} for $r = 4.0$ m).

This result has important implications for modeling compact aggregations of scatterers in the water column. Principally, it becomes important to model an extended, finite-length Rayleigh scatterer with a representative spatial extent rather than by a single point scatterer with a non-uniform scattering response (e.g., the Rayleigh, point target associated with the PDF in Figure 2.10).

E. SIMULATIONS OF ECHOES FROM SCATTERERS IN A RANDOM WAVEGUIDE

Random factors including small scale bottom roughness, surface wave action, and internal waves add a level of complexity to a real ocean environment that can only be simulated by adding a stochastic component to a simulation. In order to simulate a realistic ocean environment, internal waves are included in this model as a well understood source of random variability. A shallow water model of diffuse internal waves was incorporated into the two-way PE model[63] to add realistic, range-dependent perturbations to the sound-speed profile (Figure 2.2, right panel). The effects of incorporating this stochastic component is investigated for a single and multiple scatterers in a directional sonar beam.

1. Single Scatterer in a Directional Beampattern in the Vertical Plane (Case E, Table 2.3)

The gross effects on the forward propagation field of adding a stochastic, range-dependent sound-speed profile are two-fold. First, a significant portion of the energy is seen to leak into the shadow zone as can be seen in the transmission loss plot (Figure 2.6d). Second, the strongly coherent directional beam, seen in the deterministic case, begins to fragment into a more complex sound field. Commensurate effects can be seen in the statistics of the pressure field when randomly sampling in depth and in the statistics of the echoes from randomly positioned scatterers in depth. In the shadow zone (0–40 m) the echo PDFs are, again, strongly non-Rayleigh and non-exponential at ranges from 500 m to 9.5 km. The primary difference from the deterministic case (Figure 2.9) is that the tail is consistently elevated out to higher amplitudes in the stochastic case (Figure 2.11). This is most likely due to the strong leakage of energy into the shadow zone. In the energetic zone (40–100 m) the effect of the internal waves is to drive the pressure field to saturation more rapidly than the deterministic case. The pressure field reaches saturation at a range of 3.5 km ($p_{\text{real}}/p_{\text{imag.}}$ = 0.37/0.45) and all simulations at ranges from 3.5 km and farther closely match the Rayleigh PDF ($d_{\text{KL}} \leq 2.18\times10^{-2}$ – figures not shown). The effect of this is seen in the echo PDFs where the tails are very close to exponential at all ranges from 500 m to 9500 m (Figure 2.11). Furthermore, the Kullback-Leibler distance decreases at each consecutive range step that was simulated reducing from 3.53×10^{-2} at 500 m to 3.01×10^{-2} at 9500 m.

2. Multiple Scatterers in a Directional Beampattern in the Vertical Plane (Case E, Table 2.3)

In order to investigate the effects of first-order scattering (i.e., scattering from acoustic waves directly from the source prior to interference from other scatterers) by multiple scatterers, the model setup in the previous section was applied to cases with a number of scatterers, *N*, ranging from 1 to 10. In these simulations *N* scatterers were randomly distributed, vertically, but horizontally on axis in the energetic zone (40–100 m) at a range of 10 km. The effect of increasing the number of scatterers is to drive the echo magnitude PDFs toward a Rayleigh distribution (Figure 2.12). Thus, for a saturated

or nearly saturated pressure field at the scatterer, the echo distribution for *N* scatterers is bounded by the exponential distribution for small *N* and a Rayleigh distribution for large *N*. These results are expected. With a saturated field, each random scatterer produces an independent contribution to the echo. The sum of many independent, identically distributed phasors produces a complex Gaussian PDF by the CLT (e.g., see Goodman, 1985).[51] Therefore, the echo magnitudes should become Rayleigh distributed. However, it is important to note that, although the distributions are clearly approaching a Rayleigh with increasing *N*, the echo PDF in the case of 10 scatterers still has a significantly elevated tail with respect to a Rayleigh PDF.

The most significant result of this portion of the analysis is to show that at relatively short ranges a realistic stochastic component such as diffuse internal waves, drives the echo statistics towards saturation; whereas, in the deterministic case the statistics remain clearly unsaturated. Clearly, this is a first-order effect that must be accounted for in accurately predicting ranges at which the pressure field and associated echo statistics become saturated.

F. SIMULATION OF ECHOES FROM SCATTERERS IN A THIN LAYER WITHIN A RANDOM WAVEGUIDE

In order to simulate a real world scenario with a surface ship based sonar ensonifying scatterers that aggregate in thin layers (e.g., zooplankton and fish), simulations were conducted with a directional source located at 10 m depth and scatterers located randomly within a 10 m thick layer. Of particular interest is the degree to which the echo magnitude PDFs are non-Rayleigh and how various parameters such as beampattern and scattering response effect these statistics. Two cases, with various numbers of scatterers randomly located in depth within a thin layer, were investigated: a shallow layer in the thermocline at 10–20 m and a deep layer near the bottom at 85–95 m (see horizontal white lines on Figure 2.13).

The primary result of moving the source depth to 10 m is to reduce the size of the shadow zone abutting the surface (Figure 2.13). The layers in which the scatterers are located in this analysis are in the energetic zone below this shallow shadow zone. In one case the difference in the energetic, convergence zones and the shadow zones located

horizontally between these convergence zones (see white arrows on Figure 2.13) is analyzed.

1. Single Scatterer in a Vertically Directional Beampattern (Case F, Table 2.3)

In order to analyze the range dependence of the echo characteristics, the scintillation index, SI, was chosen as a good measure of the degree to which echo statistics approach a saturated state. The SI is a particularly useful measure in this context as it is most sensitive to the high amplitude portion of the intensity PDF of a signal. The scintillation index is the normalized intensity variance of the randomly sampled intensity, $\hat{I}$, of a signal and is given as

$$\mathrm{SI} = \frac{\left\langle \hat{I}^2 \right\rangle}{\left\langle \hat{I} \right\rangle^2} - 1. \tag{2.26}$$

It is known that the scintillation index of a fully saturated (i.e., complex Gaussian) pressure field is one;[69] however, the SI may also be used to analyze the statistics of echoes measured at a receiver. Given a narrowband signal in a strong multipath environment, the pressure at a given position and time can be described by the sum of *k* individual paths, $P(\mathbf{r},t) = a_k e^{i\phi_k}$, with amplitude a_k and phase ϕ_k. It has been shown[54] that when phase variance is large Eq. (2.26) can be expressed in terms of the individual path amplitude, $\hat{a}$, as

$$\mathrm{SI} = 1 + \frac{1}{N}\left(\frac{\left\langle \hat{a}^4 \right\rangle}{\left\langle \hat{a}^2 \right\rangle^2} - 2 \right). \tag{2.27}$$

For the case of a single scatterer ($N = 1$) giving rise to exponentially distributed echo magnitudes, where the moments are

$$\langle \hat{a}^n \rangle = n! \langle \hat{a} \rangle^n, \tag{2.28}$$

substituting this result into Eq. (2.27) leads to a scintillation index of 5. These values (SI = 1 for a saturated pressure field at the scatterer location, and SI = 5 for the associated echoes in the case of a single scatterer) are then used as a measure of saturation (i.e., unsaturated - below the given value, partially saturated - above the given value, or

saturated - at the given value). The saturation value is shown in horizontal black lines in Figure 2.14.

Two depth layers were analyzed in this part of the investigation, 10–20 m and 85–95 m, in a 100 m deep waveguide. There are two primary range dependent effects seen in the intensity statistics of both the shallow and deep layers. First, the scintillation index rapidly decays towards saturation in all cases (i.e., both shallow and deep layers and both at the target range and at the receiver). This trend towards saturation is in agreement with the results seen in Sec II.F.1 where the trend towards saturation is largely driven by the increased randomness of the field with range due to the internal wave perturbations of the sound speed.

The second effect is that the SI is strongly periodic in all cases at short ranges (1–5 km) before becoming less so as the statistics approach saturation. A comparison between the transmission loss (Figure 2.13) and the SI (Figure 2.14) at the same ranges show that the minima in the SI correspond to the regions where the pressure field is strongly energetic (e.g., see downward pointing arrows in the shallow layer of Figure 2.13). Between these energetic zones, which occur in both the upper and lower layer, are significantly lower energy regions, or shadow zones. At short ranges, where these shadow zones are most prominent, there are peaks in the saturation index. This is largely due to the fact that the SI is normalized by the mean, which has a tendency to elevate the SI in regions of very low pressure values. An analysis of the energetic region is more illuminating. In all cases the SI begins slightly to well below saturation (i.e., in an unsaturated state) and rises to or above saturation into a partially saturated state before tending towards saturation.

In comparing the shallow and deep water cases it appears that the scattering from the deep layer approaches saturation at slightly shorter ranges. This is likely due to a difference in the structure and extent of the energetic zones. Near the surface the shape of this zone is influenced solely by the downward refracting sound-speed profile; whereas, near the bottom there is a combination of effects due to both refraction within the water column and reflection from the bottom.

2. Effects of an Azimuthally Directional Beampattern (Case G, Table 2.3)

a. Single Scatterer

In this section a final degree of sonar system complexity is added to the ensonifying system: an azimuthally-dependent beampattern. A single scatterer, randomly located in the beam within the shallow layer (10–20 m) is considered. In this analysis the results are divided into energetic and non-energetic (shadow zone) regions, horizontally, as described in the previous section and illustrated by white arrows in Figure 2.13.

Echo magnitude PDFs were generated for various ranges from 1 km to 9.125 km. These results were compared with the phasor summation calculations described in Eq. (2.19). As the phasor summation does not inherently capture waveguide propagation effects, two parameters were adjusted to account for these effects a priori: the range of elevation angles where the scatterer is located in the beam and the PDF of the scatterer response. The scatterer location in the beam is limited in elevation angle, ϕ_S, ϕ_R to a range of angles centered on the main lobe, while the azimuthal angle, θ_S, θ_R, is given the full range within the half-space (i.e., the main lobe and all side lobes). Limiting the elevation angle represents the loss of acoustic energy propagating at higher angles that is attenuated by bottom interactions. Several ranges of elevation angles were examined: the full beam (± π/2 radians), the main lobe and first side lobe, on axis (±0 radians), and a portion of the main lobe. The best results were produced with the angle limited to a portion of the main lobe, $\pm\phi_{\mathrm{SL}}$, where ϕ_{SL} is the angle where the source beampattern value first decreases to the amplitude of the highest side lobe. Additionally, the PDF of the scattering response, p_A, in the phasor summation calculation is drawn from an exponential distribution. This accounts for the squaring effect of the waveguide described in Sec. II.B.2 for a single scatterer in a saturated pressure field. The result is a very good estimate of the PE predictions at all ranges when the scatterer is located within the energetic zone and at long ranges for cases where the scatterer is located in the less energetic zone (Figure 2.15). At short ranges, where the less energetic region is a shadow zone, the phasor summation does not model the PDF well as the field is not saturated.

However, as the shadow zone fills in at ranges further from the source, the phasor summation predicts the PDF well ($d_{\mathrm{KL}} = 3.82\times10^{-3}$ at 9.125 km).

b. Multiple Delta Function Scatterers

In order to analyze the effects of first-order scattering by multiple scatterers on the echo statistics and the validity of the phasor summation method, the simulation parameters in the previous section were applied at a single range with multiple scatterers each with equal and fixed scattering responses. A range of 5.25 km was chosen where the echo statistics were determined to be near saturation ($N = 1, \mathrm{SI} = 5.22$). The tail of the predicted distributions is strongly non-Rayleigh in all cases (Figure 2.16). Notably, in the case of 10 scatterers the result is still highly non-Rayleigh with a significantly elevated tail. In comparison with the phasor summation, the results show excellent agreement for low values of N ($N \leq 5$, $d_{\mathrm{KL}} \leq 5.35\times10^{-3}$) and good agreement in the tail at all values of N studied. Comparisons were also made with the K distribution using method of moments to estimate the shape parameter.[70] In all cases the physics-based phasor summation method outperforms the K distribution fit to the PDFs.

In order to investigate the echo envelope distribution in the limit of many scatterers, calculations were made using the phasor summation method with $N = 1000$. In this case the distribution of echo envelopes approaches a Rayleigh distribution ($d_{\mathrm{KL}} = 1.87\times10^{-3}$ – figure not shown).

3. Extended, Finite-Sized Rayleigh Scatterers (Case H, Table 2.3)

In order to investigate the effects of including a scatterer with a realistic scattering response, a Rayleigh scatterer was simulated with 10 point scatterers located closely in space within a sphere with a 2.5 m radius. This geometry provides a spatial extent assumed to be sufficient to induce a Rayleigh-like scattering response (e.g., see Figure 2.10, bottom two panels). In all cases, for N ranging from 1 to 10, the PDFs of the echo magnitudes are strongly non-Rayleigh (Figure 2.17). The trend of the PDFs with increasing N is, for both the low and the high amplitude ends of the PDF, to decrease towards a Rayleigh distribution. Comparisons are made with the analytical form of the

Chu-Stanton theory as well as the mathematically equivalent numerical phasor summation. In these calculations the elevation angles of the scatterers, ϕ_S, ϕ_R, are limited to ϕ_{SL} as in the comparisons with the delta function scatterers. However, the distribution of the scattering response, p_A, is set to a Rayleigh distribution to model the scattering response of large, extended Rayleigh scatterers in a waveguide (see Sec. II.D.4). There is good agreement in all cases ($d_{KL} \leq 3.83\times10^{-2}$). In the case of N = 10, there is not as good agreement in the tail of the PDF; however, the theory still performs similarly or better than the K distribution in all cases.

Calculations using the phasor summation method were also made to investigate the echo envelope statistics in the limit of many scatterers. In this case of $N = 1000$ the distribution of echo envelopes approaches a Rayleigh distribution ($d_{KL} = 2.38\times10^{-3}$ – figure not shown).

In analyzing the K distribution results it is seen that the shape parameter (α_k), often used as a proxy for the number of scatterers in a sonar resolution cell,[25,41,47,71] does not follow a one-to-one relationship with the effective number of scatterers, N_{eff} (Figure 2.18). This effective number of scatterers is the product of the total number of scatterers in the half space and the fractional width of the beampattern. Although α_k shows a linear relationship with N there is a significant offset from the origin at $N = 0$ suggesting more information is needed than just the number of scatterers to predict a K distribution that fits the echo envelopes.

G. DISCUSSION AND CONCLUSIONS

1. Effects of a Shallow Waveguide

Two primary effects have been identified that are associated with echoes generated in a shallow, deterministic waveguide. First, in the case of an omni-directional source, reflections from the surface and the bottom rapidly drive the pressure field to saturation, and, hence, an envelope that is Rayleigh distributed, as seen by randomly sampling the pressure field in depth at a given range from the source (e.g., see cases A

and C). This result is independent of the two sound-speed profiles investigated (constant and depth-dependent Munk profile). Second, it is shown that, for a single scatterer, randomly located in depth in a multipath-saturated waveguide, the PDF of the echo magnitudes, before beampattern effects, is exponential given a constant scattering response and a monostatic sonar system. This result is caused by the squaring effect induced by reciprocal forward and back paths through the waveguide (Eq. [2.6]).

2. Effects of a Random Waveguide

One approach to simulate the realistic stochastic nature of sound propagation in an oceanic waveguide is to include sound-speed perturbations due to diffuse internal waves. In comparison with the case of a directional source in a deterministic waveguide (Case D, Figure 2.9), the case involving an internal wave field (Case E, Figure 2.11) shows a significantly more rapid trend towards saturation with range. This can be seen in the rapid convergence of the echo envelope PDF on the exponential distribution. In case D (deterministic waveguide) refraction of the acoustic energy in the sound channel (Figure 2.6c) limits the formation of multipath due to fewer boundary interactions which, in turn, prevents the one-way pressure field from reaching saturation at any of the ranges simulated (figure not shown). In fact, the echo envelope PDFs for scatterers located in the energetic zone show very little range dependence beyond 3.5 km (Figure 2.9, right panels). Case E, in contrast, illustrates how the random internal wave field drives the energetic portion of the one-way pressure field towards saturation with range (figure not shown) and the echo PDFs tend towards exponential for the case of $N = 1$ (e.g., Figure 2.11, right panels). This result has implications for modeling of echo statistics in a shallow water environment. Calculations of a narrow acoustic beam in the sound channel of a deterministic waveguide, without including the realistic randomness seen in oceanic environments, may predict an unsaturated field with little or no trend towards saturation which is likely inaccurate.

It should be noted that the inclusion of internal waves is only one way to induce randomness in the waveguide. There are other waveguide properties, such as a randomly rough bottom or sea surface, that can also be included in shallow water models which would produce randomized acoustic paths. It is expected that the primary effect of

including more than one stochastic waveguide property would be to cause the pressure field to reach saturation at shorter ranges.

An analysis of thin layers of scatterers ensonified by a shallow source in a stochastic waveguide (case F) illustrates how the combination of deterministic and stochastic waveguide characteristics affects the echo statistics. At short ranges, the scintillation index is strongly range-dependent (Figure 2.14), driven by the location of the scatterers with respect to the alternating energetic and shadow regions. These regions are generally deterministic formed by the refraction of the narrow acoustic beam as it is influenced by the mean sound-speed profile. However, stochastic internal wave perturbations of the sound-speed profile induce two effects that lead to range-independent statistics at farther ranges: (1) the shadow zones are filled in by fragmentation of the acoustic paths and (2) the interference of many paths leads to saturation. These two effects greatly simplify the prediction of the echo envelope distributions for scatterers far from the source by removing any significant range dependence when the number of scatterers within the sample volume is fixed.

3. Effects of a Directional Source

As has been shown by Chu and Stanton,[29] understanding the beampattern effects is crucial to accurately predicting echo statistics in the case of a small number of scatterers in a narrow beampattern. In this study the effects of the beampattern are split into the elevation-dependent component of the beampattern (i.e., simulations where the scatterer is located on the axis of the main lobe azimuthally, Cases D–F) and the azimuthal component (shown in the full beampattern cases, Cases G and H). With respect to the elevation-dependent component, the combination of a narrow beam in the vertical and a strongly depth-dependent sound-speed profile refracts most of the acoustic energy into the sound channel producing strong shadow zones (e.g., see Figure 2.6c). As discussed in the previous section, this combination also leads to significantly less deterministic multipath than in cases including an omni-directional source due to fewer boundary interactions. In these cases saturation is only likely to occur if other processes are present which help fragment the acoustic paths into a larger number of independent paths.

In cases of a stochastic waveguide (e.g., Case E), the rapid fragmentation of the acoustic paths seen in Figure 2.6d renders the elevation-dependent component of the beampattern less significant. This effect can be seen by the rapid trend of the echo envelope PDFs towards exponential-like distributions (right panels, Figure 2.11), which is nearly the same result that is seen in the multipath-saturated regime of the omni-directional sources (Figure 2.7 and Figure 2.8, lower panels). A closer examination of effects due to the elevation-dependent component of the beampattern is conducted in Case G by comparison with the phasor summation. Here the two-way PE model is used to predict the distribution of echo envelopes from scatterers located in a thin, shallow layer ensonified by a shallow source in a random waveguide. Comparison of these predictions with phasor summation calculations, in which the vertical beampattern is limited to various ranges of elevation angles from a single on-axis value to the full beampattern, shows the best fit when limiting the acoustic beam to the main lobe (Case G). So, while the attenuation of high angle energy reduces the influence of well off-axis beampattern values, the echo envelope distribution is still influenced by the elevation-dependent main lobe of a narrow acoustic beam.

The horizontal component of the beampattern has a strong and consistent effect on the echo envelope statistics at all ranges, though it must be noted that out-of-plane scattering has been ignored in this treatment. The full beampattern case with the source at 10 m clearly shows the effect (Case G). Here it is shown that the PE predictions of echo envelope distributions converge on the phasor summation calculations which account for the azimuthally dependent beampattern (Figure 2.15). Importantly, the combination of a directional sonar beam and a single scatterer, with a constant scattering response, located in a randomized waveguide produces a highly non-Rayleigh and non-exponential PDF. The contribution of the azimuthally dependent beampattern, in particular, contributes to the tail of the PDF remaining highly elevated over the exponential distribution which would otherwise be predicted for a non-directional beam with a single scatterer in a saturated pressure field. It is expected, though, that significant horizontal variation in the sound-speed profile would lessen the effect of the azimuthal beampattern component.

When multiple, independent scatterers are ensonified by a directional source in a random waveguide the echo envelope PDF trends strongly towards a Rayleigh distribution (e.g., Figure 2.12, elevation-dependent beampattern component). Importantly, in the case where the beam is narrow in both elevation and azimuth the trend toward a Rayleigh distribution with increased number of scatterers is much more gradual (Figure 2.16).

4. Extended Scatterers with a Variable Scattering Response in a Waveguide

It is shown in this study that a single scatterer with a fixed scattering response located in a saturated environment produces echo envelopes that are exponentially distributed (Case A). However, in nature, the scattering response is often variable. One commonly observed response is a complex Gaussian distribution which arises from many scatterers, all with scattering responses of the same amplitude and random phase, contributing to a single echo (e.g., a compact school of single-sized fish ensonified near swimbladder resonance). This response induces echo envelopes that are Rayleigh distributed in the absence of waveguide or beampattern effects and leads to the term *Rayleigh scatterer*.

A Rayleigh scatterer in a saturated pressure field of a shallow waveguide is examined in Case B, where the distribution of echo envelopes is shown to be sensitive to the size of the scattering volume. While an infinitesimally small Rayleigh scatterer (i.e., a point scatterer with a complex Gaussian response) in a waveguide has a highly non-Rayleigh echo envelope distribution, an extended Rayleigh scatterer of this nature has an increasingly Rayleigh-like distribution with increasing size (Figure 2.10). The reason for this dependency, shown mathematically in Sec. II.D.4, is related to the relative size of the scattering volume with respect to the distance at which the one-way pressure field becomes uncorrelated. For a very small scatterer the amplitude of the entire scattering volume is modulated by the waveguide response which is exponentially distributed. However, in the limit of a large scatterer, different regions of the scattering volume are modulated independently, further randomizing the contribution from various regions of the scattering volume. Following the CLT, then, the summation of the contributions from

various regions of scattering volume results in echo envelopes that are Rayleigh distributed. In practice the ensonified volume contributing to a single echo is dependent on the sonar source and receiver beamwidths and the source waveform. So, this dependence on the size of the scattering volume is only expected while the scatterer is smaller than the spatial resolution of the sonar system.

5. Modeling Echo Envelopes in an Acoustic Waveguide

A key result of this analysis is that the echo statistics of a collection of scatterers in a complex oceanic environment may be modeled, in some cases, with a fairly simple and computationally low-budget model such as the phasor summation method described Sec. II.C.3. The requirements are that the scatterers are located in an energetic zone of the waveguide and at a range where the pressure field is saturated. Knowledge then is required of the beampattern, the number of scatterers in the beam at a given range, and the scattering response (e.g., constant or complex Gaussian). The predicted PDFs for the various cases studied with scatterers located in a saturated waveguide are presented in Table 2.4. In nearly all cases studied the Chu-Stanton theory or the mathematically equivalent phasor summation method outperformed the K distribution in predicting echo statistics from water column scatterers in a shallow waveguide. Furthermore, it is shown that, in the case of N scatterers randomly distributed in a directional beam, the shape parameter of a K distribution that most closely fits the data cannot be predicted solely from the number of ensonified scatterers.

Future work in this realm could include comparison with data collected from scattering by aggregations of volume scatterers in the water column such as schools of fish or bubble clouds. Modeling could include broadband or narrowband simulations that incorporate extended scatterers representing realistically shaped aggregations and non-Rayleigh scatterers. An additional area that could be explored is the effect of out-of-plane scattering on echo envelope PDFs in the case of a directional source with an azimuthally dependent beampattern.

Parameter	Value
Latitude (degrees north)	42
# of Internal Wave Modes (j_{max})	15
Mode parameter (j^*)	1
Internal wave displacement (ζ_0 , m)	6

Table 2.1. Shallow water internal wave modeling parameters.

Parameter	Value
Sonar System Parameters	
Source Type	circular piston (ka = 37.06)
Source Depth (m)	1500
Frequency (kHz)	3
Receiver Type	circular piston (ka = 37.06)
Receiver Depth (m)	1500
Scatterer Parameters	
range from sonar (m)	1000
Location within Beam	limited to range $[0, \theta_{SL}]$
Scattering Response	Rayleigh PDF
Environmental Parameters	
Sound-speed Profile (m/s)	1500 (constant)
Water Depth (m)	3000
Bottom Density (kg/m^3)	1000
Bottom Speed (m/s)	1500
Bottom Attenuation (dB/wavelength)	200
Parabolic Equation Model Parameters	
Range Step (m)	5
Depth Step (m)	0.05
# of Padé Terms	4

Table 2.2. Model parameters simulating direct path geometry.

CASE	A	B	C	D	E	F	G	H
Source / Receiver Parameters								
Source Type (note 1)	omni	omni	omni	beam	beam	beam	beam	beam
Source Depth	50 m	50 m	50 m	50 m	50 m	10 m	10 m	10 m
Frequency	3 kHz	3 kHz	3 kHz	3 kHz	3 kHz	3 kHz	3 kHz	3 kHz
Receiver Type (note 2)	omni	omni	omni	omni	omni	omni	omni	omni
Receiver Depth	50 m	50 m	50 m	50 m	50 m	10 m	10 m	10 m
Scatterer Parameters								
Location (note 3)	N/A	N/A	N/A	on axis	on axis	on axis	full beam	full beam
Response (note 4)	delta function	Rayleigh	delta function	delta function	delta function	delta function	delta function	Rayleigh
Environmental Parameters								
SSP (note 5)	constant	constant	Munk fit	Munk fit	Munk fit	Munk fit	Munk fit	Munk fit
Internal Waves (note 6)	no	no	no	no	yes	yes	yes	yes

Notes: 1) The source type is either omni-directional ("omni") or a circular piston (ka = 37.06) with a narrow beam ("beam").
2) The receiver type is omni-directional ("omni") in all cases.
3) The scatterer location in the beam is either in a vertical plane (i.e., azimuthally "on axis"), or randomly located vertically and azimuthally ("full beam"), or not applicable ("N/A").
4) The scattering response denotes a scattering magnitude that is either fixed at unity ("delta function") or Rayleigh distributed ("Rayleigh").
5) The water column sound speed is either a constant 1500 m/s ("constant") or an analytical fit of a Munk sound-speed profile to an observed shallow water profile ("Munk Fit").
6) A "yes" for internal waves indicate that the sound-speed profile is perturbed every 10 m with a shallow water internal wave model.

Table 2.3. Key modeling parameters used in numerical simulations. Parameters which were constant throughout all simulations include bottom characteristics: density = 2000 kg/m^3, sound speed = 1600 m/s, and attenuation = 0.5 dB/wavelength; and PE modeling parameters: range step = 1 m, depth step = 0.025 m, and number of Padé terms = 8.

Without Beampattern Effects					
N	**Scattering Response**	**Scatterer Spatial Extent**	**PDF**		
1	delta	point	exponential		
1	Rayleigh	point	PDF associated with the product of an exponentially distributed random variable and a Rayleigh distributed random variable		
1	Rayleigh	extended	Rayleigh (in limit of large spatial extent)		
With Beampattern (BP) Effects					
N	**Scattering Response**	**Scatterer Spatial Extent**	**Vertically Directional BP**	**Horizontally Directional BP (note 1)**	**PDF**
1	delta	point	yes	no	exponential
$\gg 1$	delta	point	yes	no	approaches Rayleigh O($N \approx 10$)
1	delta	point	yes	yes	highly elevated tail (note 2)
$\gg 1$	delta	point	yes	yes	approaches Rayleigh O($N \approx 1000$)
1	Rayleigh	extended	yes	yes	highly elevated tail (note 2)
$\gg 1$	Rayleigh	extended	yes	yes	approaches Rayleigh O($N \approx 1000$)

Notes:
1. No out-of-plane scattering considered.
2. Distribution with high-amplitude portion elevated above Rayleigh and exponential distributions.

Table 2.4 Predicted echo envelope PDFs for various cases of a monostatic sonar system with *N* scatterers positioned randomly in a saturated pressure field.

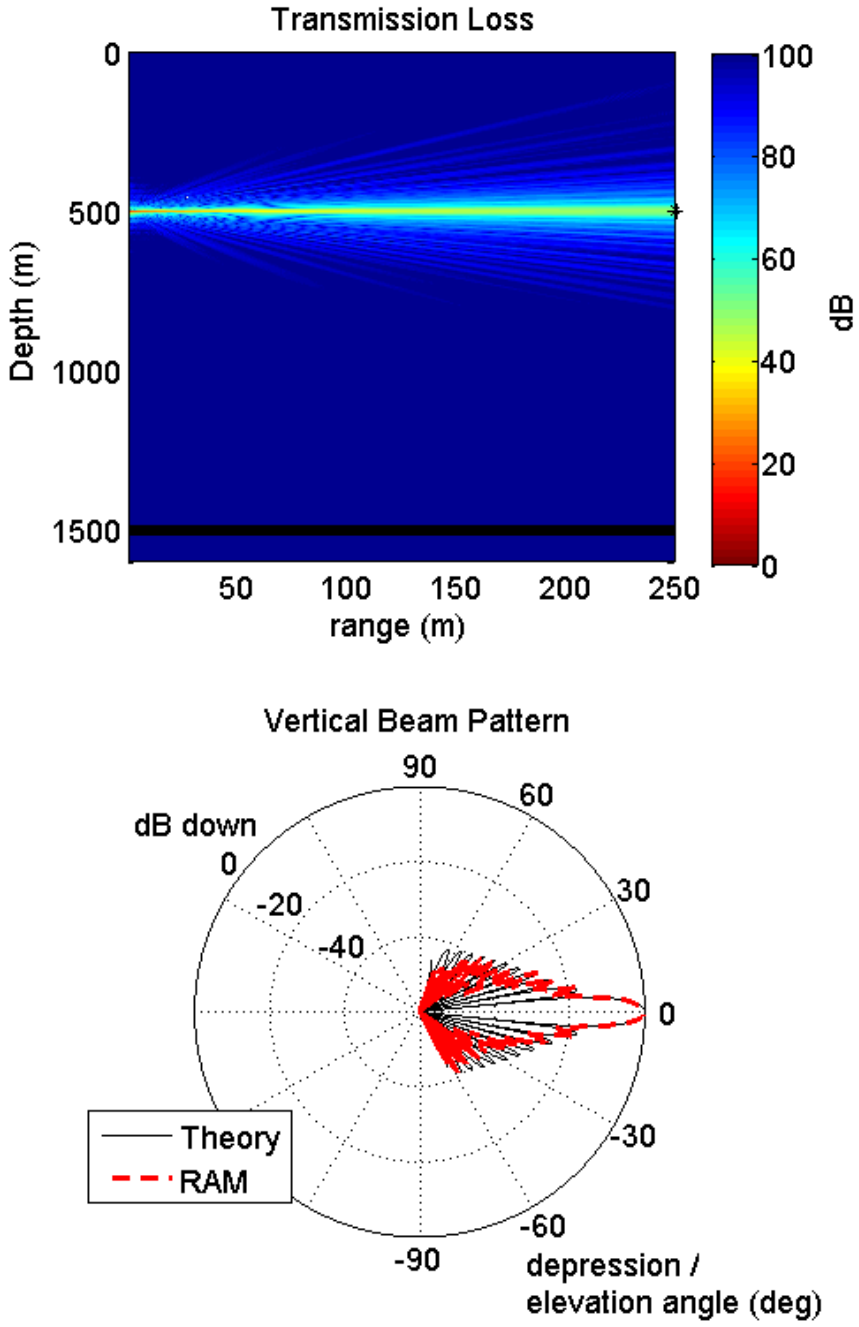

Figure 2.1 Benchmark test of parabolic equation starter field modeling a circular piston ($ka = 32.06$). Top panel shows propagation of narrow 5° beam in a constant sound-speed ($c = 1500$ m/s) environment. Bottom panel shows comparison of intensity at a range of 250 m between PE model (red dashed line) and theory (black solid line). Model parameters: range step = 0.5 m, depth step = 0.025 m, number of Padé terms = 8.

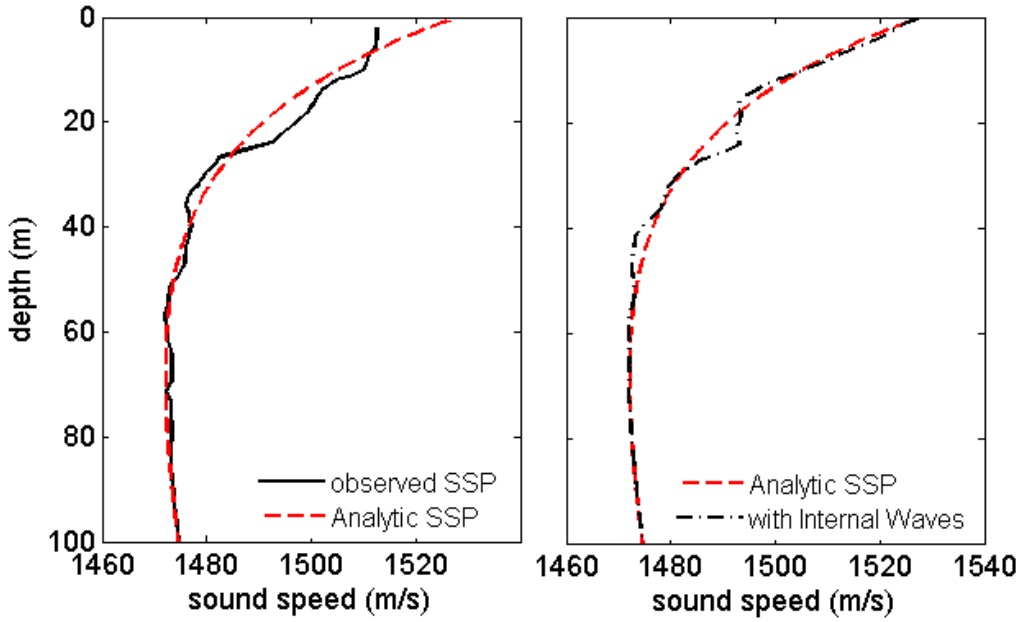

Figure 2.2 Munk sound-speed profile fit to observed data, with and without internal waves. Left panel shows a shallow water sound-speed profile measured in the Gulf of Maine in September of 2010 truncated at 100 m depth (solid black line) and a canonical Munk sound-speed profile fit to the measured data (dashed red line in both panels). Right panel shows a single realization of the same analytic Munk profile perturbed by diffuse internal waves (black dot-dashed line) as predicted by an empirically validated, shallow water internal wave model.[63]

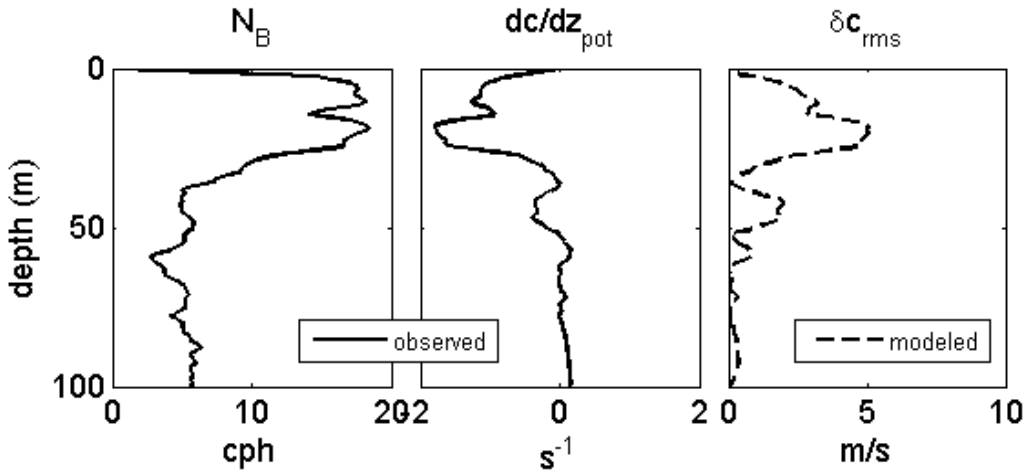

Figure 2.3 Observed water column profiles from 2010 Gulf of Maine cruise. Buoyancy frequency and the derivative of potential sound speed with depth (left and center panel, respectively). Modeled range-averaged, rms sound-speed perturbation (right panel).

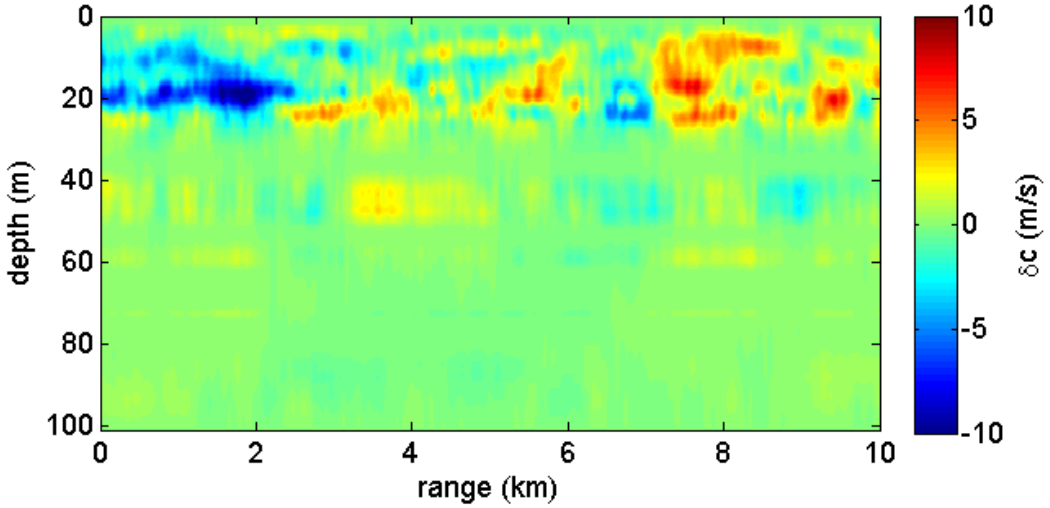

Figure 2.4 Predicted sound-speed perturbation due to diffuse, broadband internal waves in shallow water using an empirically validated model.[63]

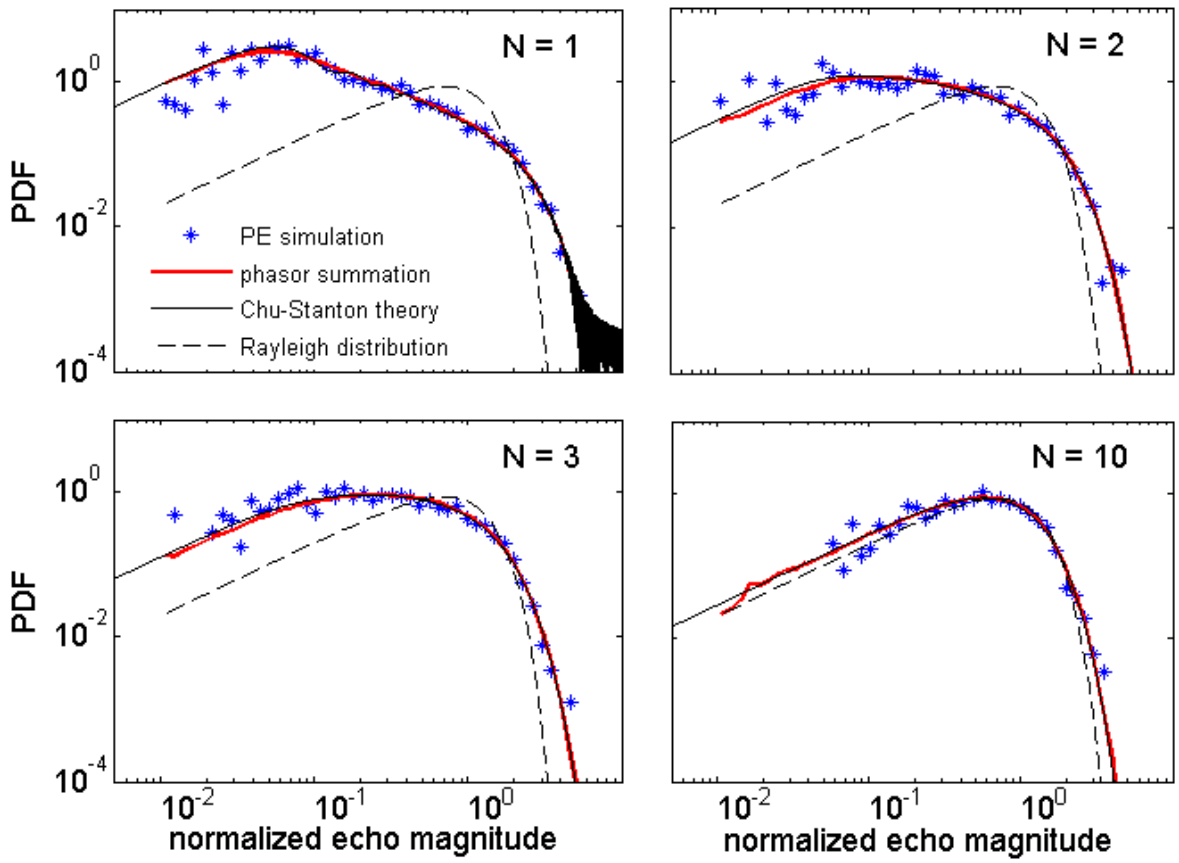

Figure 2.5 Predicted echo PDFs of various numbers of scatterers, each with a Rayleigh distributed scattering amplitude, randomly located in the main lobe of a directional sonar beam (3 kHz source with a 5° beamwidth) in a direct path geometry. Blue asterisks are predictions using the two-way PE simulation at a range of 1 km, red dashed line is numerical phasor summation which incorporates beampattern effects, black solid line is theoretical curve,[29] and the dashed black line is a Rayleigh distribution. The number of scatterers, *N*, is given in the top right of each panel.

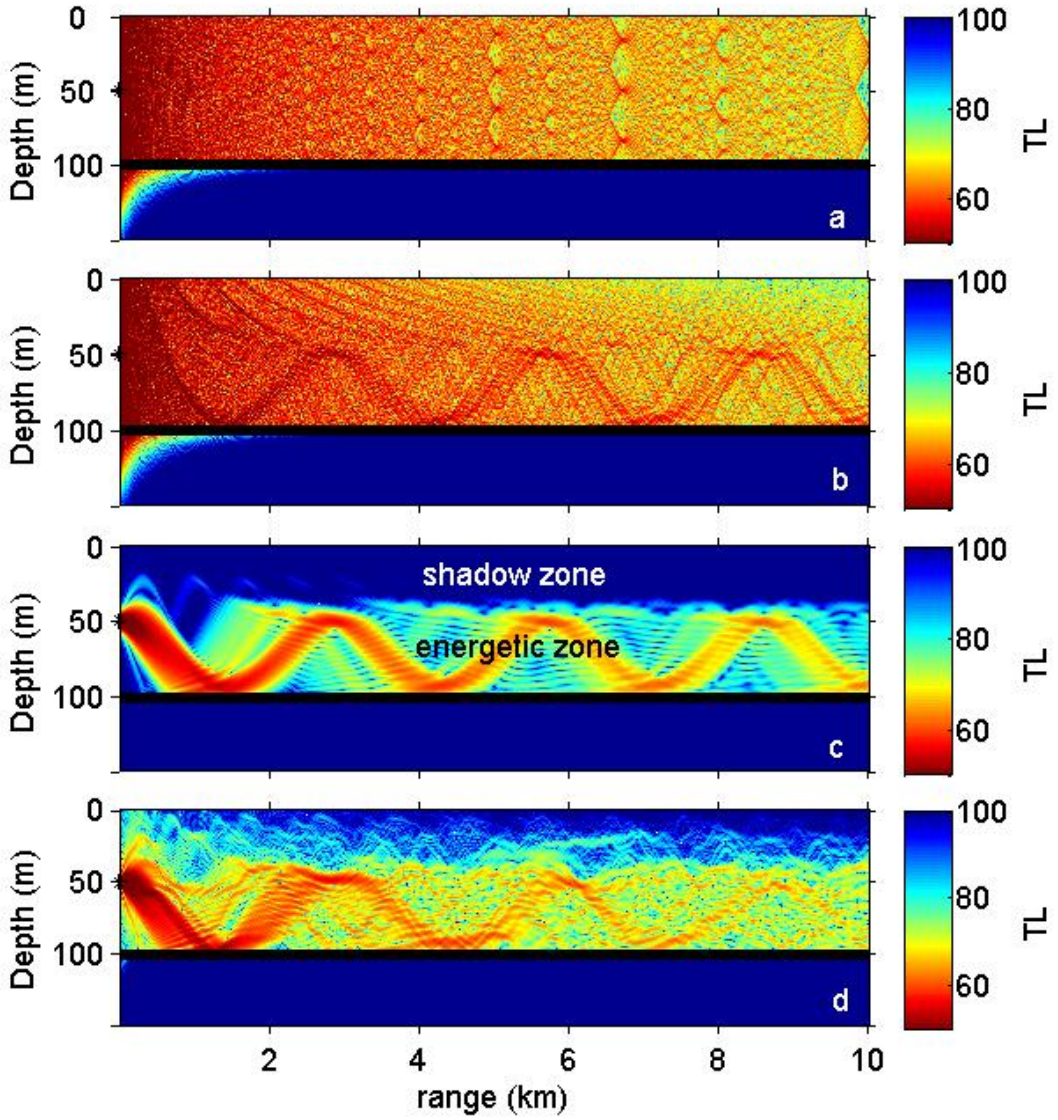

Figure 2.6 Predicted transmission loss from a 3 kHz source in an oceanic waveguide with varying levels of complexity. (a) omni-directional source, constant sound-speed profile; (b) omni-directional source, canonical Munk sound-speed profile; (c) directional source, Munk sound-speed profile; (d) directional source, Munk sound-speed profile with internal wave perturbations. In (c) and (d) the directional source is a circular piston (ka=37.06) with a narrow beam (5° 3dB beamwidth).

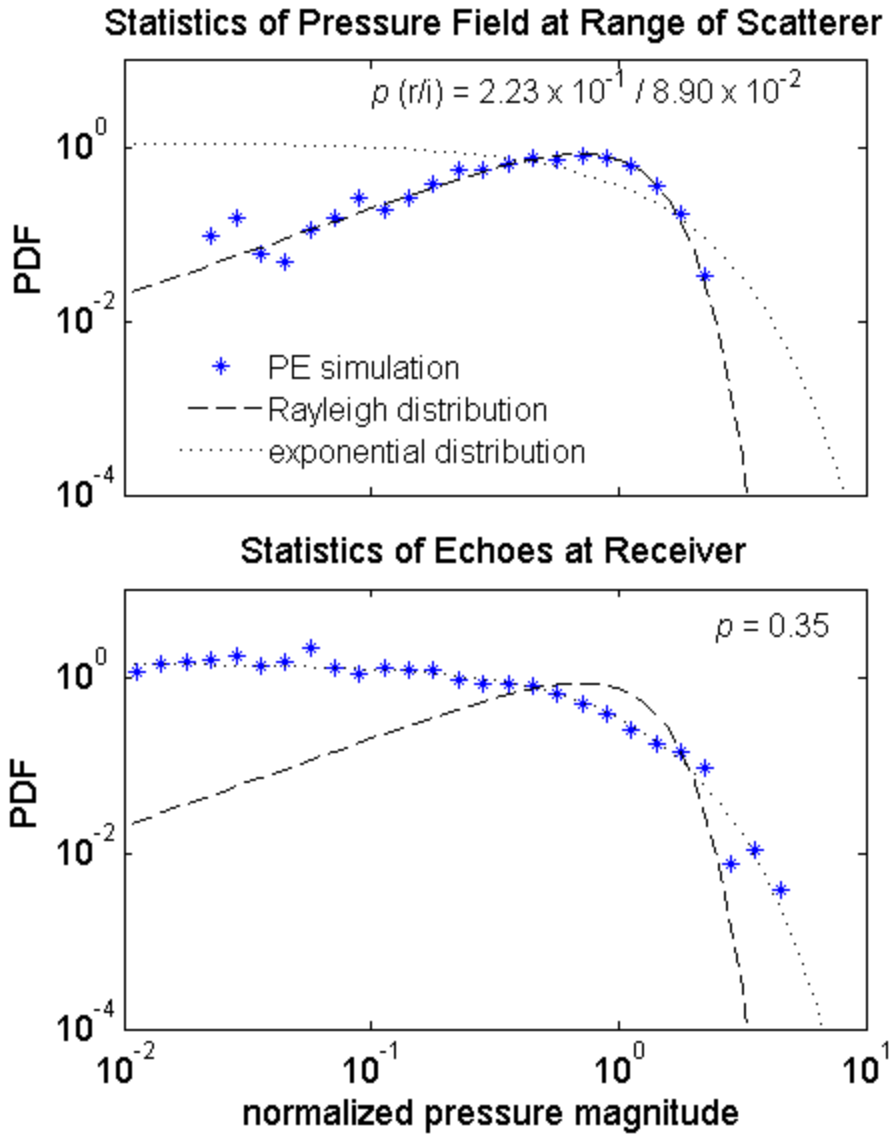

Figure 2.7 Predicted PDFs associated with a 3 kHz *omnidirectional source* at a depth of 50 m ensonifying a single scatterer randomly located in depth at a range of 1000 m in a waveguide with a *constant sound-speed profile*. The scatterer response is a constant. Top panel is the PDF of the magnitude of the pressure field at the scatterer's random location and the bottom panel is the PDF of the echo envelope at the receiver. Lilliefors test *p*-values for comparison with the Rayleigh distribution (top panel) and the exponential distribution (bottom panel) are given in the top-right corner of each panel.

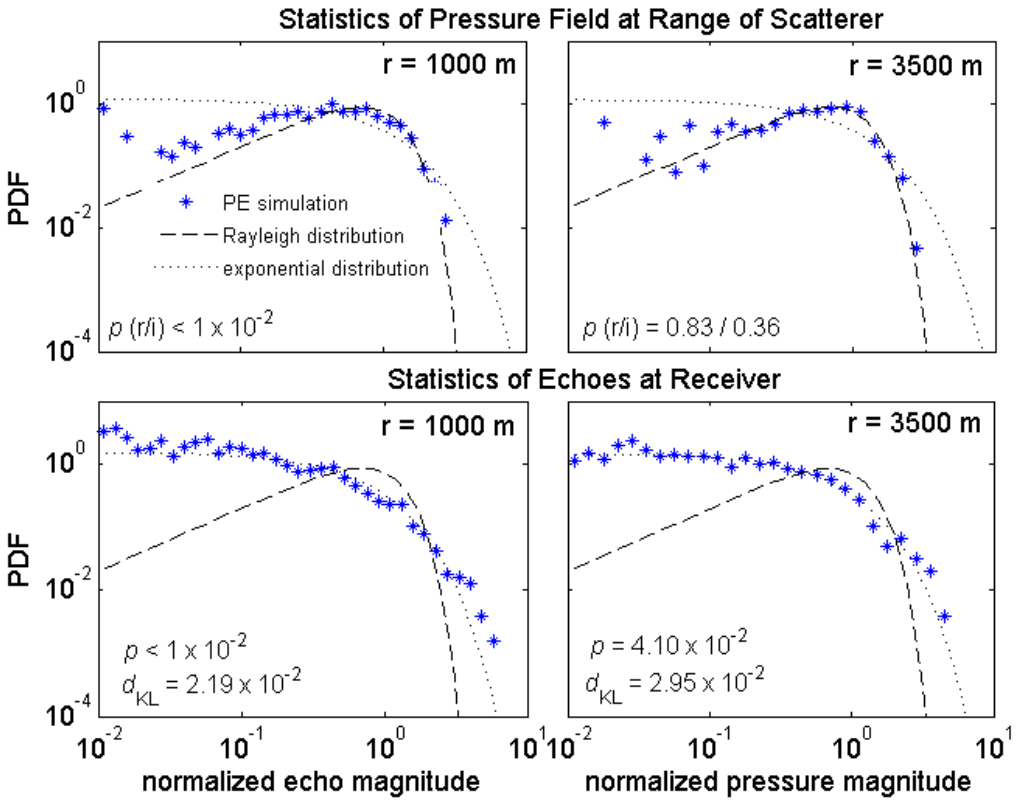

Figure 2.8 Predicted PDFs associated with a 3 kHz *omnidirectional source* at a depth of 50 m ensonifying a single scatterer randomly located in depth at a range of 1000 m (left two panels) and 3500 m (right two panels) in a waveguide with a *canonical Munk sound-speed profile*. The scatterer response is a constant. Top two panels give the statistics of the magnitude of the pressure field at the scatterer's random location; while, bottom two panels give the statistics of the echo envelope at the receiver. Lilliefors test *p*-values for comparison with the Rayleigh distribution (top panels) and the exponential distribution (bottom panel) are given in the bottom left corner of each panel. Kullback-Leibler distances comparing model predictions with the exponential distribution, d_{KL}, are given in the bottom left corner of the bottom panels.

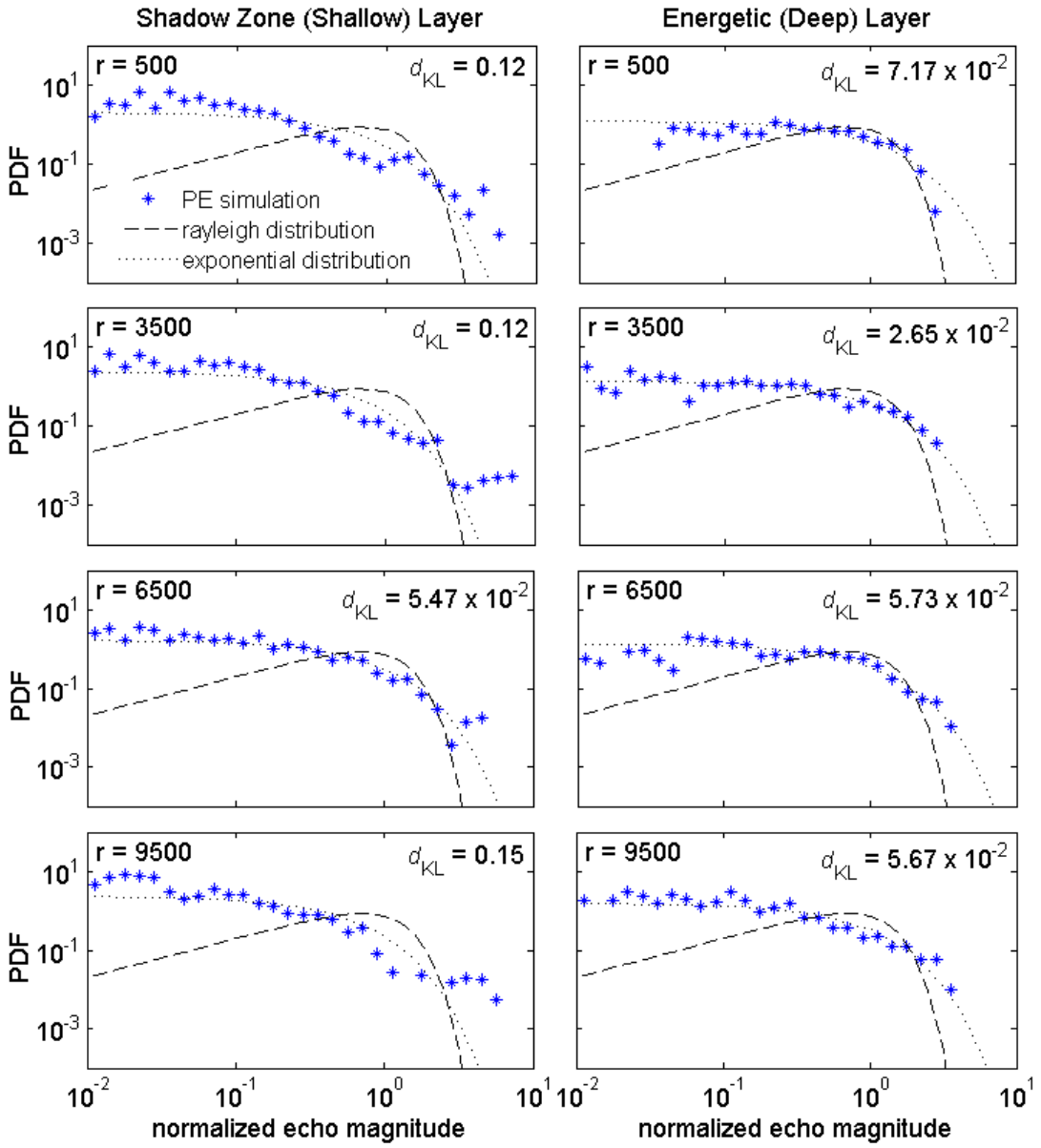

Figure 2.9 Predicted echo PDFs associated with a 3 kHz *directional source* at a depth of 50 m ensonifying a single scatterer located *azimuthally on axis* and randomly in depth at various ranges in a waveguide with a *canonical Munk sound-speed profile*. The panels on the left give the statistics of the shadow zone (0 to 40 m), and the panels on the right give the statistics of the energetic zone (40 to 100m). The range of the scatterer, r, is given in the top left of each panel. The directional source is a circular piston (ka=37.06) with a narrow beam (5° 3dB beamwidth) and the scatterer response is a constant. Kullback-Leibler distances comparing model predictions with the exponential distribution, d_{KL}, are given in the top-right corner of each panel.

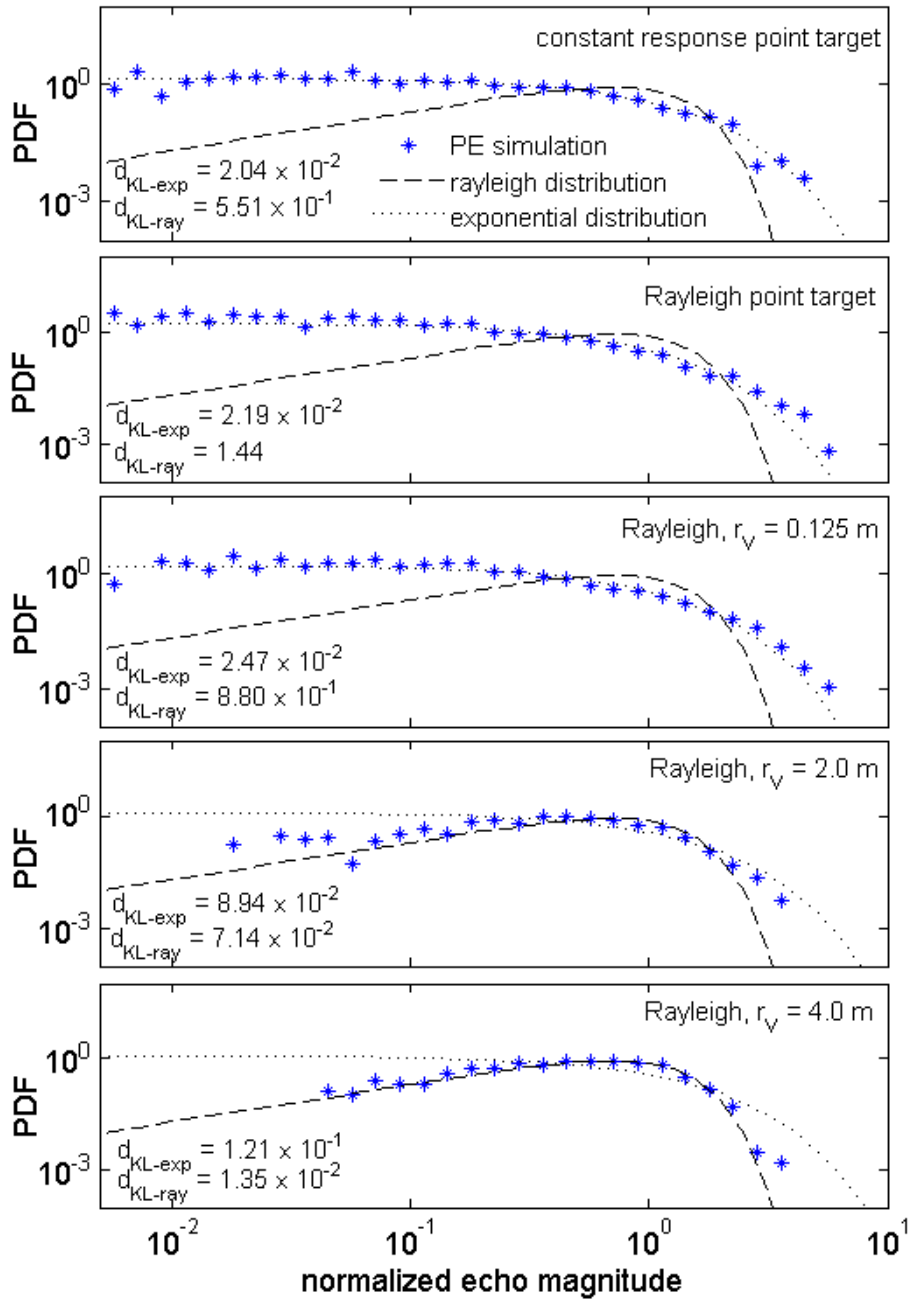

Figure 2.10 Predicted echo PDFs associated with a 3 kHz omnidirectional source at a depth of 50 m ensonifying a single spherical Rayleigh scatterer of various radii, r_v. The scatterer is randomly located in depth at a range of 1000 m in a waveguide with a constant sound-speed profile. Top panel is the PDF of a delta scatterer with the same parameters for comparison. Kullback-Leibler distances comparing model predictions with the exponential distribution, $d_{KL\text{-}exp}$, and the Rayleigh distribution, $d_{KL\text{-}ray}$,are given in the bottom left corner of each panel.

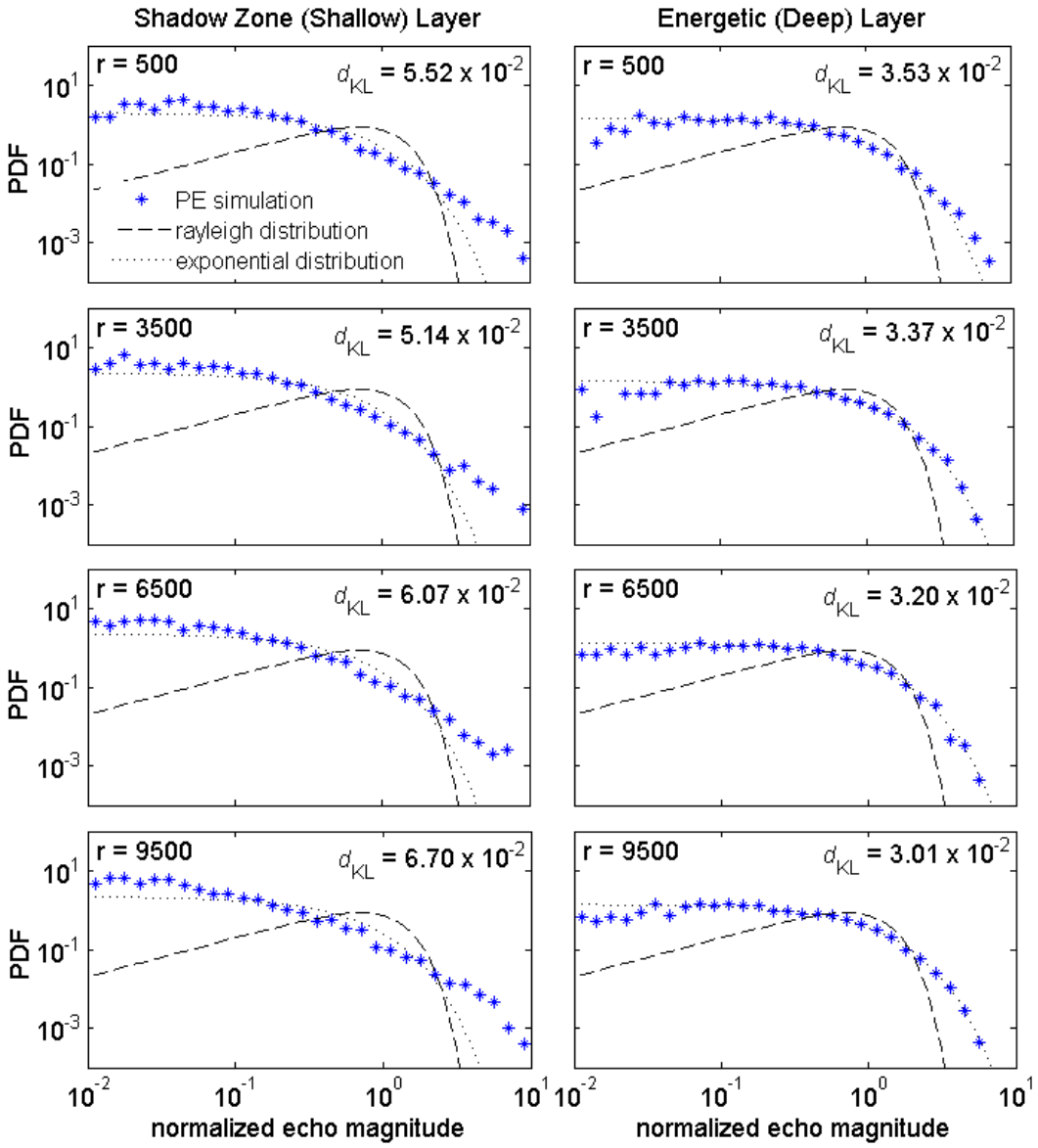

Figure 2.11 Predicted echo PDFs associated with a 3 kHz *directional source* at a depth of 50 m ensonifying a single scatterer located *azimuthally on axis* and randomly in depth at various ranges in a *random waveguide* with a canonical *Munk sound-speed profile* perturbed by diffuse internal waves. The panels on the left give the statistics of the shadow zone (0 to 40 m), and the panels on the right give the statistics of the energetic zone (40 to 100m). The range of the scatterer, r, is given in the top left of each panel. The directional source is a circular piston (ka=37.06) with a narrow beam (5° 3dB beamwidth) and the scatterer response is a constant. Kullback-Leibler distances comparing model predictions with the exponential distribution, d_{KL} ,are given in the top-right corner of each panel.

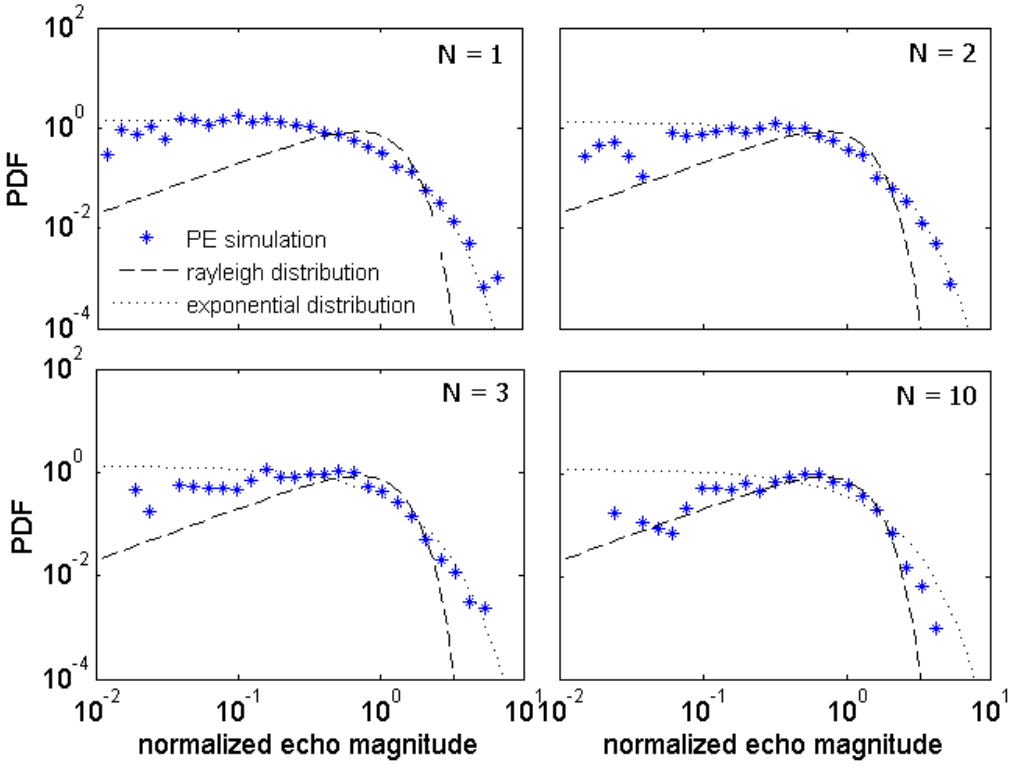

Figure 2.12 Predicted echo PDFs associated with a 3 kHz *directional source* at a depth of 50 m ensonifying various numbers of scatterers. The scatterers are located *azimuthally on axis* and randomly in depth in the energetic zone (40–100m depth) at a range of 10 km in a random waveguide. The directional source is a circular piston (ka=37.06) with a narrow beam (5° 3dB beamwidth). The number of scatterers, *N*, is given in the top right of each panel. The scatterers are at a range of 10 km in all cases and have a constant scattering response.

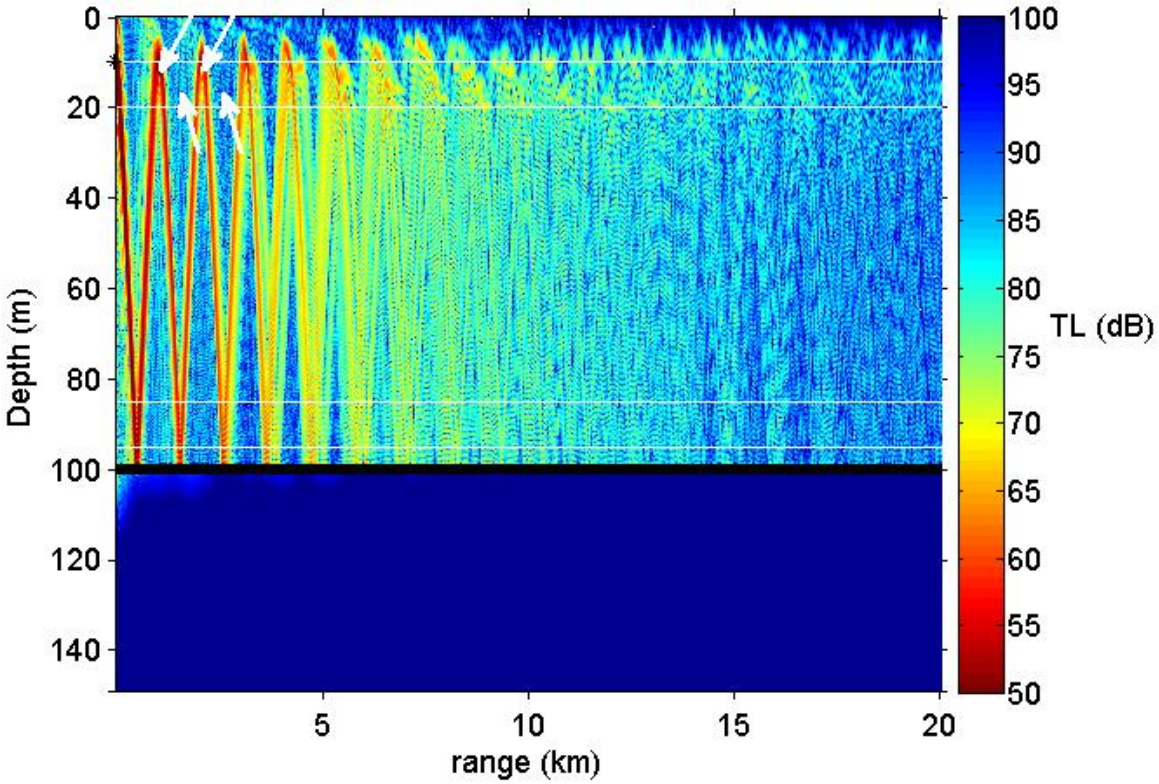

Figure 2.13 Predicted transmission loss from a 3 kHz directional source located at 10 m depth in a random waveguide. The waveguide has a Munk sound-speed profile perturbed by diffuse internal waves. The directional source is a circular piston (ka=37.06) with a narrow beam (5° 3dB beamwidth). Pairs of white lines represent the boundaries of two layers used in the analysis: a shallow layer (10–20 m) and a deep layer (85–95 m). Arrows depict convergence zones (top two arrows) and shadow zones (bottom two arrows).

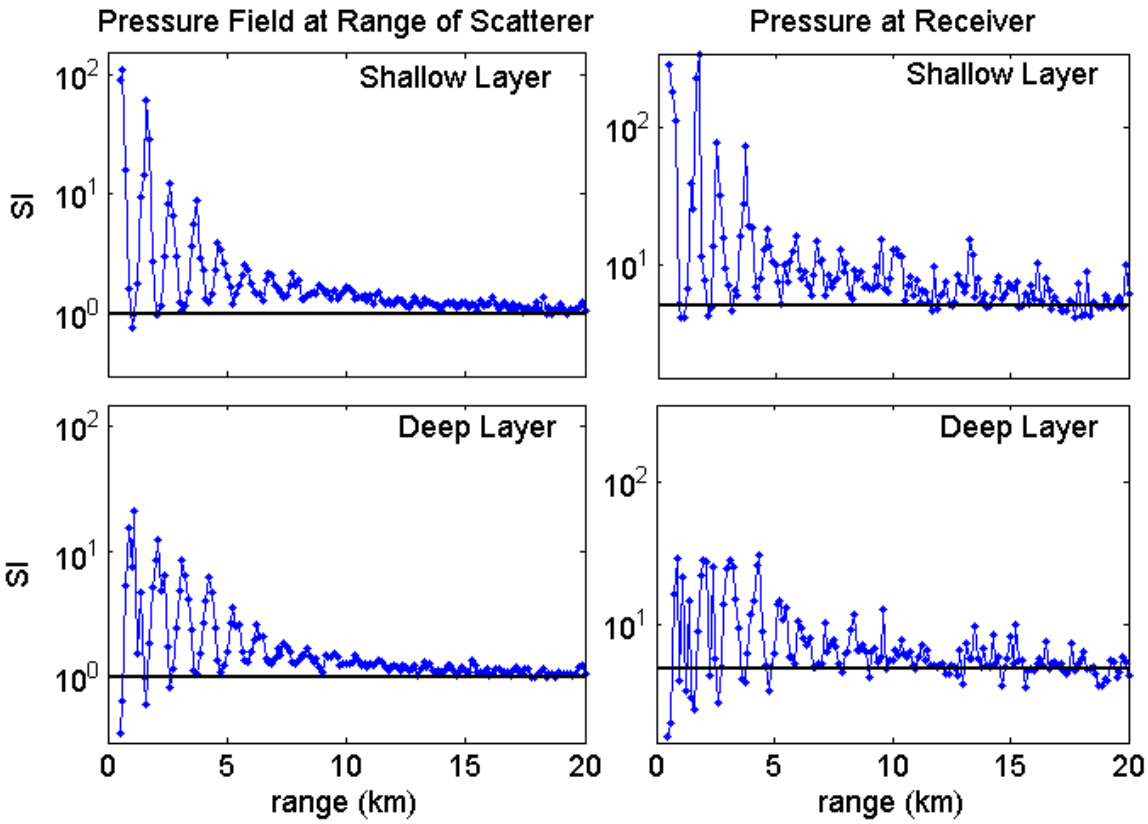

Figure 2.14 Predicted normalized intensity variance (scintillation index, SI) associated with a 3 kHz directional source at 10 m depth ensonifying a single scatterer randomly located azimuthally on axis in a thin layer in a random oceanic waveguide. The top two panels are for a scatterer in a shallow layer between 10 and 20 m depth; while, the bottom two panels are for a scatterer in a deep layer between 85 and 95 m depth. The left two panels give the SI of the pressure field at the scatterer's random location; while, the right two panels give the SI of the echoes at the receiver. The solid lines are the theoretical SI for a phase saturated pressure field (SI = 1 for the case of a Rayleigh distributed pressure magnitude at the scatterer location, and SI = 5 for exponential distributed echo magnitudes at the receiver).

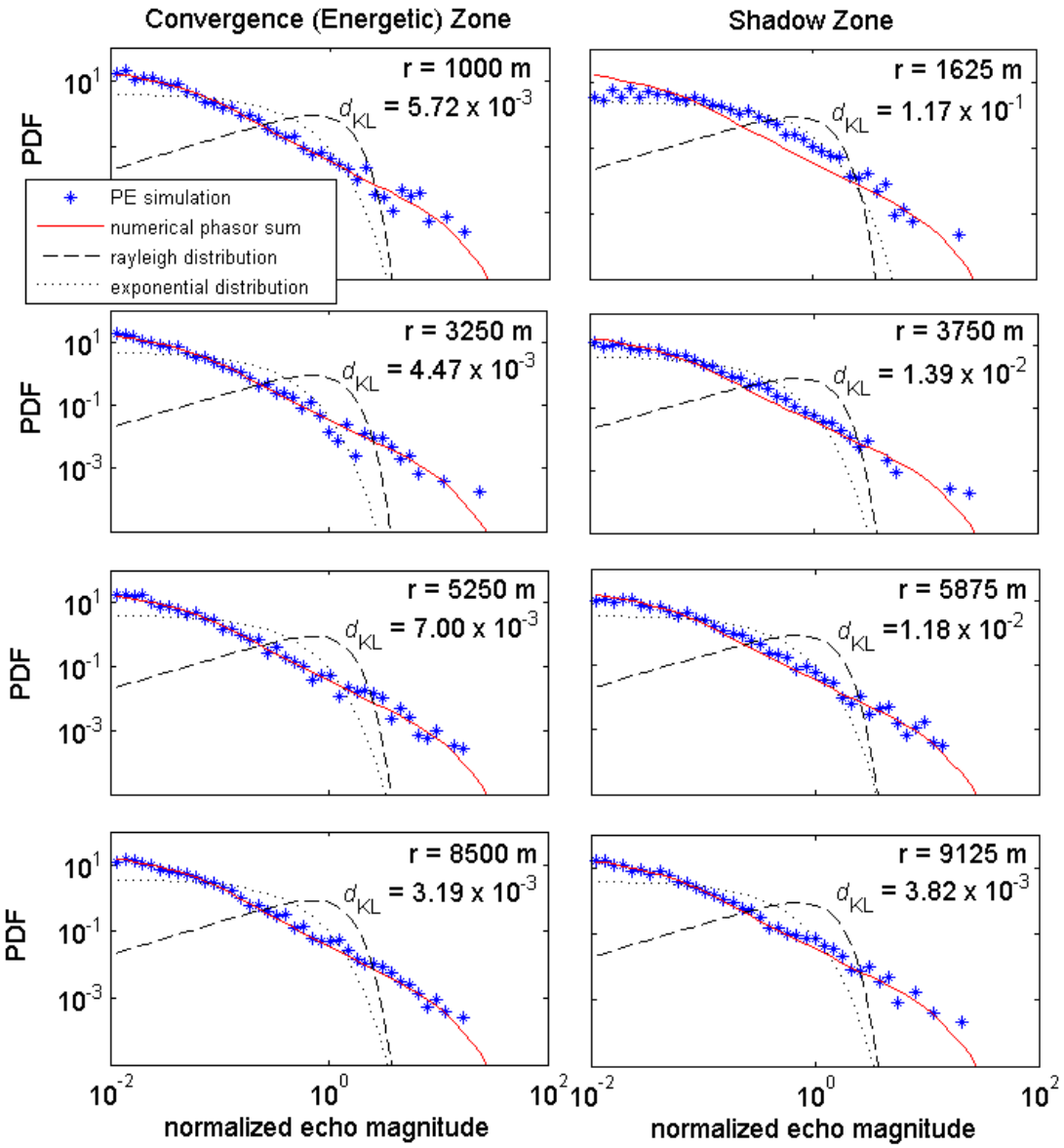

Figure 2.15 Predicted echo PDFs associated with a 3 kHz directional source at a depth of 10 m ensonifying a single scatterer randomly located within the full 180° beampattern, azimuthally, and in a shallow thin layer vertically (10–20 m), in a random oceanic waveguide. The panels on the left give the statistics associated with the convergence zones and the panels on the right give the statistics of the shadow zones. The range of the scatterer, *r*, is given in the top right of each panel. The directional source is a circular piston (ka=37.06) with a narrow beam (5° 3dB beamwidth) and the scatterer response is a constant. Kullback-Leibler distances comparing PE predictions with phasor sum predictions, d_{KL}, are given in the top-right corner of each panel.

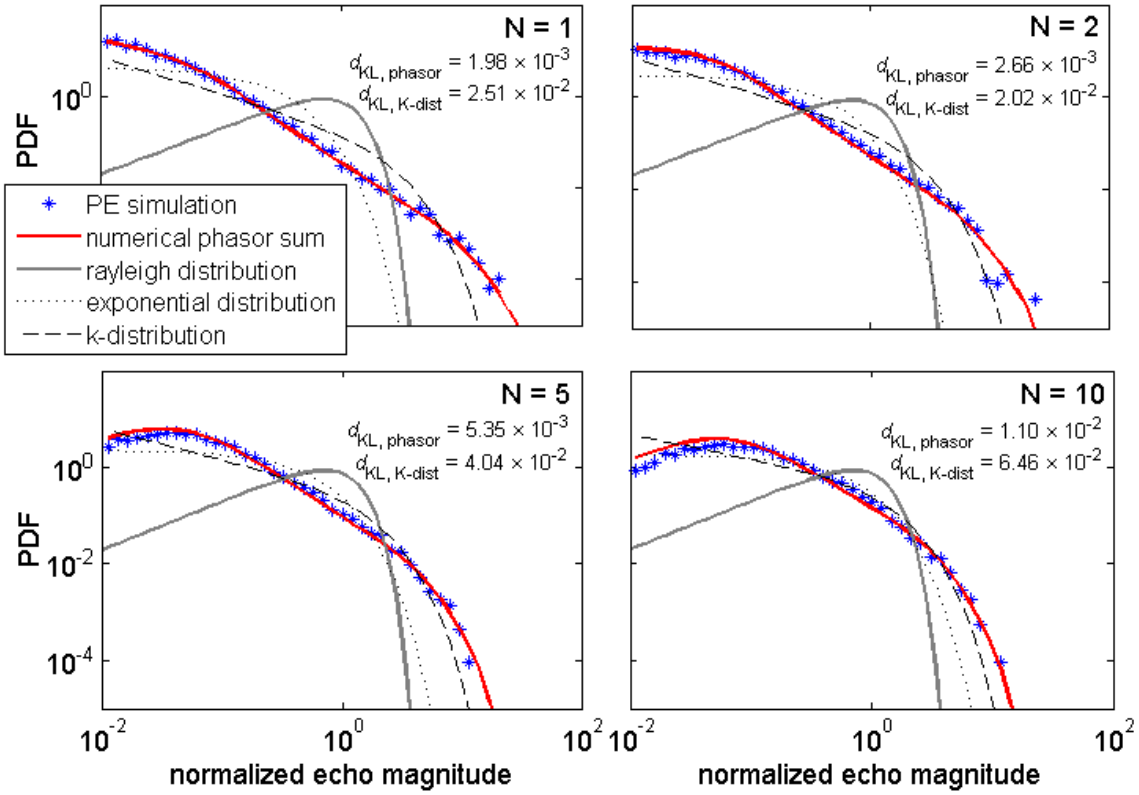

Figure 2.16 Predicted echo PDFs associated with a 3 kHz directional source at a depth of 10 m ensonifying various numbers of scatterers with *a constant scattering response*. The scatterers are located within the full 180° beampattern, azimuthally, and in a shallow thin layer vertically (10–20 m), at a range of 5250 m in a random oceanic waveguide. The directional source is a circular piston (ka=37.06) with a narrow beam (5° 3dB beamwidth). The number of scatterers, *N*, is given in the top right of each panel. Kullback-Leibler distances comparing PE predictions with phasor sum predictions, $d_{KL,phasor}$, and the K distribution, $d_{KL,K\text{-}dist}$, are given in the top-right corner of each panel.

.

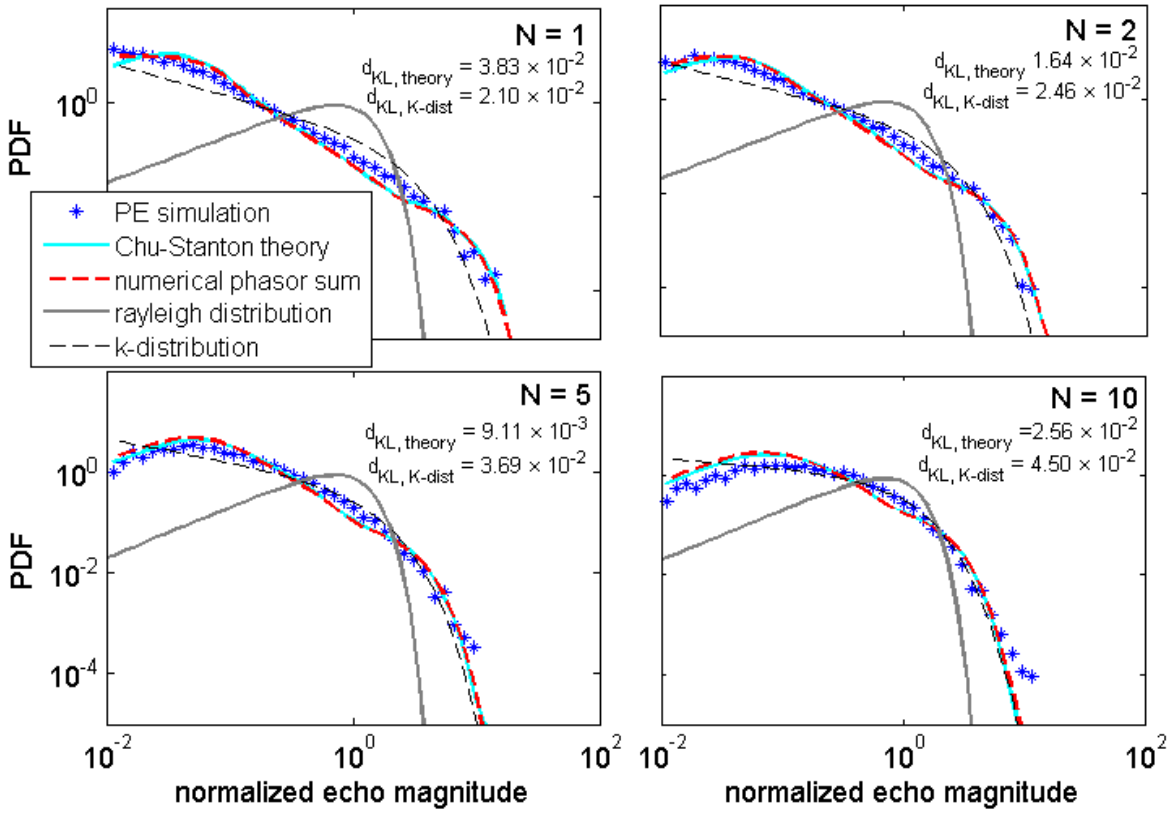

Figure 2.17 Predicted echo PDFs associated with a 3 kHz directional source at a depth of 10 m ensonifying various numbers of *extended scatterers* with a distribution of magnitudes of scattering responses that are *Rayleigh distributed*. The scatterers are located within the full 180° beampattern, azimuthally, and in a thin layer, vertically, at a range of 5250 m in a random oceanic waveguide. The directional source is a circular piston (ka=37.06) with a narrow beam (5° 3dB beamwidth). The number of scatterers, *N*, is given in the top right of each panel. Kullback-Leibler distances comparing PE predictions with Chu-Stanton theory, $d_{KL,theory}$, and the K distribution, $d_{KL,K-dist}$,are given in the top-right corner of each panel.

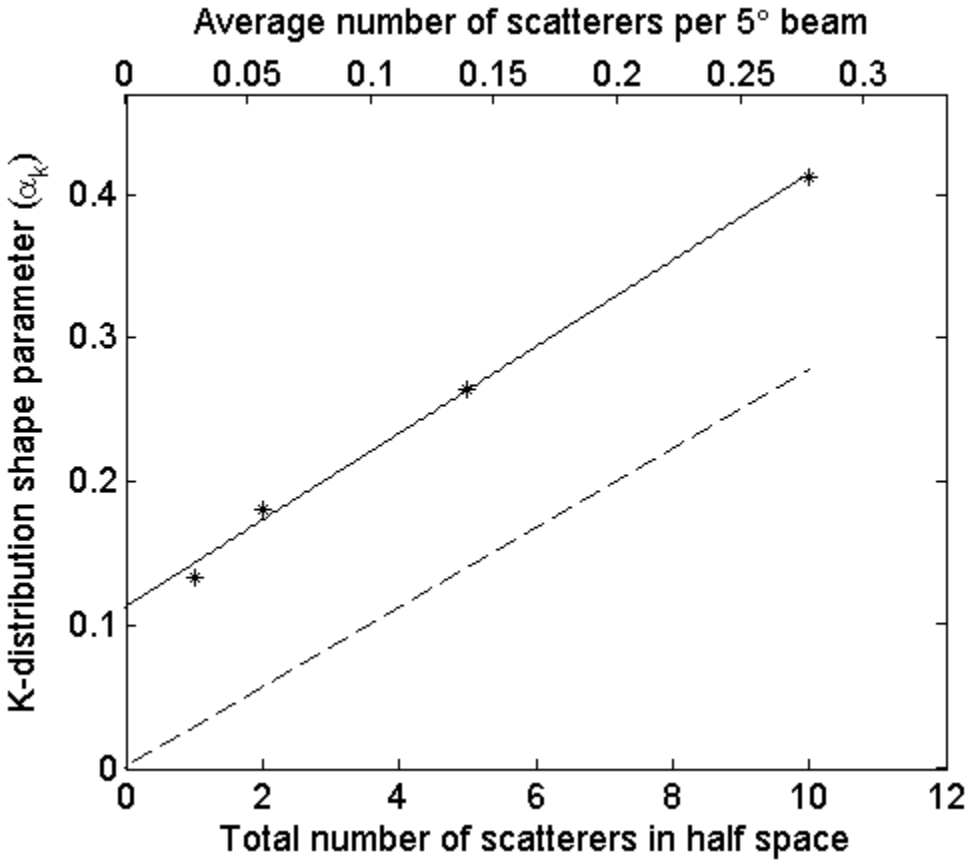

Figure 2.18 K distribution shape parameter, α_k, as a function of the number of scatterers ensonified by a directional beam in a shallow water oceanic waveguide. The model parameters are given in the caption of Figure 2.16. The black asterisks are the best fit shape parameter versus the number of scatterers located in the half-space. The solid line is a linear fit to the data. The dashed line is α_k equal to the average number of scatterers per main lobe (5° 3 dB beamwidth).

III. CLASSIFICATION AND STATISTICS OF LONG-RANGE, MID-FREQUENCY SONAR MEASUREMENTS OF AGGREGATIONS OF FISH

A. INTRODUCTION

Observations of fish from horizontally looking sonar systems have been documented since the late 1960s and early 1970s.[5–7] Since this time few studies have been conducted taking advantage of long-range horizontal propagation of acoustic energy to survey fish.[72–75] This is likely due to the myriad complications that arise with trying to localize and classify the source of scattering when using long-range horizontal-looking acoustic systems. Similar complications affect active military sonar systems when trying to discriminate between targets and non-targets. Furthermore, it is only recently that a concerted effort has been made to quantify the impacts of biologics on these systems.[27,28,44] In this study a unique set of measurements, of sparse compact scatterers by a broadband horizontally looking sonar system, is analyzed for key spectral and temporal features characteristic of aggregations of fish. The data are further analyzed to determine the key factors contributing to the highly non-Rayleigh distribution of echo magnitudes observed.

Sonar clutter in a military sonar system is defined as non-target echoes observed in processed data that generate false alarms.[2] One important characteristic of echoes that can contribute to false alarms is a temporal extent (i.e., the duration of the echo with sufficient amplitude to be seen above the background noise or reverberation) that is similar to that of a target. Since the temporal extent of the echo is related to the size of the scattering volume, an aggregation of scatterers that is similar in size to a target of interest is more likely to produce an echo of similar extent. A second characteristic contributing to false alarms is a non-Rayleigh distribution of echo envelopes (i.e., the magnitude of the complex pressure at the receiver). Specifically, a "heavy tailed" distribution, where the high amplitude portion of the distribution is elevated above a Rayleigh distribution, contributes to a higher probability of false alarm. There are several contributing factors which can lead to this type of non-Rayleigh distribution of echo envelopes. In a direct

path case it has been shown that the key factors are the number of scatterers in the beam, the source and receiver beampatterns, and the scattering response.[20] However, there are no studies to date examining the effects of these physical factors on the statistics of long-range echoes (i.e., ranges that are far when compared with the water depth) from scatterers in the water column of an oceanic waveguide.

Another application of this research is in fish surveys. Recent long-range surveys, using a narrowband acoustic system, have renewed interest in using horizontally looking systems to rapidly survey large volumes of water for fish.[74] However, complications arise when trying to interpret data involving long-range echoes particularly if the sources of the echoes are sparsely distributed. For example, the combination of a narrow beam and a refractive waveguide can lead to a highly non-uniform distribution of acoustic energy in the water column (e.g., see Sec. II.D.3) potentially leading to significant underestimates in the surveys. Also, since the depths of the fish are generally not known, it can be difficult to discriminate between bottom reverberation and scatterers in the water column. Fortunately, for gaseous swimbladder-bearing fish, the spectral characteristics of echoes from a broadband sonar system can help researchers classify these scatterers.[17,24] At the frequencies used in this study (1.5 to 9.5 kilohertz - kHz), swimbladdered fish, of a wide range of sizes, produce an acoustic response with a resonance peak[15,16] that can raise the fish echo above the background reverberation and help in classification of the echo's source.

In 2011, the second of two experiments was conducted in which long-range horizontal sonar measurements were made in the Gulf of Maine. This set of experiments is unique in that the acoustic measurements are broadband and are complemented with downward-looking multi-frequency measurements and fish trawls from a second vessel. Of interest to this study were measurements taken near Franklin Swell in which sparse, compact scatterers were observed in the long-range, horizontal sonar data. Fish trawls in this area sampled a mixture of species of swimbladder-bearing fish. Key results of the analysis presented here include the classification of sparsely distributed aggregations of swimbladder-bearing fish with echo levels at least 15 dB above the bottom-reverberation dominated background levels. Furthermore, these echoes are characterized by highly non-

Rayleigh echo magnitude statistics that are well modeled by a computationally efficient calculation that accounts for waveguide effects and beampatterns of the source and receiver (see Sec. II.C.3).

This chapter is organized as follows. Section B describes the 2011 Gulf of Maine experiment. Section C describes the models used in calculating reverberation from ocean boundaries and aggregations of fish in a waveguide. Section D describes the results which are divided into four sections (1) downward looking echo sounder data, (2) biologic sampling (fish trawls), (3) classification of the long-range echoes, and (4) statistics of the long-range echoes. Section E provides a discussion, conclusions and possible future work.

B. 2011 GULF OF MAINE EXPERIMENT

A collaborative experiment between Woods Hole Oceanographic Institution (WHOI), the Naval Research Laboratory (NRL), and the National Oceanic and Atmospheric Association's National Marine Fisheries Service (NOAA-NMFS) was conducted in September of 2011 to measure the spatial distribution and clutter characteristics of aggregations of fish in the Gulf of Maine. The experiment was conducted from two research vessels, the Fisheries Research Vessel (FRV) *Delaware II* (NMFS team) and the Research Vessel (RV) *Oceanus* (WHOI and NRL teams). The experiment was unique in that measurements were taken from long-range horizontal looking, broadband sonar system (NRL) which were complemented by narrowband, downward looking echo sounder measurements and net samples of fish (NMFS).

Of particular interest to this analysis are measurements of compact aggregations of fish from the horizontal-looking, long-range sonar near Franklin Swell (~42° north (N) latitude and 69° west (W) latitude). Data analyzed in this paper were derived from long-range (i.e., ~1 to 10 kilometers), acoustic measurements made on September 11, 2011, and short range acoustic measurements and biologic samples taken between September 9th and 15th, 2011, all in the Franklin Swell area (Figure 3.1).

1. Long-Range, Horizontally Looking Sonar System (NRL)

The NRL sonar system consists of a 10-element, broadband (1.5–9.5 kHz), vertical line array (VLA) source and a 32-element horizontal line array (HLA) receiver. The source VLA is towed from an A-frame aft of the vessel; while, the receiver HLA is deployed amidships and towed aft of the ship (Figure 3.2). Echoes from two linear frequency modulated (LFM) waveforms were analyzed in this study: LMN4U – a signal with a bandwidth, *W*, of 700 hertz (Hz) centered at 3750 Hz, and LM4U – a 3.5 kHz bandwidth signal centered at 3250 Hz (Table 3.1). These waveforms were transmitted in sequence with two other signals with a 20 second delay between each transmission giving a total cycle time between transmissions of a given waveform of 80 seconds. Echoes analyzed in this analysis come from four data sets (Sets C, C2, D, and E) from one period between 15:27 and 19:50 local time on September 11, 2011 in the vicinity of Franklin Swell (Figure 3.1). During this period the source depth was centered at 48 meters (m) and the average receiver depth was 38 m. Data were processed using matched filtering and, in the case of identifying echoes of interest, a normalization method called a *split-window normalizer.*[2] This technique implements a sliding window in which a sample (at the center of the window) is normalized by the mean envelope in a pair of windows separated (or *split*) by a small window centered on the sample that is excluded from the mean normalization value (Figure 3.3).

2. Downward-Looking Narrowband Echo Sounder (NOAA-NMFS)

A hull-mounted, downward-looking Simrad EK60 scientific echo sounder collected multi-frequency (18 kHz, 38 kHz, 120 kHz) acoustic data nearly continuously aboard FRV *Delaware II*. These echo sounder data were processed by the NMFS team using a combination of manual analysis and automated classification and detection algorithms to identify gas-filled-swimbladder bearing fish schools, classify aggregations of swimbladder bearing fish into Atlantic herring (*Clupea harengus*) and non-herring schools, and extract parameters for each school (e.g., school depth, school length, school thickness, and volume scattering strength).[76]

3. Biological Sampling (NOAA-NMFS)

Trawls were conducted from the FRV *Delaware II* using a polytron mid-water rope trawl with a mouth opening of 35 m, horizontally, and 15 m vertically. The trawl was deployed at times, depths, and durations based on real time echo sounder data indicating the presence of fish. Typical tow rates were 3–4 knots (kn). Twelve trawls were conducted between the 11th and 15th of September 2011, within 25 kilometers (km) of the RV *Oceanus* ship track of 11 September 2011 (Figure 3.4). Trawls depths were not recorded on the "minilog" temperature-depth recorder for one trawl, so only eleven trawl samples were used in this analysis neglecting the trawl with missing depth information. A manual survey was conducted of each haul identifying the number, species, and fork length, L, of fish caught. In addition, the deployment times, tow duration, depths, and geographic locations of the start and end of each tow were recorded for each trawl deployment.

4. Water Column Sampling (NOAA-NMFS)

Vertical profiles using conductivity, temperature and depth sensors (CTD) were conducted from the RV *Delaware II* using a Seabird Electronics (SBE) model 19*plus* profiling CTD. In order to characterize the environment for acoustic propagation modeling, all CTD measurements made between the 11th and 15th of September between times of 12:00 and 23:59 local and within approximately 25 NM of the RV *Oceanus* ship track of September 11th, 2011, (Figure 3.5) were considered in this analysis (15 total). Measurements were made over a range of depths from the surface to a maximum depth of 227 m (Figure 3.6).

C. REVERBERATION MODELS

Two range-dependent reverberation models were used in this study: 1) the Sonar Simulation Toolset[76,77] (SST) to calculate boundary reverberation (i.e., bottom and surface backscatter) and 2) a two-way parabolic equation (PE) model used to calculate volume reverberation from aggregations of fish. The two-way PE formulation used in this study, a modified two-way version of the range-dependent acoustic model (RAM)[58] that does not calculate backscatter from the boundaries, has the capability of incorporating

range-dependent sound-speed profiles. The SST program, in contrast, efficiently calculates boundary reverberation using a ray-based approach, but is limited, at the time of this research, to range-*independent* sound-speed profiles.

1. Sonar Simulation Toolset

The Sonar Simulation Toolset (SST) is a comprehensive simulator for active sonar systems allowing user defined beampatterns, waveforms, and propagation environment.[77,78] SST uses the Comprehensive Acoustic System Simulation (CASS) with the Gaussian Ray Bundle (GRAB) as the primary acoustic propagation model. CASS-GRAB is a ray-based propagation model that is capable of both depth- and range-dependent environments. CASS-GRAB differs from the classical ray-based approach in that the amplitude of each eigenray is derived from test rays which have amplitudes that are Gaussian distributed in depth.[79] This modification increases accuracy of pressure-field predictions near caustics in a refractive environment. Implementation of CASS-GRAB in SST, although capable of handling some range-dependent properties (e.g., bathymetry), is limited to range-independent sound-speed environments and, therefore, could not incorporate fluctuations due to internal waves. In this study SST is used to predict reverberation by ocean boundaries (i.e., surface and bottom) when ensonified by a horizontal-looking, active sonar system.

2. Two-Way Parabolic Equation Model

Calculating the volume reverberation from an aggregation of scatterers in a shallow-water environment requires accounting for both the forward- and back-propagated acoustic fields as influenced by waveguide effects as well as the scattering response of the reverberation volume. The approach taken here is to connect a shallow-water acoustic propagation model (described in detail in Sec II.C.1–2) with a free-field scattering model for aggregations of fish (see Appendix E).

In general, an aggregation of fish is represented by a collection of scattering centers (isotropic scatterers that are treated as monopole sources in the back-propagation calculation). The complex pressure at each scattering center is defined for each discrete frequency, f, as

$$s(\mathbf{r}_j;\mathrm{f}) = g_j(\mathbf{r}_{\mathrm{src}} \mid \mathbf{r}_j;\mathrm{f}) \left| f_{\mathrm{bs}}^{\mathrm{eff}}(\mathrm{f}) \right|_j , \tag{3.1}$$

where $g_j(\mathbf{r}_{\mathrm{src}} \mid \mathbf{r}_j;\mathrm{f})$ is the Green's function associated with the pressure field propagated from the source location, $\mathbf{r}_{\mathrm{src}}$, to the location of the *j*th scattering center, $\mathbf{r}_j$, and $\left| f_{\mathrm{bs}}^{\mathrm{eff}}(\mathrm{f}) \right|_j$ is the effective backscattering amplitude associated with the *j*th scattering center, (see Appendix E, Eq. (E.7)). The total volume reverberation level at the receiver is then calculated from the coherent summation of contributions from N_{s} scattering centers

$$RL_V = 10\log\left(\left| \sum_{j=1}^{N_{\mathrm{s}}} g_j(\mathbf{r}_j \mid \mathbf{r}_{\mathrm{rcv}};\mathrm{f}) g_j(\mathbf{r}_{\mathrm{src}} \mid \mathbf{r}_j;\mathrm{f}) \left| f_{\mathrm{bs}}^{\mathrm{eff}}(\mathrm{f}) \right|_j \right|^2 \right), \tag{3.2}$$

where $g_j(\mathbf{r}_j \mid \mathbf{r}_{\mathrm{rcv}};\mathrm{f})$ is the Green's function associated with the propagation of the scattered field from the jth scattering center to the location of the receiver, $\mathbf{r}_{\mathrm{rcv}}$.

D. RESULTS

In this analysis a subset of the NRL long-range acoustic data, characterized by compact and spatially sparse scatterers, was examined. These data sets (C, C2, D, and E) are identified by a range of beams and transmission times (Table 3.2). In order to classify the source of the echoes, as fish aggregations or non-fish scatterers, several cotemporaneous acoustic and non-acoustic data sets were also analyzed. In order to ensure correlation between the short-range, downward-looking acoustic data, biologic samples, and water column samples with the long-range acoustic data, only data collected between 11–15 September 2011, within 25 km of the *Oceanus* track of September 11, 2011, were considered in this study. Also, most of the long-range acoustic data were collected after sunset which occurred at 18:53 local in this region. Therefore, only trawl samples and downward-looking echosounder data collected at night are used in the classification of echoes.

1. Characteristics of Fish Schools Derived from Downward-Looking Echo-Sounder Measurements

Data from the downward-looking echosounder on FRV *Delaware II* were analyzed by the NMFS team to derive a variety of parameters pertaining to aggregations of fish in the vicinity of Franklin Swell. These parameters include mean depths, lengths, thicknesses and mean volume scattering strengths, S_V, of each fish school. The data are divided into Atlantic herring and non-herring observations. Normalized histograms of the depths, lengths, and thicknesses are illustrated for both day and night observations (Figure 3.7 and Figure 3.8). While the depth distribution of Atlantic herring during the day is narrowly distributed around 170 m, they are broadly distributed at night with a multi-modal distribution. However, given the low sample number it is difficult to draw any conclusions about the depth distribution from this data. The school length and school thickness distributions of Atlantic herring at night are more narrowly distributed (median length 39.0 m, median thickness: 5.7 m) and are similar to the day distributions (median length: 80.3 m, median thickness: 4.8 m) and night. Non-herring distributions of length and thickness during the day are virtually the same as herring; although, they are observed primarily at shallower depths (median depth: 28.9m). Non-herring distributions of lengths are greater than herring at night (median length: 124.0 m) while the thickness are nearly the same (median thickness: 5.4 m).

An important parameter for acoustic modeling of aggregations of scatterers is the numerical density of the scatterers, ρ_S. Observed volume scattering strengths, S_V, for the schools were used to derive fish school densities (i.e., number of fish per cubic meter). Following the methodology by Ona[80] a regression formula dependent upon depth in m, *z*, is used to calculate target strength, averaged over *in situ* tilt distribution, of Atlantic herring according to total fish length (m), L_{tot},

$$\text{TS} = 20\log_{10}(100L_{tot}) - 2.3\log_{10}(1+z/10) - 65.4\,. \qquad (3.3)$$

The fork length (m), L, and total length, L_{tot}, of Atlantic herring are related[81] by $L_{\text{tot}} = 1\times10^{-4} + 1.103L$. The average differential backscattering cross section can then be calculated as

$$\bar{\sigma}_{bs} = \left\langle 10^{\mathrm{TS}/10} \right\rangle, \tag{3.4}$$

where the brackets represent an average over the observed length distribution. In this case, the length distribution comes from combined trawl hauls over all depths sampled. Fish school density is then calculated from Eq. (F.2) as

$$\rho_{\mathrm{S}} = \frac{10^{S_V/10}}{\bar{\sigma}_{\mathrm{bs}}}. \tag{3.5}$$

Densities were calculated for observed fish schools comprised of Atlantic herring and are shown for both day and night observations (Figure 3.9).

2. Biologic Sampling

Trawls were conducted on an ad-hoc basis from the FRV *Delaware II* in order to sample fish when they were observed acoustically on the downward looking echo sounder. Of the eleven trawls used in this analysis, four were conducted during the day and seven were conducted at night (Figure 3.4). Three species, Atlantic herring (*clupeak harengus*), silver hake (*Merluccius bilinearis*) and Acadian redfish (*Sebastes fasciatus*) comprised most of the trawl catches. Herring and hake were caught at all depths sampled (100–205 m) during both day and night trawls with small hake caught in the highest abundance (Figure 3.10, Figure 3.11). Redfish were only caught in significant quantities at deep depths (170–205 m) at night (Figure 3.11). The fork lengths of silver hake and Atlantic herring were narrowly distributed about 4 and 21 centimeter (cm), respectively; at all depths sampled (100–205 m); while, Acadian redfish had a broad distribution of lengths between 18 and 35 cm and a small percentage of fish sampled with lengths below 10 cm (Figure 3.10, Figure 3.11).

Importantly, it is not expected that the relative catch densities of various species correspond to relative in situ aggregation densities. Unknown factors, associated with converting catch density to aggregation density (e.g., geometry of the intersection between the trawl tow and the fish aggregations, and avoidance rates for various species) are too significant to glean any information other than presence or absence of fish at various depths.

3. Classification of Broadband, Long-Range Echoes

The goal of this portion of the analysis is to characterize, both spectrally and temporally, the long-range echoes to determine if they are likely from fish aggregations or not. Data associated with two signals are analyzed in this section (Table 3.1): data associated with the 3.5 kHz bandwidth waveform, LM4U, are analyzed for spectral clues characteristic of resonant swimbladder-bearing fish, and data associated with the 700 Hz bandwidth waveform, LMN4U, are analyzed temporally to determine if echoes have amplitudes and temporal extents resembling those predicted from aggregations of fish.

a. Spectral Analysis

Echoes from the broadband waveform LM4U were analyzed by the NRL team for spectral content. Four sets of data were formed from contiguous regions of high echo density (Table 3.2). The regions, defined by a narrow range of receiver beams and transmission times, produce sets of echoes that are locally assumed to be both spatially and temporally stationary. Additionally two-way travel time was limited to 2 to 9 seconds (approximately 1.5 to 6.5 km one-way range to scatterers).

Data were first matched filtered and normalized using a split-window normalizer[2] with a guard band of $2/W = 5.71\times10^{-4}$ second (s), where W is the transmit waveform bandwidth, and an auxiliary band of 5.41×10^{-1} s, corresponding to 200-meter range bin. Then, time bins were identified by centering a 5.41×10^{-1} s window (~ 200 m) around normalized echoes that were at least 15 decibels (dB) above the background levels, within the given beam, transmission time, and two-way travel time limits. Mean spectra were then formed for each data set by taking the Fourier transform of the matched-filtered (non-normalized) data corresponding to those time bins, averaging over all echoes, and correcting for frequency-dependent water column attenuation and source level (Figure 3.12).

Calculations of resonance scattering responses were made using a scattering model for mixed assemblages of fish that was used in a study in the same geographic region and the same frequencies as this experiment.[17] A variety of published and empirical parameters relating to the fish were used in this model. The parameters

directly related to the resonant swimbladder model (see Appendix F, Eqs. (F.3)–(F.9)) are given in Table 3.3. The coefficient for the regression of the swimbladder volume to the fish length, *A*, and the viscosity of fish flesh, ξ, used here are published parameters for the same species in all cases except for the Acadian redfish larger than 12 cm. There are no published parameters available for large Acadian redfish, a physoclistous species. Therefore, ξ for silver hake, also a physoclist, was used in these predictions. The frequency of the resonance peak is highly sensitive to the regression coefficient, *A*; therefore, some comparisons were made to verify reasonable assumptions of this value for redfish. It is known that Acadian redfish are larger bodied than silver hake; and, data from NOAA-NMFS[82] show that, in a comparison of 20 cm long Acadian redfish and silver hake, the ratio of their masses is approximately 2.4. For a state of neutral buoyancy it is assumed that the volume of the swimbladder, and thereby *A* by Eq. (F.4), is directly proportional to the mass of the fish. Multiplying *A* for large silver hake by this factor gives an estimated *A* for redfish of 6×10^{-5}. Fitting the model to the data resulted in a value of *A* for redfish of 1×10^{-4}, in reasonable agreement with these calculations.

Empirical parameters used include the length distribution and depth of the fish. The frequency-dependent differential backscattering cross-section, σ_{bs}, for each species is calculated using Eq. (F.3) in Appendix F for the range of observed lengths of fish and then weighted by the length distribution observed in night trawl hauls for that species to produce an average cross-section. The depth of the fish used was the midpoint of depths where that species was observed in night trawl hauls in significant quantities.

Finally, $\bar{\sigma}_{bs}$ is weighted by a relative numeric density of each species (Table 3.4) by a best fit to the data (Figure 3.12). The result is a good fit with the observed spectra. The maximum relative density contribution comes from Atlantic herring in three of the four cases (C2, D, and E). The predicted resonant scattering by these fish produce the spectral peak near 3 kHz which is seen in these three data sets. The predicted spectral peak near 1.5 kHz is resonance scattering by larger Acadian redfish. Two data sets (C and C2) appear to show a rise with decreasing frequency below 2 kHz that agree with the redfish resonance prediction. Finally, although the resonance peak for

the much smaller silver hake occurs above 5 kHz and is therefore not seen in the data, the inclusion of this species in the model reduces the magnitude of the slope above 3.5 kHz producing a better fit with the data.

b. Temporal Analysis

A second analysis was conducted to compare model predictions of reverberation by compact aggregations of resonant swimbladder-bearing fish in a waveguide with long-range sonar measurements. The data set examined was characterized by sparsely distributed high-amplitude echoes and a strong spectral peak suggesting resonance scattering from Atlantic herring (set D, Figure 3.12). In this analysis reverberation from transmissions of the narrower bandwidth signal LMN4U is examined. This narrower bandwidth waveform more closely approximates the waveforms used in military sonar applications. The goal of this analysis was to determine if fish schools of the observed species, fish length, school size, and aggregation density could produce echoes strong enough to be observed above the background reverberation and appear, at least qualitatively, similar to those observed in the long-range sonar data.

In order to make predictions to compare with data, a hybrid approach was taken in which two model calculations are combined coherently. The background reverberation is modeled using the ray-based SST program; while, calculations of volume reverberation by an aggregation of fish are made using the two-way PE model. This hybrid approach allowed for an efficient calculation of the background reverberation while making accurate predictions of scattering by schools of fish. To ease the computational burden, since processing time for the harmonic PE model is directly proportional to bandwidth, model calculations were made using a 100 Hz bandwidth signal with the same center frequency (3750 Hz) as the 700 Hz bandwidth waveform, LMN4U. Both the ray-based and PE calculations were made at the same bandwidth.

Ray-based predictions of non-fish reverberation are based upon the NRL system configuration, observed depth-dependent water column properties, range-dependent bathymetry,[83] and published bottom properties[84] (Table 3.5). The water column properties used were the mean profiles from averaged afternoon-to-evening

(12:00 – 23:59 local) profiles. Averaged reverberation levels over the mean forward beams (beams 5–15) and mean aft beams (20–30) for eight transmissions of LMN4U waveform between 18:42:54 and 18:52:14 local were compared with 100 Hz bandwidth model predictions (Figure 3.13) giving reasonable results. The first two peaks, observed prior to 1 s are the initial surface and bottom reflections. The peak observed near 2 s is the next bottom bounce. In all three of these cases the peak is significantly broader in the prediction than the data. This is due the effect of match-filtering the data which results in a time resolution of the received signal of $1/W$.

In the PE calculation an aggregation of 21 cm Atlantic Herring was simulated using parameters for fish school length, thickness, and density that were within the range of observed schools (Table 3.6). This species was dominant in the trawl hauls (Figure 3.11) at sizes that are shown to be resonant near the center frequency of the waveform analyzed. In order to simulate a realistic fish school, a representative morphology of a school of Atlantic herring, measured by 400 kHz multi-beam echosounder[19] near the experimental site in September of 2006, was scaled to similar dimensions of an observed fish school (Table 2.1). The majority of echoes analyzed in the spectral analysis of data set D had a two-way travel time corresponding to ranges of scatterers of approximately 2.2 to 3.7 km and all were located between beams 20 and 30 of the receiver array. In order to conduct a comparison between these observations and model predictions for a fish school positioned at a range of distances from the source to the scatterer, several simulations were conducted with a single fish school randomly positioned within a 100 m range bin for bins centered on 100 m range steps from 2050 to 4450 m from the source. Azimuthally, the scatterers were randomly positioned between angles corresponding to beams 20 and 30 of the receiver array (see Table 3.6 for all key modeling parameters).

The environmental parameters in the PE calculation included bathymetry measurements that were identical to those used in the ray-based calculations. Bottom type parameters were derived from the same database as used in the ray-based calculations, but were interpolated to give range-dependent bottom properties. The mean sound-speed profile was also identical between the models; however, the PE calculation uses a

shallow-water internal wave simulation to induce range-dependent sound-speed profile perturbations.[65] Water column profiles used in the internal wave modeling are given in Figure 3.14. Transmission loss calculations for four internal wave field simulations illustrate both the position (i.e., range and depth) -dependent and realization-dependent variability of the incident pressure field (Figure 3.15).

The PE- and ray-based calculations were coherently summed, beam-formed and match-filtered for comparison with observations. Comparisons are made between both the split-window normalized and non-normalized data. While few echoes were visible in the non-normalized data (both observed and predicted), predicted echoes of 14 of 25 aggregations could be seen above the background reverberation and were qualitatively similar in temporal extent and amplitude to the normalized and matched-filtered observed data (e.g., see Figure 3.16).

4. Echo Statistics

In this section of the analysis, echoes are examined from three sets of long-range, horizontally looking sonar data (C2, D, E – Table 3.2) and compared with theory and simulations. Broadband echoes from these beam-time regions are shown to have a spectral peak near 3 kHz (Figure 3.12) suggestive of echoes dominated by Atlantic herring near this frequency. The echoes analyzed in this section correspond with transmissions of the LMN4U signal, a 700 Hz bandwidth, linear frequency modulated (LFM) waveform centered at 3750 Hz.

a. Data Analysis Methods

Normalized echoes, with levels 15 dB above the background, were identified in order to define time windows for extracting non-normalized echoes for analysis in the same manner as described in Sec. III.D.3.a. In this case the split-window normalizer had a guard band of 2.90×10^{-3} s, corresponding to $2/W$, and an auxiliary band of 5.41×10^{-1} s, corresponding to 200-meter range bin. Ensembles were then formed from *non-normalized* echoes in a given bin (based on two-way travel time) where the ensemble is of echo envelopes, sampled across the extent of the echo.

A primary concern when calculating statistics of the echoes is that the ensemble is formed from independent samples with a stationary mean. The primary assumption used here is that the environment is locally stationary (i.e., the statistics are stationary over the short period of time and a narrow region in space considered). Echoes analyzed are limited to those arising from sonar transmissions covering a period of approximately 73 minutes, a period over which it is assumed that the mean characteristics of the ocean (e.g., the mean sound speed profile) are constant. Furthermore, the echoes are grouped into 0.67 s bins, a period of two-way travel time corresponding to approximately 500 m of spatial extent. Due to the narrow time bin and the high selection threshold of 15 dB, which likely limits the echoes to those associated with scatterers in the energetic portion of the waveguide (i.e., not including the shadow zones), the transmission losses for the echoes are assumed constant across echoes within a given time bin.

Echoes are assumed to be independent from ping to ping based on the 80 second cycle time between transmissions. In order to ensure that samples from within a given echo were non-overlapping, the matched-filtered echo envelopes were sub-sampled at a spacing of 1.5×10^{-3} s, greater than the time resolution of the waveform (1.4×10^{-3} s). To determine if this sample spacing was sufficient to ensure independence of samples within an echo, the e-folding correlation time, τ_e , was calculated as $\langle R_{xx}(\tau_e)\rangle = R_0 / e$, where R_{xx} is the autocorrelation function for each echo, R_0 is the maximum value at a delay time, $\tau = 0$, and the mean is over all echoes in a given time bin. The resulting e-folding times for all bins, $\tau_e < 1.31\times10^{-3}$, which is less than the sample spacing, ensures no correlation between samples.

b. Model Comparisons

Probability density functions (PDFs) of echo envelopes are compared, using methods described in Appendix D, with theoretical predictions following the Chu-Stanton theory.[29] This theory, developed for direct path scattering by point scatterers, has been applied to extended scatterers at long ranges in shallow water by accounting for

waveguide effects. These effects include the truncation of the vertical beampattern to account for attenuation of high angle energy and the squaring of the one-way response due to reciprocity of forward and back-propagated acoustic paths (see Sec.II.D.4). Extended scatterers in this context implies that the scattering volume, in this case an aggregation of fish, is large compared with the distance at which the incident pressure field becomes uncorrelated due to multipath interference. Three effects are examined in this section: (1) range-dependence of the echo envelope PDFs, (2) effects of a directional beampattern, and (3) effects of the split-window normalizer on the echo statistics.

Theoretical predictions of PDFs are calculated using the phasor summation method, Eq. (2.19), calculated at the center frequency of the transmitted waveform, 3750 Hz. Calculations in this section use zero-mean complex Gaussian probability density function (PDF) of scatterer amplitudes, p_A, corresponding to a magnitude of the scattering response that is Rayleigh distributed. The elevation beampattern is calculated from a shaded beampattern where the shading is derived from the mean observed power applied to the 10-element vertical line array (VLA) over the range of frequencies in the waveform (Figure 3.17). The elevation angle, ϕ, is limited in extent to account for waveguide effects (see Sec. II.G.2) where the exact values were fit to the data. The azimuthal beampattern is derived from a theoretical beampattern for a 32-element, hamming-weighted horizontal line array (HLA) for the beam at the midpoint of the range of beams defining the given data set (i.e., beam 27 for set C2 and beam 25 for sets D and E). The azimuthal angle was also limited to fit to the data. This modification is to account for the effect of choosing echoes with a high SNR as these echoes are most likely to be located within the main lobe of the acoustic beam. Finally, complex-Gaussian-distributed noise was added to the phasor summation result to account for interfering noise (both system and ambient) and non-fish reverberation in the observed data. The resultant signal, then, is $\hat{s}_1 = \hat{s} + \hat{n}$, where $\hat{s}$ is the complex pressure summed over *N* scatterers, from Eq. (2.19), and $\hat{n}$ is the additive noise. The level of the noise was fit to the low amplitude portion of the PDFs in all cases.

c. Range-Dependent Statistics

In order to determine if the echo envelope distributions have a range-dependence, echoes from sets C2, D, and E (Table 3.2) are grouped into range bins based on two-way-travel time of 0.67 s (~ 500 m range bins) from 3.1 to 17.0 s (~ 1.5 to 11.9 km). Bins with 15 or more echoes were considered for analysis. Finally, PDFs were generated from histograms of the echo envelopes normalized by the root mean square (rms) echo amplitude of the ensemble (Figure 3.18).

For comparison phasor summation calculations were made at the center frequency 3750 Hz with the number of scatterers, $N = 1$. In this calculation the azimuthal beam angle, θ, is limited to $\pm\theta_{\mathrm{SL}}$, where θ_{SL} is the angle at which the level of the main lobe decreases to the level of the highest side lobe (Figure 3.17, top panel). The elevation angle, ϕ, is limited to the main lobe and first side lobe (Figure 3.17, bottom panel). These parameters were kept constant for all ranges. Noise was added to the phasor summation and this parameter varied for each range.

Of the 23 range bins, 10 bins contained more than 15 echoes with an SNR of 15 dB or more, with no range bins beyond 8 km meeting this threshold. The echo envelope PDFs show very little range dependence over the ranges observed. The most significant difference with range is observed in the low amplitude portion of the PDF. The phasor summation predictions were in excellent agreement with the data outperforming the K distribution at all ranges (see Kullback-Leibler distances, d_{KL}, given in Figure 3.18), and providing an order of magnitude or more improvement at several ranges. It should be noted, though, that the K distribution performs similarly well in the very high amplitude "tail" of the PDF. The most notable improvement over the K distribution is in accounting for the inflection point in the data seen in nearly all the observed PDFs.

d. Beampattern Effects

The favorable comparison between the distributions of echo envelopes observed in the long-range data and the phasor summation calculation, in particular the

well-modeled inflection point in the PDFs, suggest that the observed PDFs are strongly influenced by the main lobe of the source and receiver beam patterns (Figure 3.18). However, there is another factor that can produce a qualitatively similar inflection point in an echo envelope PDF associated with an ensonified aggregation of scatterers. A study of echo statistics from an aggregation of fish in a direct path geometry illustrates this effect by showing the influence of system noise on the echo statistics.[20] In this study a two-component mixture PDF is compared with observed data, where one component is the distribution of the background noise and the second component is the distribution of echo envelopes from aggregations of unresolved fish. Such a mixture produces a PDF with an inflection point between the low-amplitude portion dominated by the background noise and the high-amplitude portion dominated by the fish echoes. In order to eliminate this mixture of echo and system noise or Rayleigh-distributed background reverberation as the primary contributor to the non-Rayleigh envelope distribution observed in this study, various two-component Rayleigh mixture PDFs are compared with an observed echo-envelope distribution. These mixture distributions, which do not account for beam pattern effects, are further compared with a phasor summation calculation which explicitly accounts for the effects of a non-uniform (i.e., directional) acoustic beam.

A single range bin was chosen ($4018.2\ \text{m} \lesssim r \lesssim 5018.2\ \text{m}$) in order to illustrate the relative importance of the beam pattern contribution over background noise or reverberation. In the mixture PDF calculations, ensembles of signal envelopes were generated in which the sample window contains part high amplitude echo (with a complex-Gaussian pressure distribution) with additive complex-Gaussian noise and part only complex-Gaussian noise (i.e., a mixture of two zero-mean, complex Gaussian distributions with different variances). In this mixture calculation a *x*% mixture contains a total of N_{tot} samples, where $N_1 = (1-x)N_{\text{tot}}$ samples are from a distribution with variance, $\sigma_1^2 + \sigma_2^2$, and $N_2 = xN_{\text{tot}}$ samples are from a distribution with variance, σ_2^2, where $\sigma_1^2 > \sigma_2^2$. Comparisons are made where $\sigma_1^2 = 1$ and σ_2^2 is used as a fitting parameter to the low amplitude portion of the observed PDF. Several mixture combinations are calculated ranging from a 5% to a 50% mixture. In none of the cases

considered does the mixture calculation agree well with the observed PDF (Figure 3.19). The best fit was the 50% mixture ($d_{\mathrm{KL}} = 1.10 \times 10^{-2}$); whereas, the phasor summation (see Sec. III.D.4.b), which accounts for beam pattern effects, matches the data closely ($d_{\mathrm{KL}} = 3.80 \times 10^{-3}$).

E. DISCUSSION

1. Echo Classification

Echoes from long-range, horizontal-looking measurements by a mid-frequency, broadband sonar system have characteristics, both temporally and spectrally, consistent with the presence of aggregations of fish. A scattering model for mixed assemblages of fish shows that the spectral content of the echoes can be reasonably represented by the resonant scattering of the three dominant species sampled in trawls during the experiment. Most key parameters used in the resonant swimbladder model are either published or observed values, while parameters that were unknown (i.e., those describing the swimbladder of large Acadian redfish) were fit to the data using reasonable values given known characteristics of these fish.

One key parameter that is generally unknown in horizontal-looking sonar data is the depth of scatterers. The depths used in the scattering model were the midpoints of the depths where each species was sampled (Table 3.3). The effect of this assumption is that the mixed assemblage scattering model predicts a narrower resonance peak than if the scattering response was calculated for fish distributed over a range of depths (Figure 3.12). There are, at least, two possible reasons why the data validate this assumption. The first possibility is that the fish ensonified in the analyzed data sets were distributed narrowly near the assumed depth and that the trawl samples, widely distributed over time and space, do not provide a good estimate of the distribution of fish for a narrow region in time and space. A second possibility is that the fish are more broadly distributed in depth, but echoes from fish located near the assumed depth dominate the mean spectra. This second explanation is reasonable because the echoes used in the spectral analysis are not corrected for transmission loss, an unknown quantity given the unknown depth of the scatterers. Without normalizing for variation in transmission losses associated with

scatterers located in different parts of the waveguide, the mean spectra are likely dominated by high amplitude echoes that arise when the fish are located at short ranges and in an energetic portion of the waveguide. These energetic regions can have a narrow extent in depth (e.g., the region centered at a range of 2 km and a depth of 150 m – see Figure 3.15) which would give echoes associated with scatterers at these depths a stronger weighting in the mean spectra.

The final unknown parameter in the spectral modeling was the relative numeric density contribution of each species. While the trawl data provide some information on the dominant species present, no information regarding the relative masses of the species can be gleaned from this data for several reasons: 1) the trawls were conducted on an ad hoc basis rather than following a systematic survey plan, 2) the geometry describing the intersection between the trawl sample volume and the fish aggregations is unknown, and 3) the various species and sizes of fish sampled likely have different avoidance rates for the trawl. So, the relative density of each species was fit to the data. Still, the resultant parameters, with silver hake and Atlantic herring dominating most of the data sets (Table 3.4), agree broadly with trawl data (Figure 3.10 and Figure 3.11).

Reverberation modeling of fish schools, using conservative values for school size and school density (Table 3.6), predict that aggregations of 21 cm Herring at 155 m depth can be observed above the background reverberation in a majority of the simulations at various ranges and azimuthal angles. The ranges modeled were approximately 2 to 4.5 km which corresponding to the ranges in data set D where high amplitude, compact echoes were observed. Due to computational limitations modeling was conducted using a 100 Hz bandwidth signal in contrast to the 700 Hz bandwidth waveform used in the experiment. The likely impact of the lower bandwidth simulations is to under predict the ratios of the echo levels to the background levels as the lower time-bandwidth product is directly related to a lower matched filter gain.

2. Echo Statistics

Echoes, presumably from compact aggregations of fish, are shown to produce highly non-Rayleigh echo envelope PDFs. Moreover, for the ranges observed in three data sets, the distributions of echo envelopes were nearly invariant in range. While the high amplitude "tail" of the PDFs showed little dependency on range, the low amplitude portion, characterized by the background reverberation and noise, did vary some with range. The stability of the statistics with range is most likely due to a combination of factors. First, the sparse spatial distribution of scatterers ensures that the number of aggregations in a given sonar resolution cell is no more than one; and, second the pressure field is likely saturated by natural randomness in the waveguide. These two factors result in a nearly constant distribution of normalized echo envelopes with range. Interestingly, the waveguide-influenced beampattern effects also remain constant, at least over the ranges analyzed. It is expected that the invariance of the statistics with range would not apply at short ranges and in regions where the fish aggregations are more densely distributed. At short ranges the statistics of the pressure field may vary widely before reaching saturation (e.g., see Figure 2.14). For more dense distributions of fish schools, the number of aggregations per sonar resolution cell is likely to vary with increasing sonar sample volume which increases as the square of the range. While both of these effects could add range dependencies to the echo statistics, the latter effect could be explicitly accounted for in the phasor summation model by making N a function of range given a known spatial distribution of fish aggregations.

It is also shown that a physics-based model accounting for (1) the number of schools in the sonar beam (for a given range cell), (2) the stochastic scattering response of the fish aggregation (i.e., a complex-Gaussian scattering response), (3) the beampatterns (both source and receiver) of the active sonar system, and (4) background noise and/or reverberation can accurately predict the distribution of echo envelopes. Finally, the K distribution, a frequently used distribution to model non-Rayleigh echoes, can be well fit to the high amplitude portion of the PDFs. However, this distribution inherently does not account for beampattern effects and, therefore, does not predict the inflection in the PDFs caused by the inclusion of the main lobe of the sonar beam.

F. CONCLUSION

This research has potential application to two widely disparate communities – fisheries researchers and military sonar operators. For fisheries research this study emphasizes several benefits as well as potential pitfalls of long-range, broadband horizontal acoustic surveys. Benefits include 1) the ability to rapidly survey a large volume of water, 2) the ability to measure sparse distributions of fish which may be under-sampled by nets or downward-looking echosounders, and 3) the ability to classify mixed aggregations of swimbladder-bearing fish based on spectral analysis of the echoes. Potential challenges associated with these surveys include: 1) non-uniform sampling of the water column in depth due to the coupling of a directional sonar beam and the naturally refractive waveguide, 2) difficulties in inferring the depth of the aggregations in the absence of cotemporaneous downward-looking echosounder which is compounded by the fish length and depth dependencies of the scattering response of fish swimbladders, and 3) contamination of data from non-fish sources (e.g., rocky outcroppings, non-swimbladder-bearing fish, marine mammals, etc.). In order to reap the benefits of such surveys, it is clear that careful analysis of the data through comparisons with realistic propagation modeling of the environment and spectral modeling of scattering responses are necessary to extract reliably meaningful information from surveys of this nature.

From a military standpoint this study highlights several important characteristics of reverberation from aggregations of fish in shallow water. At mid-frequencies target-sized aggregations of swimbladder bearing fish can produce echoes with sufficient SNR to be observed above boundary reverberation in normalized, matched-filtered data. This is shown in the observed data for a 700 Hz bandwidth signal and simulations using a 100 Hz bandwidth signal. Furthermore, the distribution of echo envelopes from sparsely distributed aggregations, such as those observed near Franklin Swell in the Gulf of Maine, have highly non-Rayleigh (i.e., clutter-like) distributions of echo envelopes. A computationally inexpensive model has been shown to model the distribution of echo envelopes accurately. This model could potentially be used to help predict the

probabilities of false alarm from fish aggregations in other regions of the world's oceans given specific parameters of the sonar being employed and information pertaining to the density of fish aggregations in the area.

signal	signal type	W (Hz)	f_{min} (Hz)	f_{max} (Hz)	T_P (s)
LMN4U	LFM	700	3400	4100	2
LM4U	LFM	3500	1500	5000	2

Table 3.1 Parameters of signals analyzed in this study including signal type, bandwidth, W, minimum frequency, f_{min}, maximum frequency, f_{max}, and pulse length, T_P .

data set	time period (local)	Midpoint of Ship Track	number of pings	beam range
C	18:40:54–18:58:14	42.24N 68.90W	14	15–25
C2	18:36:54–18:58:14	42.24N 68.90W	16	25–30
D	18:58:14–19:16:54	42.23N 68.88W	15	20–30
E	19:16:54–19:50:14	42.22N 68.86W	25	20–30

Table 3.2 Long-range acoustic data sets defined by time of transmission and range of receiver beams from which data was drawn.

	Atlantic herring (note 1)	Silver Hake L < 12 cm (note 2)	Silver Hake L > 12 cm (note 3)	Acadian redfish L < 12 cm (note 2)	Acadian redfish L > 12 cm (note 4)
A	5×10^{-4}	5×10^{-4}	2.5×10^{-5}	5×10^{-4}	1×10^{-4}
ξ (Pa·s)	80	5	30	5	30
z (m)	152.9 m	152.9 m	152.9	152.9	184.3

Notes: 1) A and ξ are published parameters for 25 cm Atlantic herring at 182 m depth[17].
2) A and ξ are published parameters for "small mixed" fish at 82 m depth[17].
3) A and ξ are published parameters for silver hake at 55 m depth[17].
4) ξ is a published parameter for silver hake at 55 m depth[17]. A is obtained by fitting model to data sets C and C2.

Table 3.3 Resonant swimbladder scattering model parameters. The coefficient of the regression of swimbladder volume from fish length, *A*, and the viscosity of fish flesh, ξ, are published parameters in all cases except *A* for large Acadian redfish which is obtained by fitting to the data. Fish depths, *z*, are the midpoint of trawls in which the given species were caught in significant quantities at night.

data set	silver hake	Atlantic herring	Acadian redfish
C	0.08	0.15	0.77
C2	0.40	0.50	0.10
D	0.13	0.67	0.20
E	0.30	0.50	0.20

Table 3.4 Relative densities of various species of fish used in mixed-assemblage spectral modeling of echoes from aggregations of fish.

Parameter Name (units)	Parameter Value
Source Parameters	
Source Type	10-element VLA
Spacing of Elements (m)	0.248
Source Depth (m)	48
Source Location	42.23 N 68.88 W
Source Level (rms, dB)	207.37
Center Frequency (Hz)	3750
Bandwidth (Hz)	100
temporal shading	Hanning window (5% taper fraction on each end)
Receiver Parameters	
Receiver Type	32-element HLA
Element Spacing (m)	0.1524
Receiver Orientation	133° T (forward endfire)
Receiver Depth (m)	38
Environmental Properties	
Bathymetry	USGS database[83]
Sound-speed Profile (m/s)	CTD derived (range-independent)
Bottom Type	Sand-Silt-Clay[84,85]

Table 3.5 Parameters used in reverberation calculations using the Sonar Simulator Toolset (SST).

Parameter Name (units)	Parameter Value
Source Parameters	
Source Type	10-element VLA
Spacing of Elements (m)	0.248
Source Depth (m)	48
Source Location	42.23 N 68.88 W
Source Level	observed (note 1)
Center Frequency / Bandwidth (Hz)	3750 / 100
Receiver Parameters	
Receiver Type	32-element HLA
Element Spacing (m)	0.1524
Receiver Orientation	133° T (forward endfire)
Receiver Depth (m)	38
Fish Aggregation (school) Properties	
Depth (m)	155
Location, azimuthally (degrees)	155 ± 22 (starboard beams 20–30)
N_{hlts} (scatterers / resolution cell)	5
Morphology	Observed[19]
Diameter (horizontal extent, m)	~50
Thickness (vertical extent, m)	~10
Fish Density, ρ_s (fish/m^3)	0.02
Love Model Properties	
fish type	Atlantic Herring (physoclist)
fork length, L (m)	0.21
regression coefficient, A	5×10^{-4}
viscosity of fish flesh, ξ ($\text{Pa} \cdot \text{s}$)	80
Environmental Properties	
Bathymetry	database[83]
Mean Sound-speed Profile (m/s)	CTD derived
Bottom Type	database[84,85]
IW Parameters	
reference displacement, ζ_0 (m)	2
reference buoyancy frequency, N_0 (cycles/hr)	3
number of IW modes, $j_{\max}$	20
RAM Parameters	
frequency resolution (Hz)	1.69
range step (m)	1 / 0.02 (note 2)
depth step (m)	0.025
number of Padé terms	4
note 1: Source level is derived from observed power levels applied to the elements. note 2: Coarse range step is used for propagation to scatterer or receiver. Fine range step is used within scatterer aggregation or between elements of HLA.	

Table 3.6 Two-way parabolic equation modeling parameters.

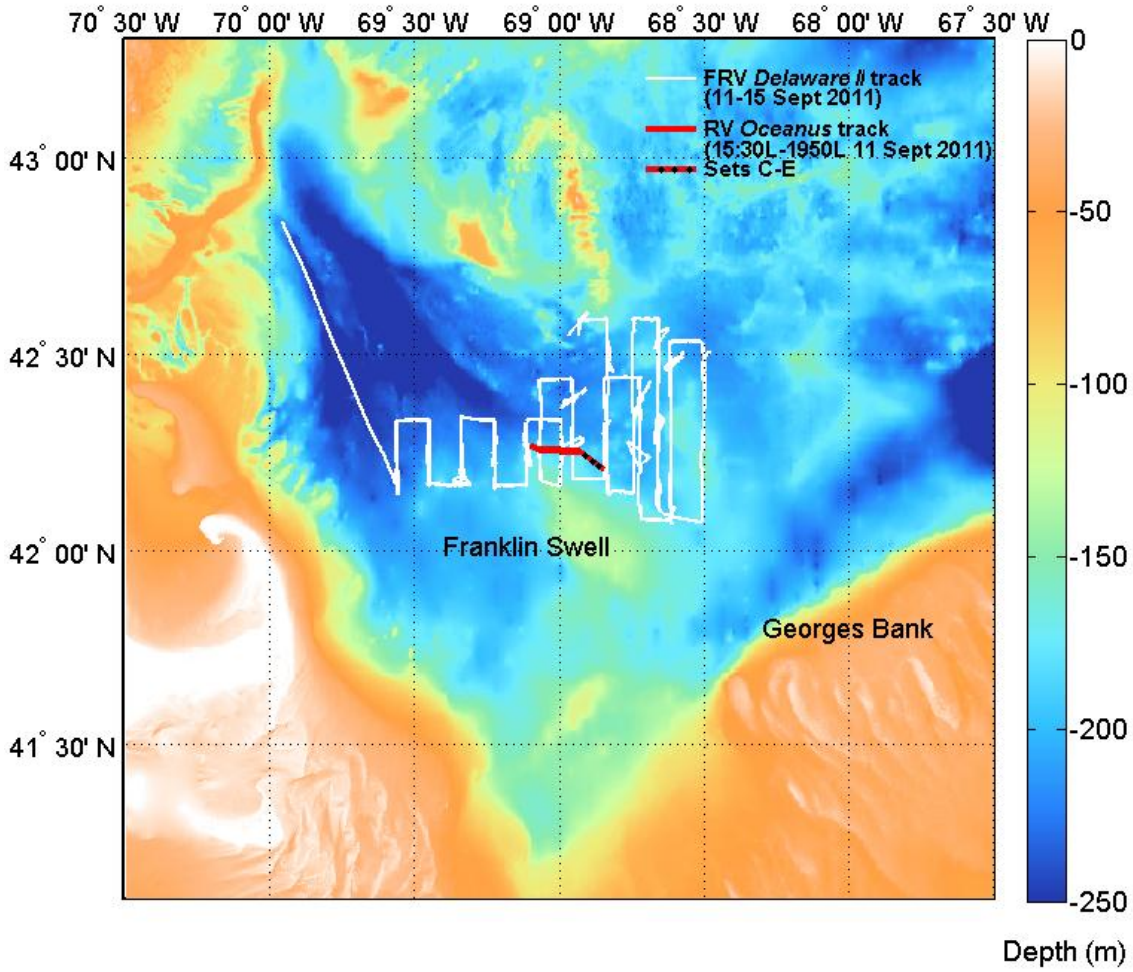

Figure 3.1 Map of the Gulf of Maine showing bathymetry and cruise tracks of FRV *Delaware II* from 11th-15th of September 2011, (white line) and RV *Oceanus* from 15:30 – 19:50 local on the 11th of September 2011 (red line). Black dots along *Oceanus* track represent midpoint of tracks where data sets C/C2, D, and E were collected, northwest to southeast, respectively.

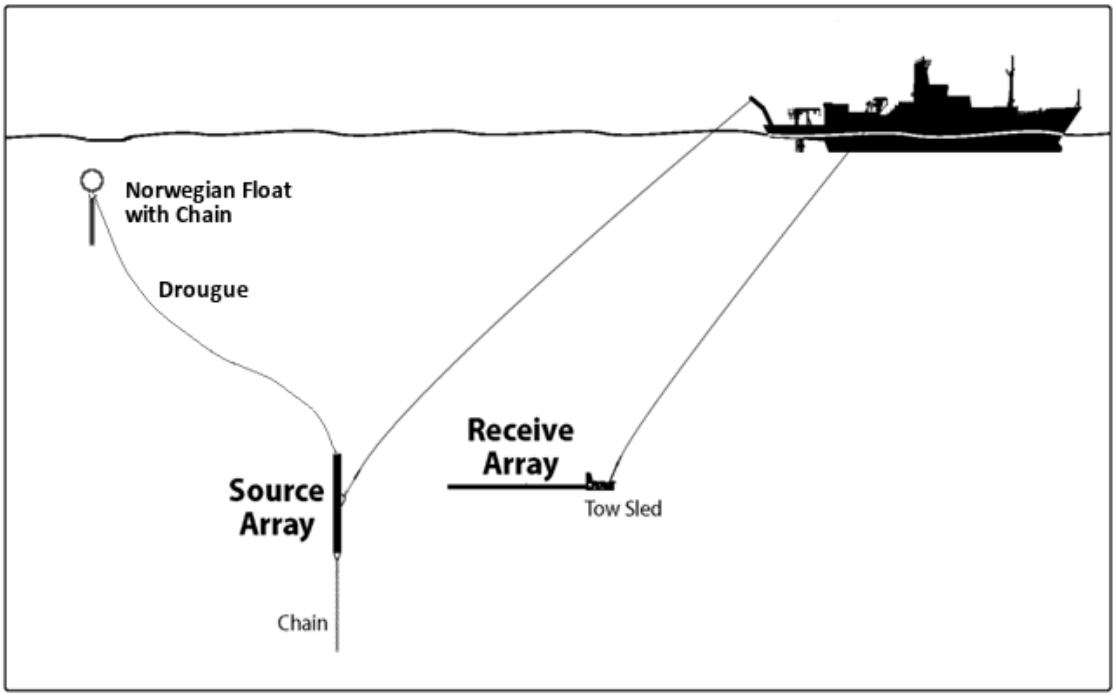

Figure 3.2 Deployed configuration of NRL long-range, horizontal-looking sonar system.

Figure 3.3 Cartoon illustrating the split-window normalization technique (from Fialkowski et al., 2010)[2]. Illustration shows auxiliary bands (AB_U and AB_L), guard bands (GB_U and GB_L), and sample being normalized, "o."

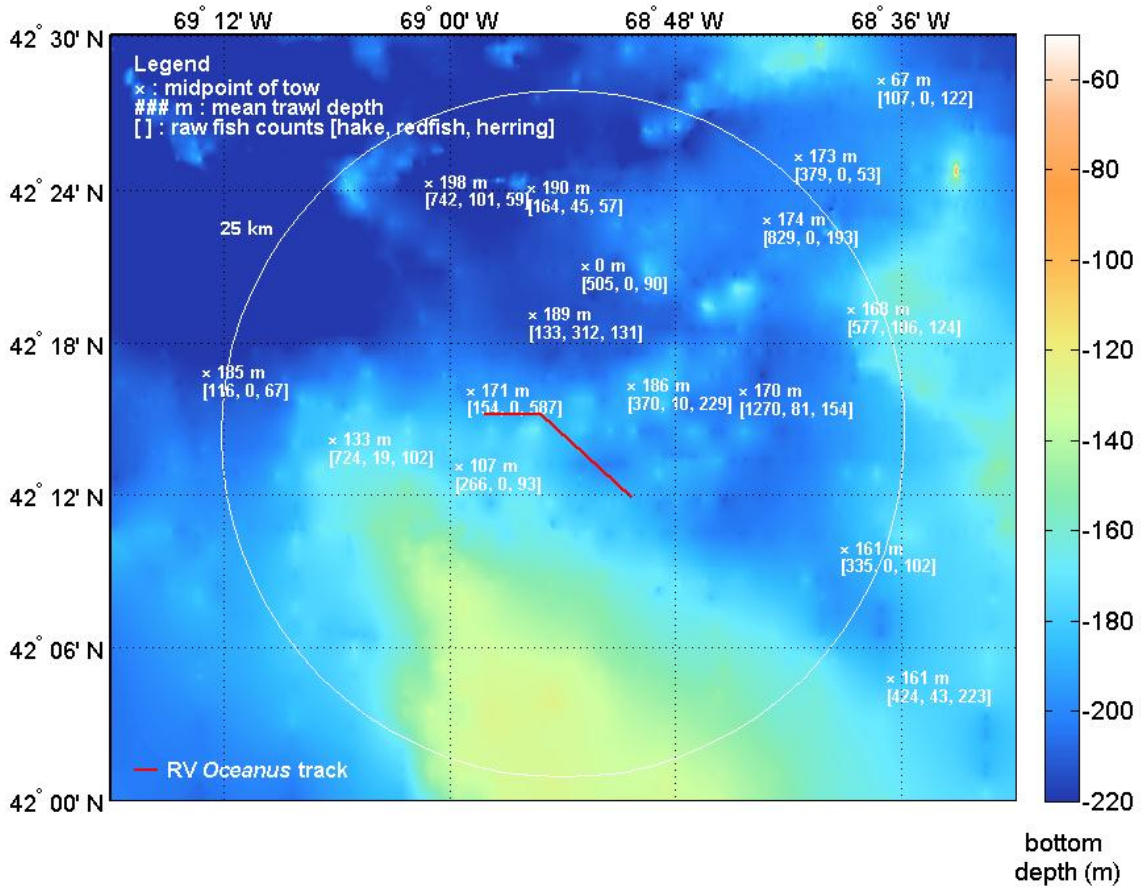

Figure 3.4 Trawl tows conducted from FRV *Delaware II* between the 11th and 15th of September 2011. White crosses mark the midpoint of each tow annotated with the depth in meters. Numbers in brackets are the raw fish counts in each haul for the three species that comprised the majority of the trawl catches [silver hake (*Merluccius bilinearis*), Acadian redfish (*Sebastes fasciatus*), Atlantic herring (Clupea harengus)]. The red line is the track of the RV *Oceanus* on the 11th of September 2011. The white circle is a 25 km radius drawn about the midpoint of the RV *Oceanus* track. Only tows conducted within this circle were considered in this analysis.

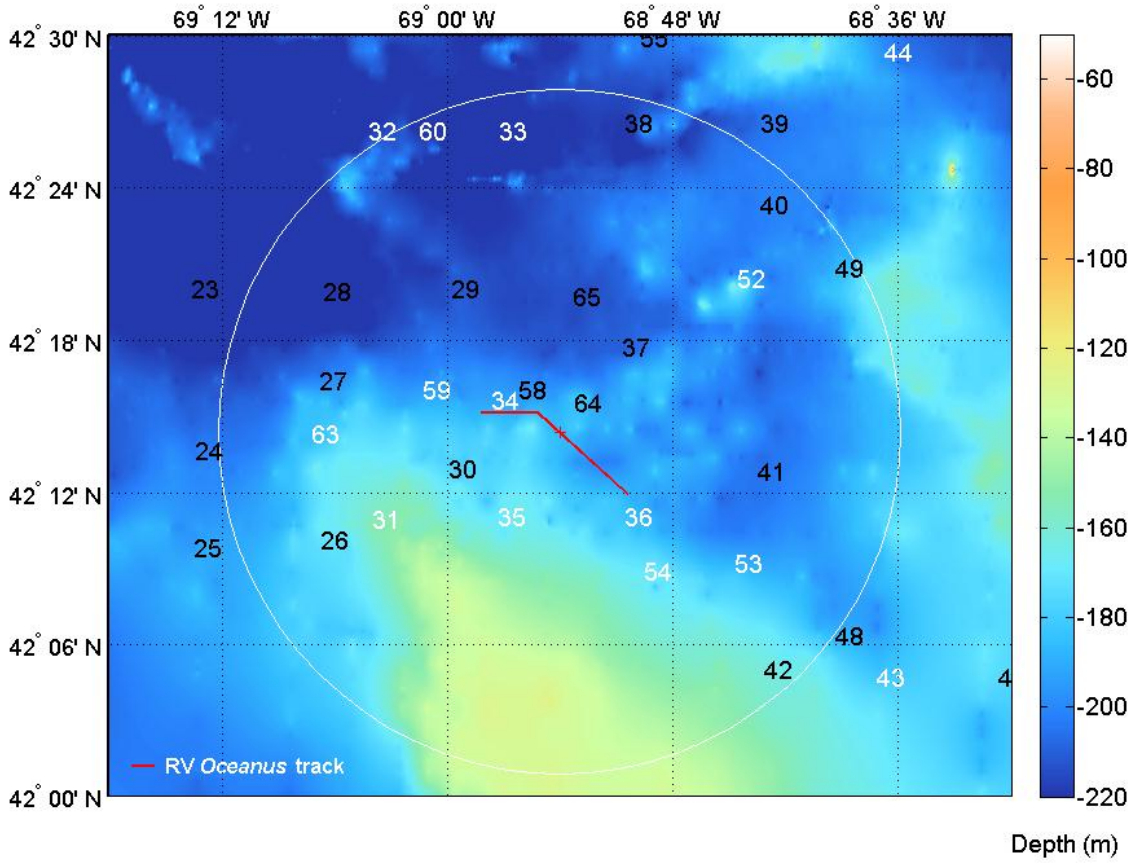

Figure 3.5 Map of CTD cast stations from FRV *Delaware II* during times of 0:00 to 11:59 local (white) and 12:00 to 23:59 local (black) between the 11th and 15th of September 2011. The red line is the track of the RV *Oceanus* on the 11th of September 2011.

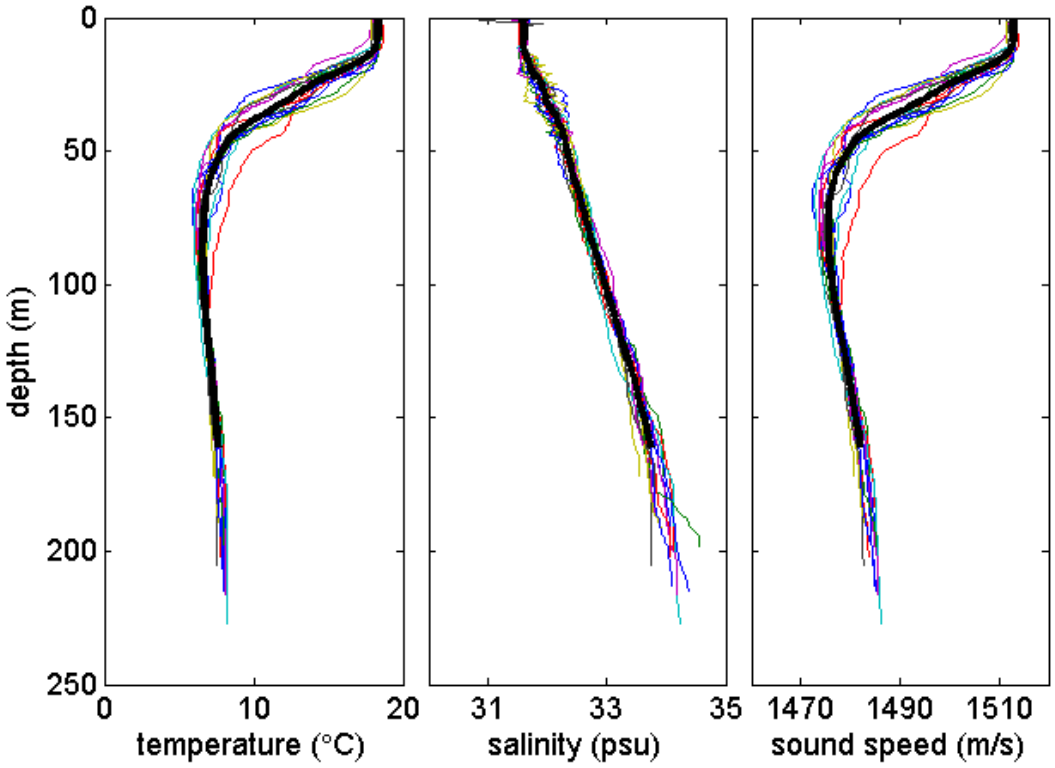

Figure 3.6 Temperature, salinity, and sound-speed profiles (left to right) derived from CTD casts taken from FRV *Delaware II* during times of 12:00 to 23:59 local (see Figure 3.5) between the 11th and the 15th of September 2011. Mean profiles are shown in thick black curves.

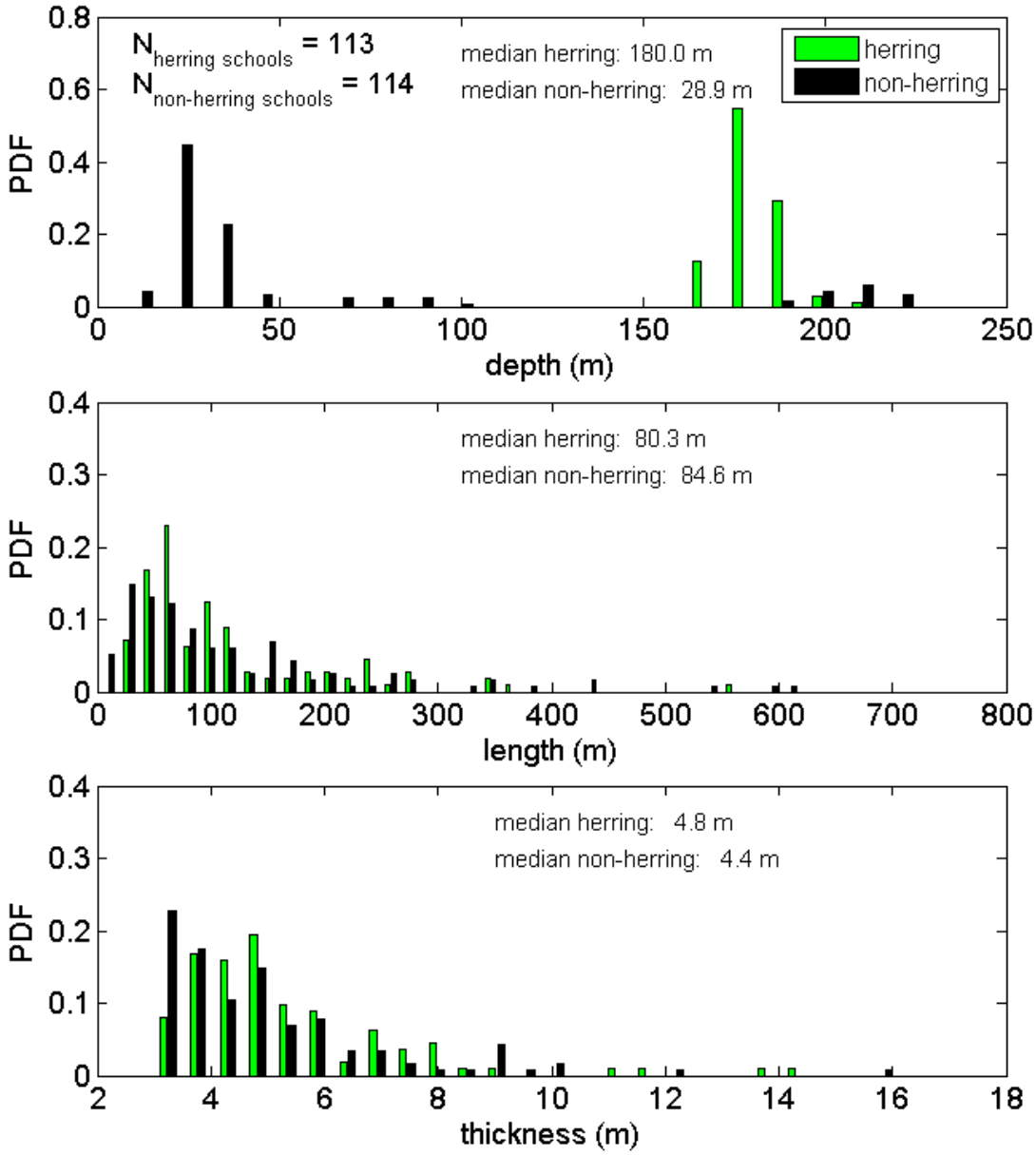

Figure 3.7 Normalized histograms of fish school characteristics (mean depth – top panel, length – middle panel, mean thickness – bottom panel) derived from *day* measurements of a downward-looking, multi-frequency echosounder from the FRV *Delaware II*. Data are divided into Atlantic herring (green) and non-herring (black) schools. Length distributions are truncated at 800 m to better display results. Total numbers of schools observed, $N_{\_,schools}$, for each group, are given in the top left of each panel. Median values are given in the top center of each panel.

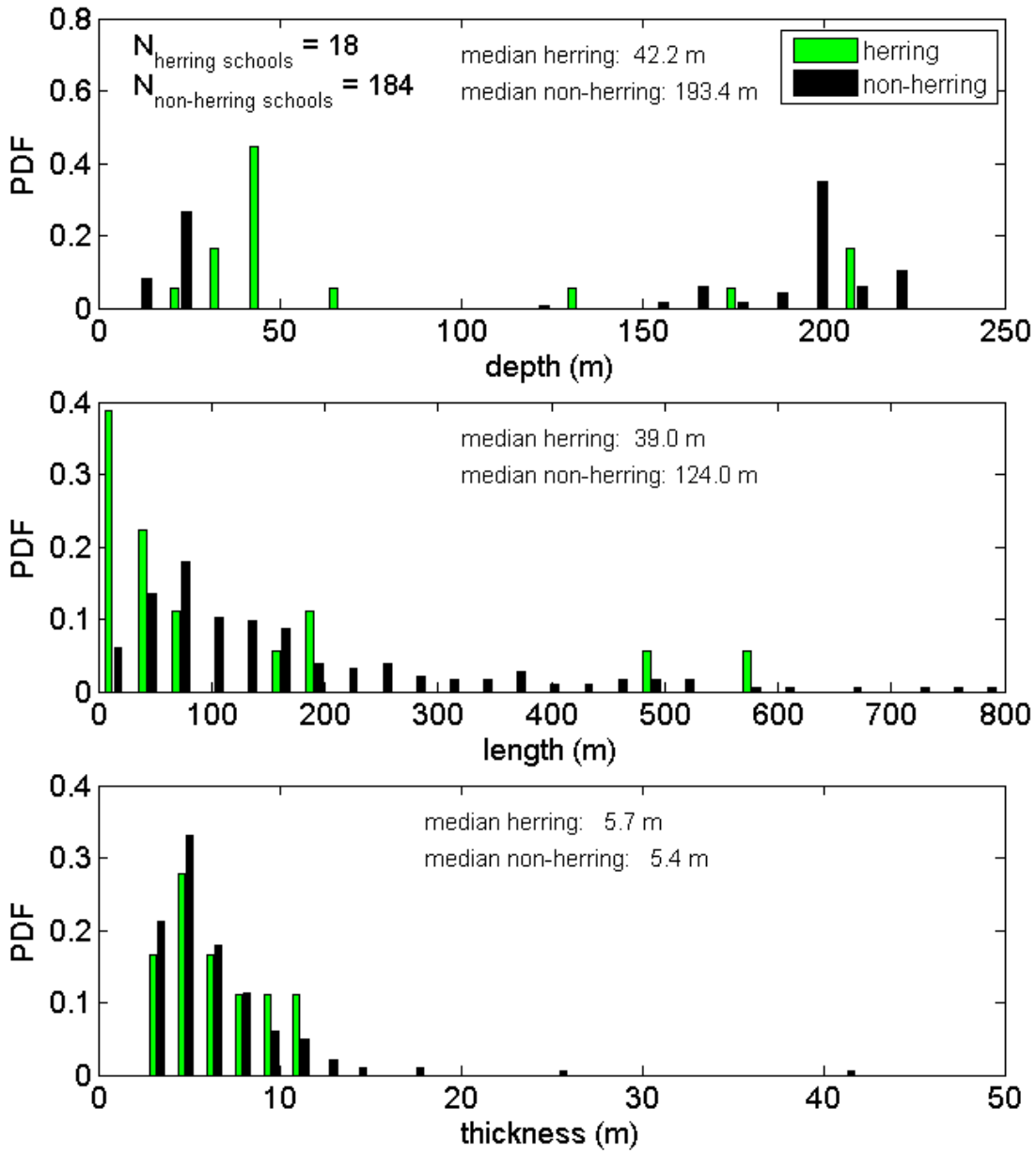

Figure 3.8 Normalized histograms of fish school characteristics (mean depth – top panel, length – middle panel, mean thickness – bottom panel) derived from *night* measurements of a downward-looking, multi-frequency echosounder from the FRV *Delaware II*. Data are divided into Atlantic herring (green) and non-herring (black) schools. Length distributions are truncated at 800 m and a single Atlantic herring school thickness outlier at 84.3 m is not shown to better display results. Total numbers of schools observed, $N_{\_,\text{schools}}$, for each group, are given in the top left of each panel. Median values are given in the top center of each panel.

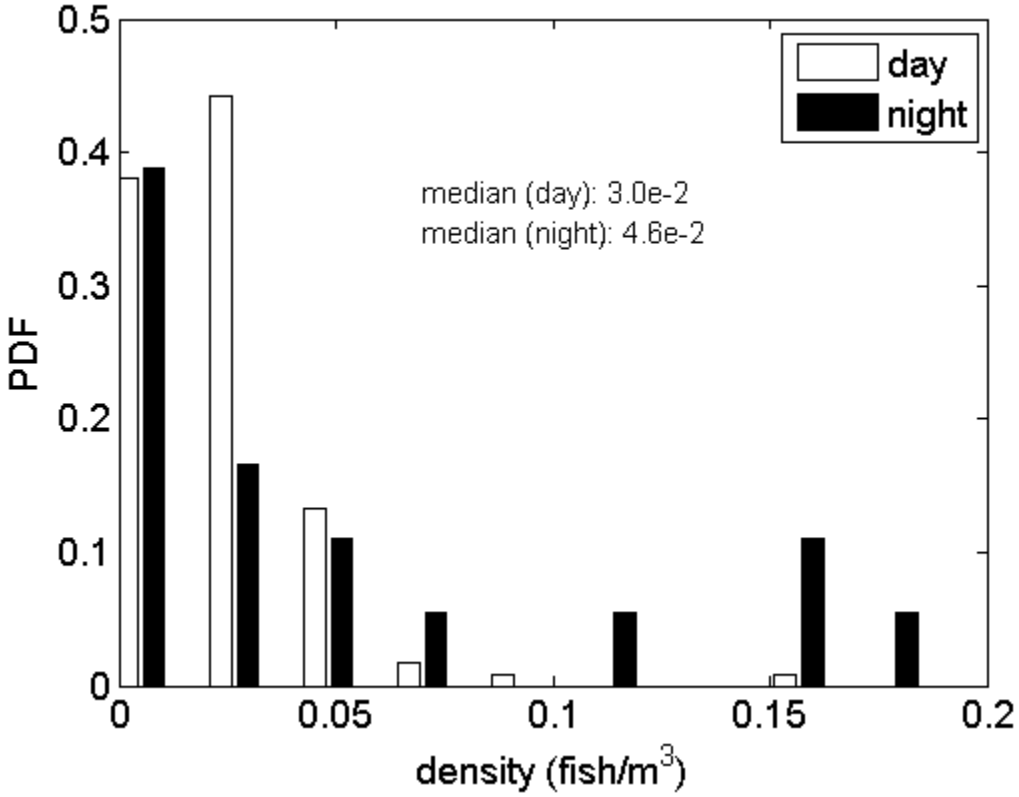

Figure 3.9 Normalized histograms of densities of schools of Atlantic herring derived from daytime (white) and nighttime (black) measurements of a downward-looking, multi-frequency echosounder from the FRV *Delaware II*.

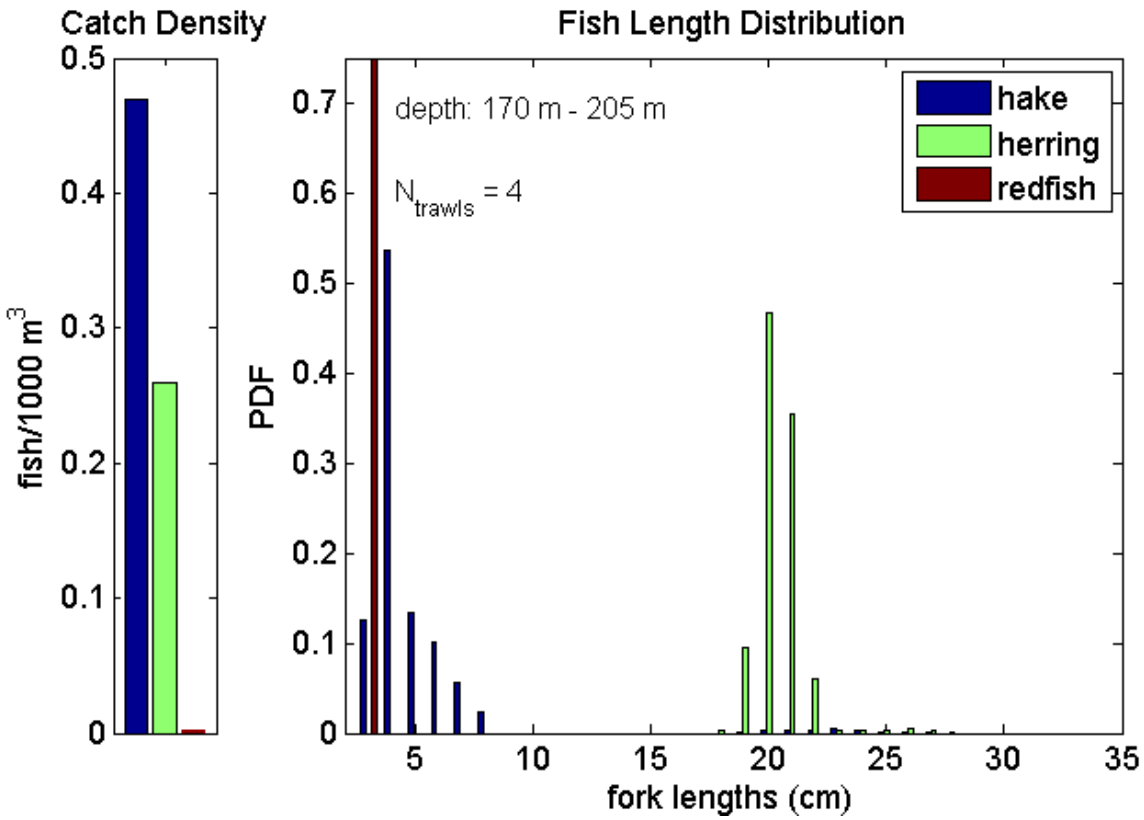

Figure 3.10 Catch density and length distribution of three species of fish caught during *day* trawls from FRV *Delaware II*: silver hake (blue), Atlantic herring (green), Acadian redfish (red). Left panel shows catch density (i.e., numbers of fish caught per 1000 cubic meters of water sieved). Note that catch density is *not* used as a proxy for fish aggregation density. Right panel shows normalized fork length distributions. The low probability values above 23 cm are a mix of Atlantic herring and silver hake.

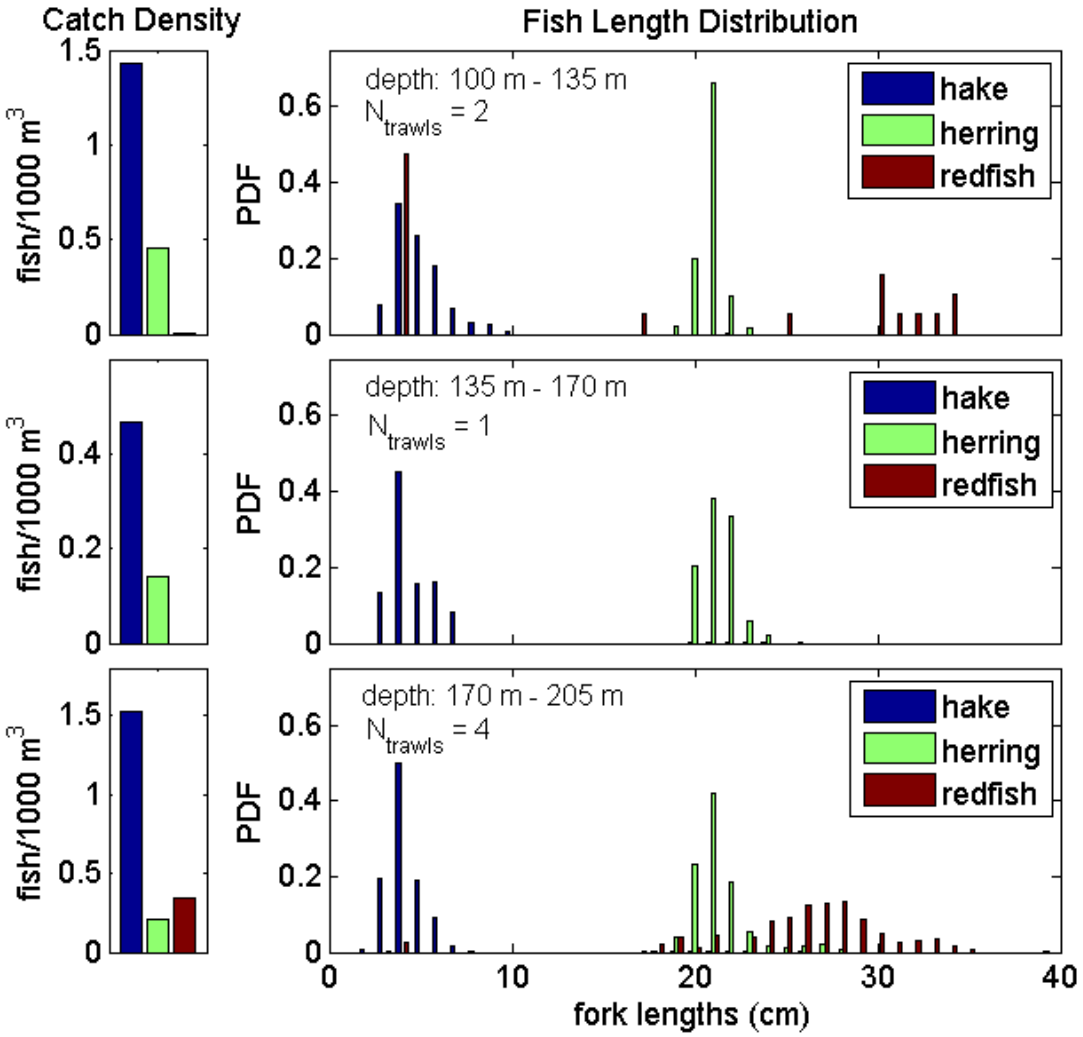

Figure 3.11 Catch density and length distribution of three species of fish caught during *night* trawls from FRV *Delaware II*: silver hake (blue), Atlantic herring (green), Acadian redfish (red). Left panel shows catch density (i.e., numbers of fish caught per 1000 cubic meters of water sieved). Note that catch density is *not* used as a proxy for fish aggregation density. Data are sub-divided by mean depth of trawl: 100–135 m (top panels), 135–170 m (middle panels), 170–205 m (bottom panels).

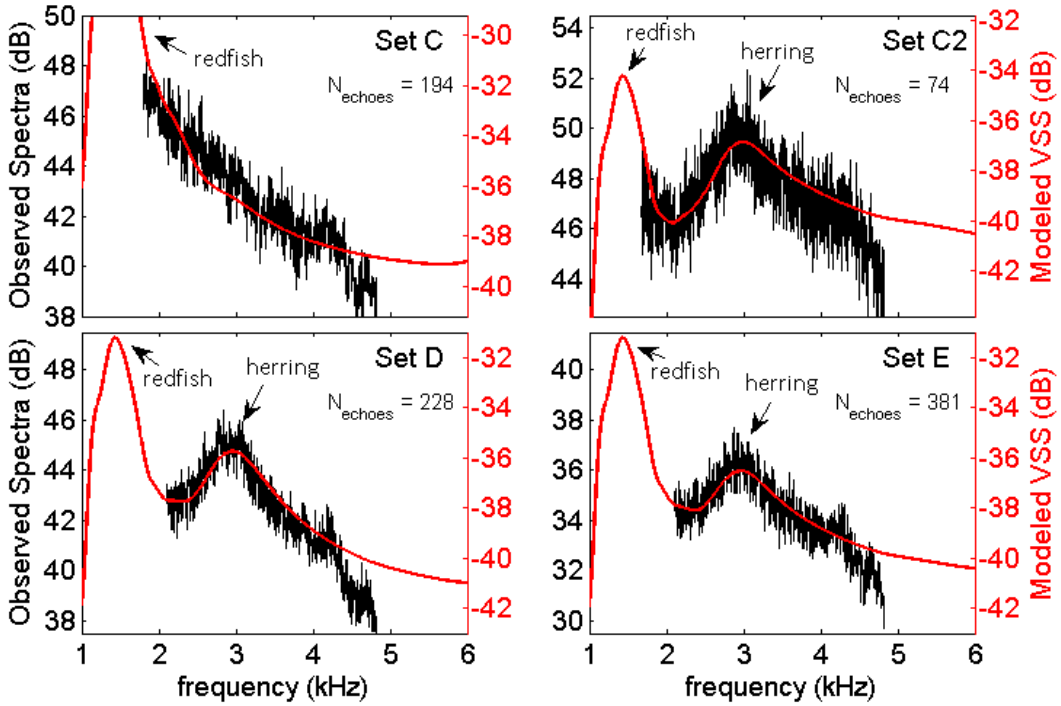

Figure 3.12 Mixed assemblage model (red) fit to observed spectra (black) for four sets of data. Observed data are averaged, match-filtered data over N_{echoes} spectra (number given in top right of each panel). Model predictions are volume scattering strength of a mixed assemblage of silver hake, Atlantic herring, and Acadian redfish with relative densities (given in Table 3.4). Key modeling parameters of the underlying resonant scattering model are given in Table 3.3. Arrows indicated resonance peak in model and data (when in source band) of given species.

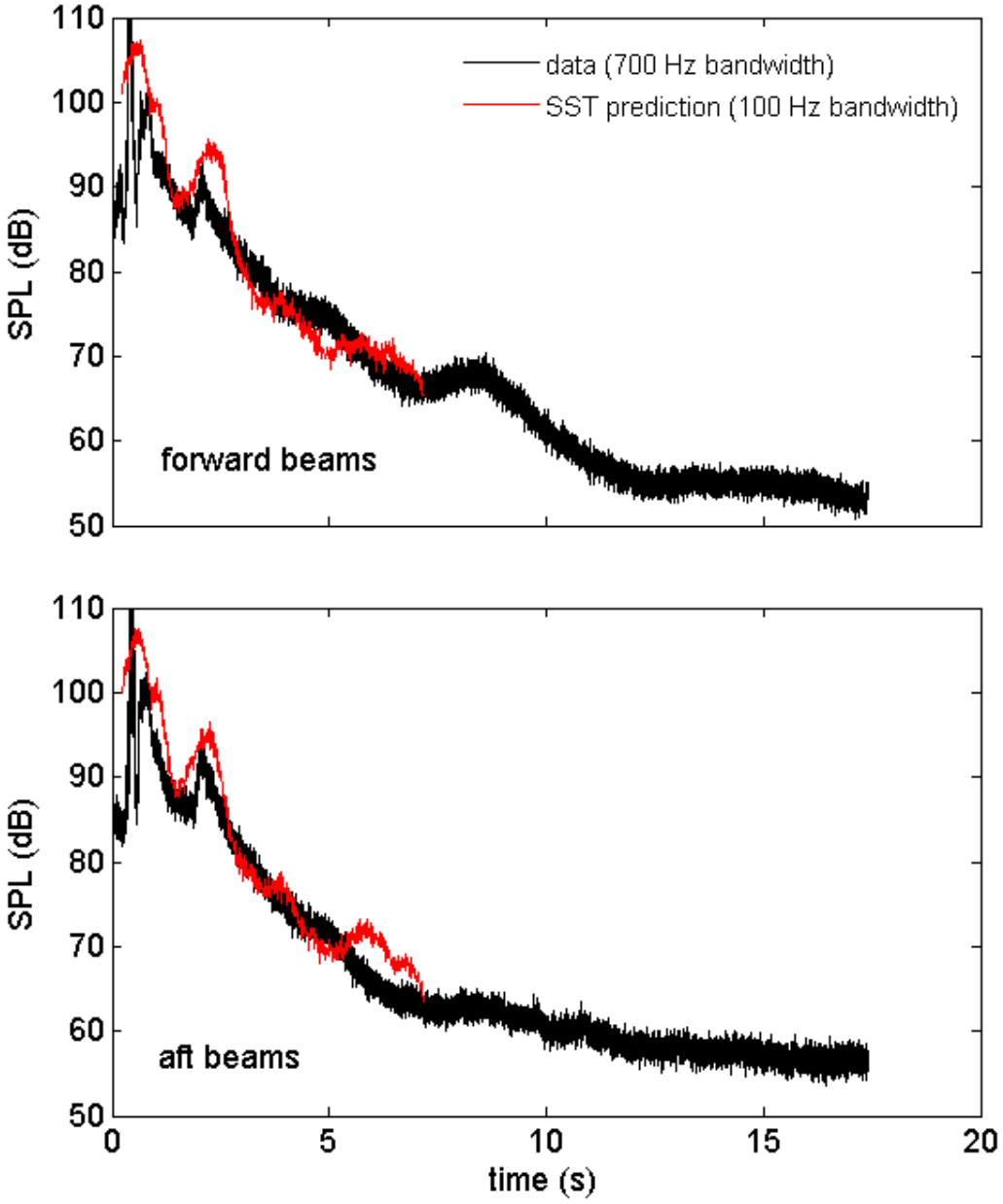

Figure 3.13 Comparison between observed reverberation level (black) and SST predictions averaged over forward beams (top panel) and aft beams (lower panel). Observed data are 700 Hz bandwidth while predictions are for a 100 Hz bandwidth signal.

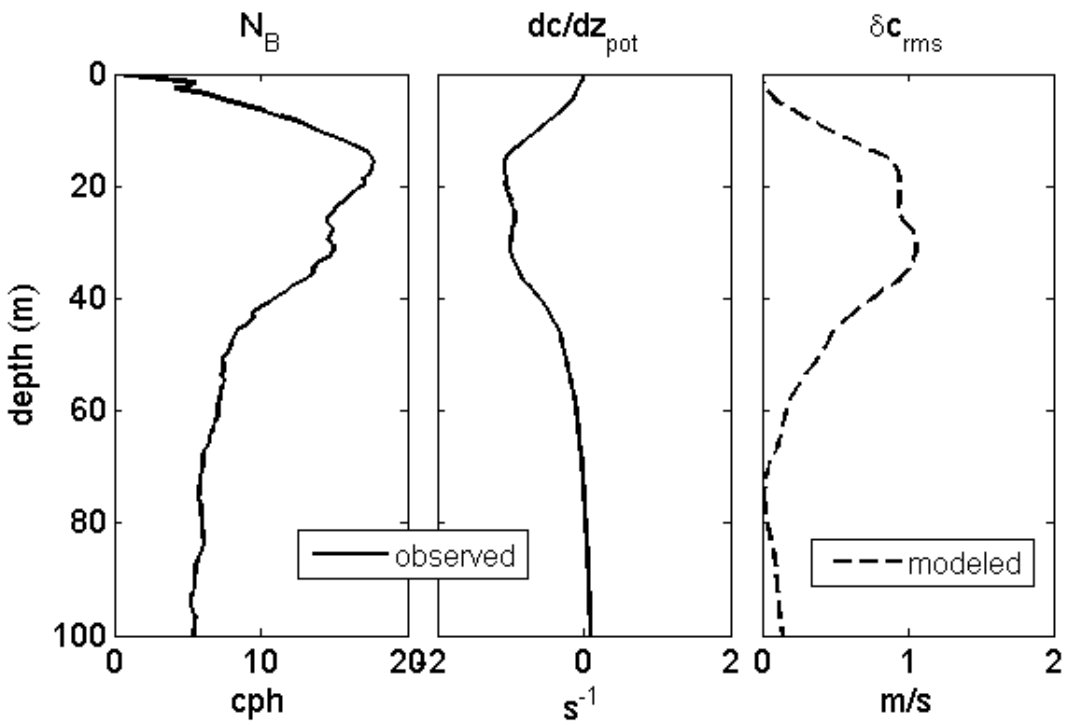

Figure 3.14 Water column profiles associated with observed mean profile (thick black curves, Figure 3.6) from Franklin Swell area in the Gulf of Maine from September 2011. Profiles shown are buoyancy frequency (left panel), the derivative of potential sound speed with depth (center panel), and. modeled range-averaged, rms sound-speed perturbation (right panel).

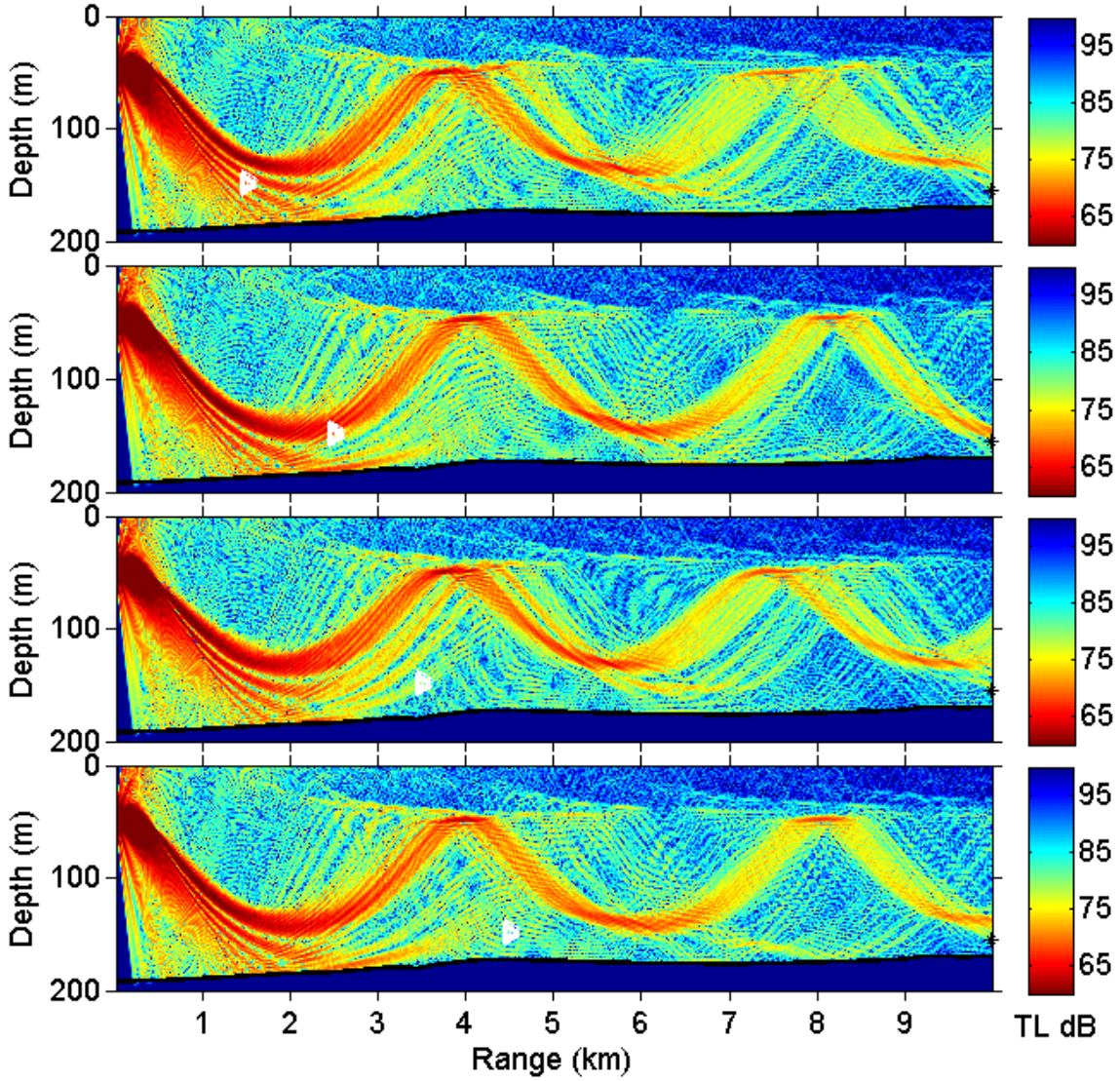

Figure 3.15 Transmission Loss for four realizations of internal wave fields. White triangles are representative examples of fish schools located at a mean depth of 155 m and ranges of approximately 1.5, 2.5, 3.5 and 4.5 km.

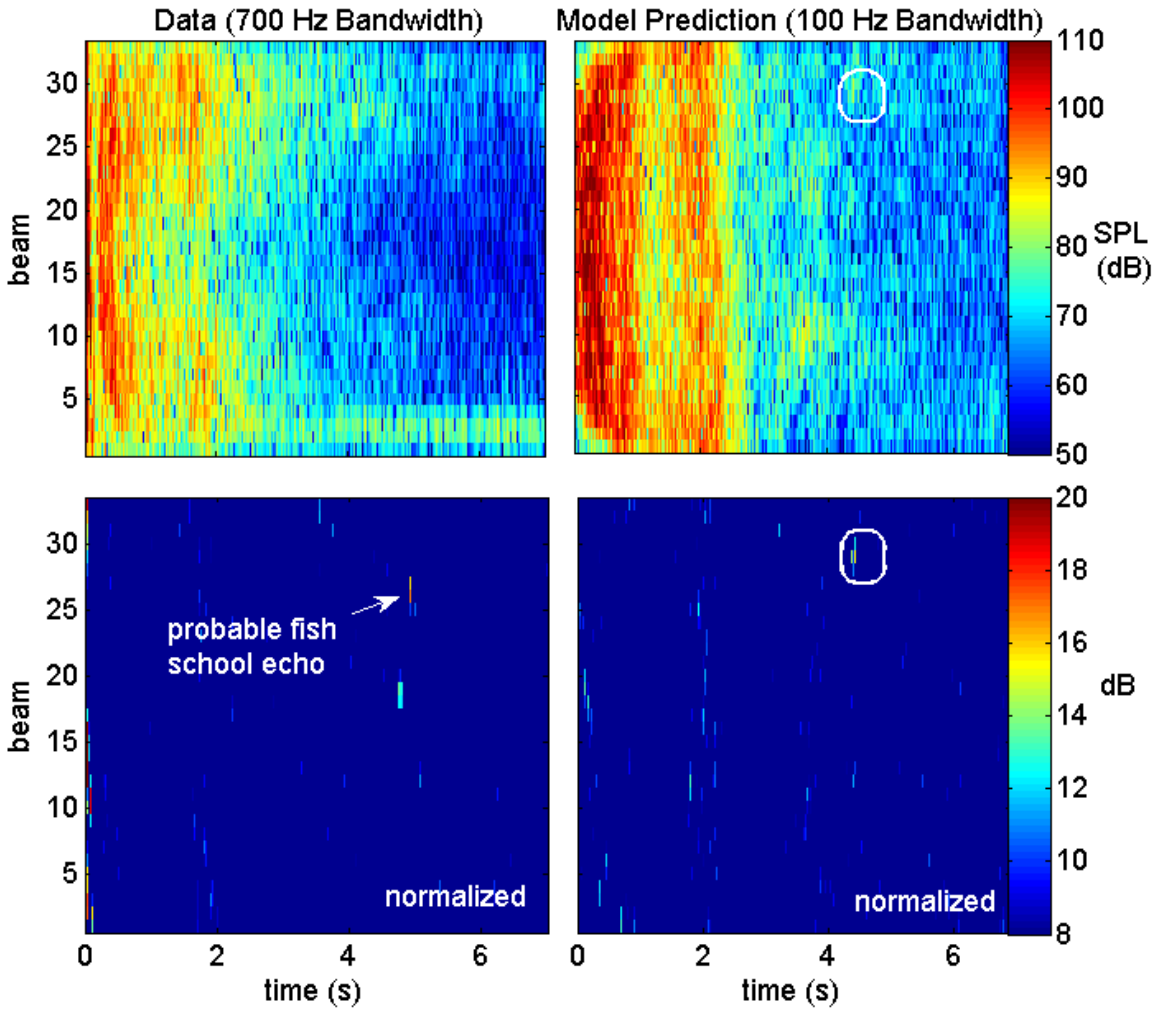

Figure 3.16 Sample comparison between an acoustic measurement by a long-range, horizontal-looking sonar (left panels) and a model prediction (right panels). Acoustic measurement was made at 19:14:54 local on September 11th, 2011, near Franklin Swell in the Gulf of Maine. Top panels show matched-filtered data, while lower panels show matched-filtered, split-window-normalized results. An echo that is likely from a fish school is identified in the normalized data with a white arrow. The modeled fish echo is circled in right two panels.

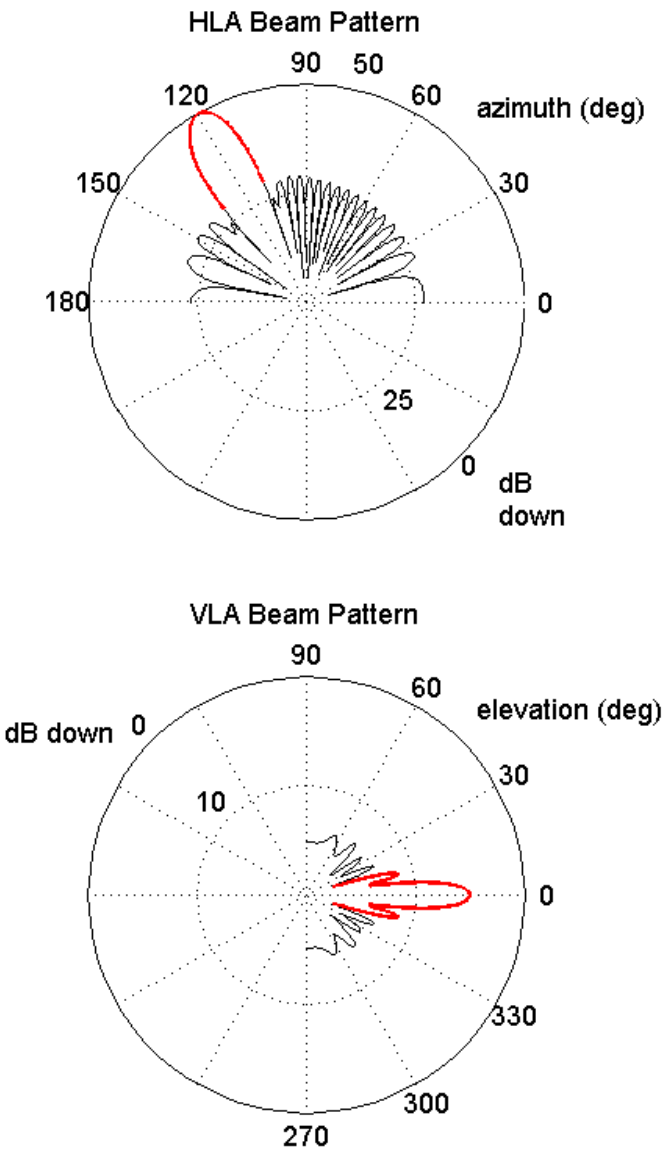

Figure 3.17 Theoretical beampatterns in terms of pressure envelope at 3.75 kHz (black) for beam 25 of a shaded 32-element HLA (top panel) and a shaded 10-element VLA (bottom panel). HLA shading is a hamming window; while, VLA shading is based on average observed power drawn by VLA elements. Solid red line is the angular extent of the location of scatterers within the beam used in the numerical phasor summation simulations (i.e., main lobe for HLA, and main lobe and first side lobe for VLA).

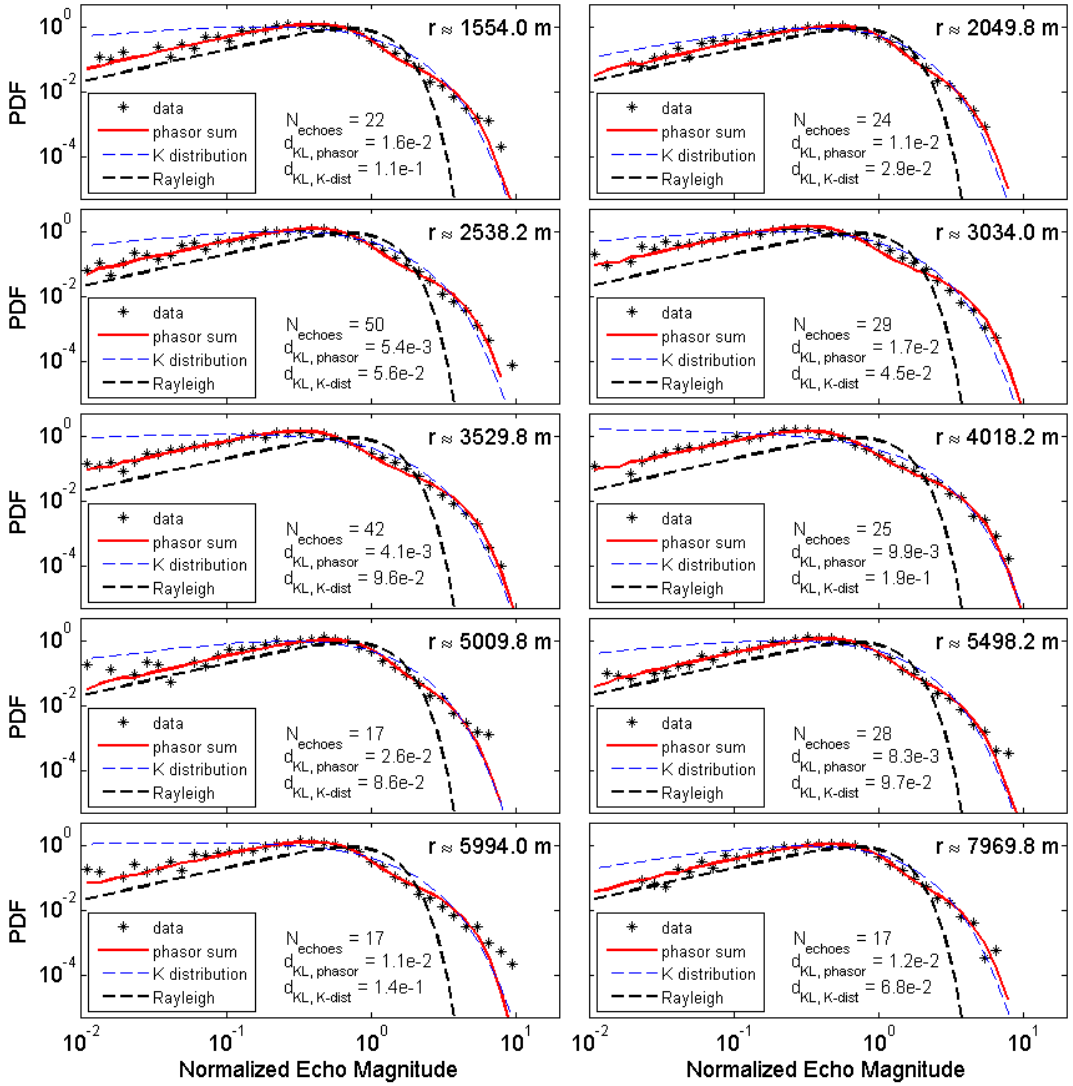

Figure 3.18 Comparison of observed echo magnitude PDFs (black asterisks) for scatterers at various ranges from Sets C2, D and E, with predictions by numerical phasor summation mehtod (red solid), and the K distribution (blue-dashed). The Rayleigh distribution (black dashed) is provided for reference. The range, r, in the top right of each panel (derived from two-way travel time) is the approximate range to the beginning of a ~500 m range bin where echoes were collected. Results shown are limited to cases where the number of echoes in the ensemble, N_{echoes}, (given in the center of each panel) is ≥ 15. The Kullback-Leibler distances for the numerical phasor summation prediction, $d_{KL,\ phasor}$, and K-distribution, $d_{KL,\ K\text{-}dist}$, are also given in the center of each panel.

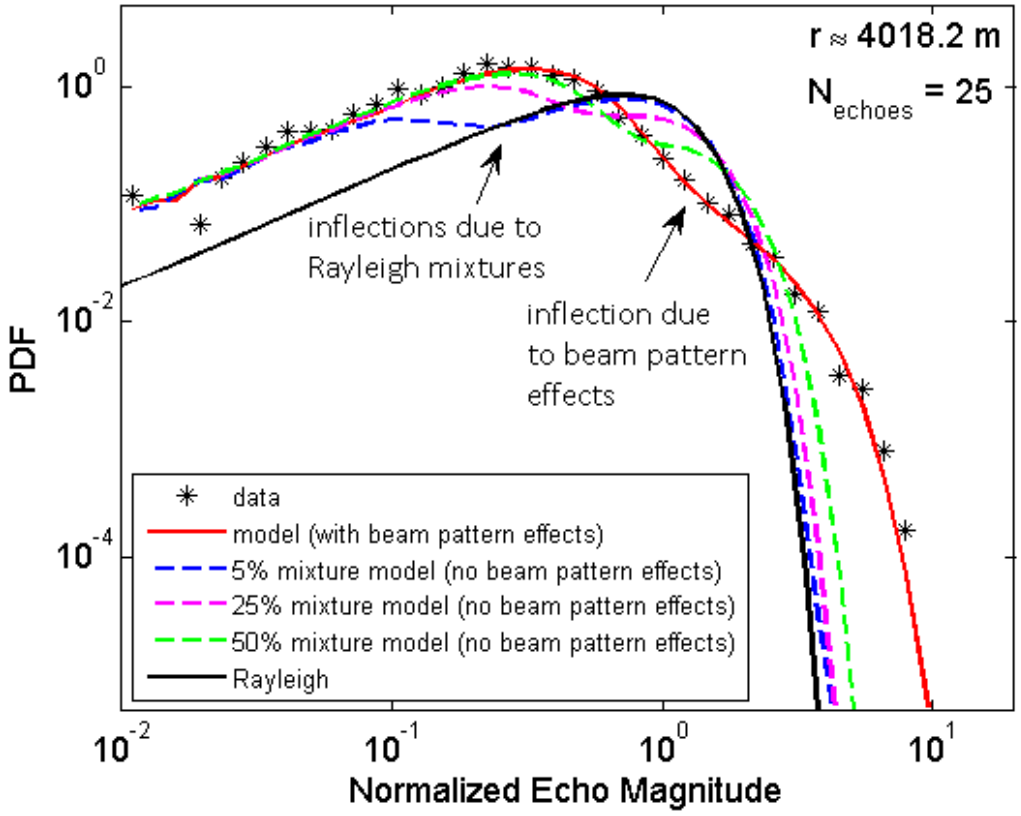

Figure 3.19 Comparison of observed echo magnitude PDFs (black asterisks) for scatterers in a single range bin ($\approx$ 4018.2 to 4518.2 m) from Sets C2, D and E, with a mixture model using a two-part Rayleigh mixture and no beampattern effects (dashed), and a phasor summation calculation including beampattern effects and no mixture (red solid). The Rayleigh distribution (black solid curve) is provided for reference.

THIS PAGE INTENTIONALLY LEFT BLANK

IV. CONCLUSION

This study has focused on the effects of various physical factors on the statistics of echoes from scatterers, ensonified by an active sonar system, in the water column of a random oceanic waveguide. Facilitating this work was the development of a range-dependent two-way parabolic equation (PE) model, for calculating volume reverberation by aggregations of fish in the water column. Key components of this model include: 1) diffuse broadband internal-wave induced, perturbations of the mean sound-speed profile, 2) resonant acoustic scattering by aggregations of swimbladder-bearing fish, and 3) realistic morphology of fish aggregations. Numerical simulations, using this model with parameters describing various levels of system complexity, have aided in examining the contributions to the echo statistics of 1) a shallow water waveguide, 2) range-dependent, stochastic water column properties, 3) a directional acoustic source, 4) a variable scattering response, and 5) an extended scattering volume. Of particular interest has been the relationship between these various factors and the degree to which the echo envelope distributions are non-Rayleigh (a key characteristic in determining the likelihood of an echo causing a false alarm). Results of these analyses were validated, in part, through comparisons with measurements of compact schools of swimbladder-bearing fish made by a broadband, horizontally looking sonar.

A. MODELING AND ANALYSIS

The complex interaction between an acoustic source, a shallow-water waveguide, and a scattering volume was examined in Chapter II of this study. It is shown that randomness of the waveguide, directionality of the sonar system, and extent of the scattering volume are all of primary importance to the echo statistics. While it is clear that an omnidirectional source in a shallow waveguide produces strong multipath interference at all ranges, it is shown that the combination of a directional sonar beam in a refractive waveguide, with no added randomness to the waveguide, can significantly limit scattering from the boundaries. This results in a pressure field that remains unsaturated to fairly long ranges (at least 10 km in a 200 m deep waveguide). However, at ranges much shorter than these, adding natural randomness to the waveguide, such as

internal-wave induced range-dependent perturbations to the sound speed of the water column, is shown to play an important role. This randomness has two important contributions, first by filling in shadow zones and second by causing strong interference of forward scattered acoustic waves that induces a saturated environment at fairly short ranges (e.g., a few kilometers for a 200 m deep waveguide). This rapid evolution toward a saturated environment is important in predicting the echo statistics. It is shown that a single scatterer randomly located in a saturated waveguide, with a constant scattering response, has a distribution of echo envelopes that is exponentially distributed before beampattern effects. Furthermore, in cases of directional beampatterns, is shown that, with knowledge of the beampattern, scatterer density, and the number of scatterers ensonified at a given range, accurate predictions of the echo statistics can be made.

The significance of beampattern effects and the contribution to non-Rayleigh statistics for scatterers in a waveguide has been shown by dividing the beampattern into the vertical and azimuthal components. For scatterers located at long ranges in a saturated pressure field the contribution of the vertical component of the beampattern is limited, approximately, to the main lobe as higher angle energy is attenuated by bottom interaction. Meanwhile, the echo statistics have been shown to depend upon the full beampattern as a function of azimuth. Importantly, though, the numerical simulations from which these results are derived do not account for background noise or reverberation; and, as was seen in comparison with observations, scatterers located outside of the main lobe may not be observed above the background reverberation rendering the azimuthal sidelobes less significant.

Also examined were the effects of extended scatterers with variable scattering responses simulating, for example, aggregations of fish. It is shown in this study that the distribution of echo envelopes is sensitive to the size of the scattering volume. Before beampattern effects a point scatterer located in a saturated waveguide with a zero-mean complex Gaussian response (i.e., a Rayleigh scatterer) has a strongly non-Rayleigh distribution due to waveguide effects, while an extended Rayleigh scatterer has an increasingly Rayleigh-like distribution of echo envelopes with increasing size.

Results of these analyses led to the development of a computationally efficient, numerical method for predicting echo envelope statistics for an arbitrary number of scatterers randomly located in a saturated waveguide and ensonified by a directional source. This phasor summation method, which is mathematically equivalent to the Chu-Stanton Theory, is applied to long-range echoes by accounting for waveguide effects as follows: 1) the beampattern as a function of elevation is truncated by limiting the domain to launch angles (i.e., elevation angle at the source) near horizontal where energy propagates further in the waveguide, and 2) the probability density function representing the scattering response has been modified to account for the squaring effect of the waveguide. This model is of particular value in that it is physics-based and, thus, predictive rather than empirically fit such as the K distribution that is commonly used to describe the statistics of sonar clutter.

B. MEASUREMENTS

The modeling results are validated, in part, by long-range horizontal acoustic measurements of compact scatterers in shallow water detailed in Chapter III of this study. Classification of long-range echoes is a challenge; therefore, a significant portion of this analysis was dedicated to inferring the source of the echoes observed on the horizontally looking system. Spectral and temporal analyses of the long-range horizontal-looking data combined with downward-looking acoustic data and biologic samples determined that the sources of the observed echoes were most likely sparse, compact aggregations of swimbladder-bearing fish with target-like sizes (~50–250 m in horizontal extent).

Quantitative analysis of the horizontal acoustic measurements showed that the echo statistics had little range dependence over the observed ranges (~1.5 – 8 km). Importantly, in these data, the aggregations are sparsely distributed, so that the number of aggregations within any range cell is, on average, just one. This lack of range dependence seen in the observations validates the modeling results which have shown that, for scatterers in a saturated pressure field, the statics remain stable with range in the case where there are a fixed number of scatterers in a resolution cell. The importance of this result is in showing that the dependence upon the beampattern (i.e., what portion of the beampattern contributes to the statistics) appears stable over the ranges studied (1–8 km).

Furthermore, although the relative contributions to the randomness from internal waves, bottom roughness, surface roughness or other stochastic parameters is not well known, it is clear that sufficient randomness exists in this shallow water environment to rapidly drive the pressure field to saturation. Finally, it is expected that, because many of these characteristics are ubiquitous in shallow water (e.g., internal waves and boundary roughness) these results can be applied to any littoral environment.

C. CONTRIBUTIONS OF THIS DISSERTATION

1. Contributions to the Ocean Acoustic Community

- Through extensive modeling, analysis, and comparison with observations, identified key physical factors that significantly contribute to the echo statistics of scatterers in the water column of a shallow water waveguide.
- Developed a two-way parabolic equation (PE) model for calculating volume reverberation by aggregations of scatterers in the water column that is capable of incorporating realistic randomness due to diffuse, broadband internal waves.
- Demonstrated an efficient numerical calculation for predicting the probability distributions of echo envelopes by aggregations of scatterers in a waveguide.
- Demonstrated techniques for classifying long-range echoes, measured by a horizontally looking sonar system, from aggregations of swimbladder-bearing fish.

2. Contributions to the United States Navy Sonar Community

- Demonstrated, by observations and numerical modeling, the possible significance of sparsely distributed, target-sized aggregations of swimbladder bearing fish as sources of clutter to mid-frequency, long-range sonar systems.
- Implemented a scattering model that simulates reverberation from realistically shaped aggregations of swimbladder-bearing fish that can for use in mid-frequency sonar simulations.

- Identified a key weakness in Navy Standard Parabolic Equation (NSPE) model in calculating acoustic propagation by mid-to-high frequency sources due to single-precision formulation of source code.

D. RECOMMENDATIONS FOR FUTURE WORK

This study inspires several interesting scientific questions for future research, for example: 1) What is the geographic variability of fish aggregations as it pertains to sonar clutter characteristics? 2) What other significant physical processes in shallow water effect echo statistics and to what degree (e.g., non-linear internal waves (solitons) and horizontal refraction of acoustic waves)? From a Navy point of view important questions include: 1) Are sparse, target-sized aggregations of mid-frequency-resonant fish unique to the Gulf of Maine or are they widely distributed throughout the world's oceans? and 2) Can the clutter-like nature of other scatterers in the ocean (e.g., shipwrecks, marine mammals, bubble clouds) be characterized using similar methods to those presented in this work.

THIS PAGE INTENTIONALLY LEFT BLANK

APPENDIX A: DERIVATION OF THE SPLIT-STEP PADÉ SOLUTION TO THE PARABOLIC EQUATION

The parabolic equation is a small propagation angle approximation to the wave equation that is readily adapted to range dependent problems. Using Padé approximations, the range dependent Helmholtz equation can be solved by a range-marching finite element method in which the properties within each element are treated as range independent. The range step can then be varied depending on the rate of change of the range dependent parameters to obtain the required accuracy.

Following the derivation provided in Jensen et al. (1993)[86] and assuming azimuthal symmetry, the 2D Helmholtz equation is written in cylindrical coordinates as

$$\frac{\partial^2 P}{\partial r^2}+\frac{1}{r}\frac{\partial P}{\partial r}+\frac{\partial^2 P}{\partial z^2}+k_0^2 n^2 P=0 \quad , \tag{A.1}$$

where, $k_0=\omega/c_0$ and $n=c_0/c(r,z)$. Next, assuming a solution in the far-field ($k_0 r>>1$) is of the form

$$P(r,z)=\Psi(r,z)H_0^{(1)}(k_0 r) \quad , \tag{A.2}$$

where Ψ is a slowly varying envelope function and the Hankel Function can be approximated in the far-field as

$$H_0^{(1)}(k_0 r)\simeq\sqrt{\frac{2}{\pi k_0 r}}e^{\mathrm{i}(k_0 r-\pi/4)}. \tag{A.3}$$

Substitution into Eq. (A.1) results in the elliptical wave equation

$$\frac{\partial^2 \Psi}{\partial r^2}+2ik_0\frac{\partial \Psi}{\partial r}+\frac{\partial^2 \Psi}{\partial z^2}+k_0^2(n^2-1)\Psi=0\,. \tag{A.4}$$

Eq. (A.1) can then be rewritten as

$$[L^2+2\mathrm{i}k_0 L+k_0^2(Q^2-1)]\Psi=0, \tag{A.5}$$

using the operators $L=\partial/\partial r$ and $Q=\sqrt{n^2+1/k_0^2(\partial^2/\partial z^2)}$. For a range independent environment Eq. (A.5) can then be factored into two components:

$$\frac{\partial \Psi}{\partial r} = -\mathrm{i}k_0(Q+1)\Psi \tag{A.6}$$

and

$$\frac{\partial \Psi}{\partial r} = \mathrm{i}k_0(Q-1)\Psi \,. \tag{A.7}$$

Equations (A.6) and (A.7) represent the incoming and outgoing waves, respectively. Neglecting the incoming portion, Eq. (A.7) can be solved using approximations to the square root operator, *Q*. Rewriting Q as $\sqrt{1+q}$ it can be shown that, for small propagation angles, q is small allowing for the expansion of the square root operator (e.g., into a Taylor series). This expansion around $q=0$ is equivalent to a paraxial approximation (i.e., a small angle approximation) from which the standard parabolic equation is formed. Approximations of the square root operator, *Q*, have led to many variations of the parabolic equation.

One approach to solving the parabolic equation is to use the Padé approximation of the form

$$Q \simeq \sum_{j=1}^{n} \frac{\alpha_{j,n} q}{1+\beta_{j,n} q} + 1 \,, \tag{A.8}$$

where n is the number of terms in the expansion and the coefficients are defined as

$$\alpha_{j,n} = \frac{2}{2n+1} \sin^2\left(\frac{j\pi}{2n+1}\right) \,, \tag{A.9}$$

and

$$\beta_{j,n} = \cos^2\left(\frac{j\pi}{2n+1}\right) \,. \tag{A.10}$$

Substituting Eq. (A.8) into Eq. (A.7) gives the very-wide-angle parabolic equation

$$\frac{\partial \Psi}{\partial r} = \mathrm{i}k_0 \left[\sum_{j=1}^{n} \frac{\alpha_{j,n}\left(n^2 - 1 + \frac{1}{k_0^2}\frac{\partial^2}{\partial z^2}\right)}{1+\beta_{j,n}\left(n^2 - 1 + \frac{1}{k_0^2}\frac{\partial^2}{\partial z^2}\right)} \right] \Psi. \tag{A.11}$$

Another approach, taken by Collins,[58] is to first solve Eq. (A.7) analytically at the range $r + \Delta r$ giving

$$\Psi(r + \Delta r) = e^{ik_0 \Delta r (Q-1)} \Psi(r). \tag{A.12}$$

Then applying the Padé approximation, Eq. (A.8), directly to the exponential in Eq. (A.12) the split-step Padé solution is obtained

$$\Psi(r + \Delta r) = \Psi(r) + \sum_{j=1}^{n} \frac{a_{j,n} q}{1 + b_{j,n} q} \Psi(r). \tag{A.13}$$

The coefficients $a_{j,n}$ and $b_{j,n}$ can be determined numerically. Collins uses this Padé solution to the parabolic equation in the Range-dependent Acoustic Model (RAM), the model adapted for use in this study, using a finite element method.[58]

THIS PAGE INTENTIONALLY LEFT BLANK

APPENDIX B: COMPARISON OF TWO DERIVATIVES OF THE RANGE-DEPENDENT ACOUSTIC MODEL (RAM): PE 5.5 AND MRAMGEO

The Range-Dependent Acoustic Model (RAM) is a propagation model that uses a split-step Padé solution, Eq. (A.13), to solve the parabolic wave equation. Several derivative programs of RAM are currently in use. The current U.S. Navy standard parabolic equation model (PE 5.5) incorporates RAM for range-dependent, passive acoustic propagation modeling. This version of RAM is capable of making predictions for a complex environment with fully range dependent parameters including bathymetry, sound-speed profiles and sediment properties.

RAMGEO is a modification to the basic RAM routine that allows the user to enter range dependent sediment properties underlying a range dependent bathymetry. A translation of this code from Fortran to MATLAB programming language resulted in MRAMGEO.[59] Although based on the same propagation algorithm, there are several differences between MRAMGEO and PE 5.5. The Navy standard model includes several features not available in MRAMGEO including a rough surface model based on wind speed, frequency dependent volume attenuation in the water column, and a directional source field to name the most significant. However, MRAMGEO has one distinct improvement over PE 5.5 in that the code is written in double precision number format, the default format in MATLAB programming; whereas, the Fortran version of RAM incorporated in PE 5.5 is written in single precision format.

During development of the two-way PE model used in this research a significant issue was encountered while attempting to benchmark the PE 5.5 program for some simple, direct path cases. These difficulties led to an analysis of the signal phase predicted by PE 5.5 for a range of propagation angles in a direct path environment (i.e., no boundary interactions). In the simulation presented here a 3 kHz source is placed 500 m depth in a constant sound-speed environment. The signal phase is analyzed at a fixed range of 250 m for varying propagation angles (±10°). Significant errors were discovered in the phase of the transmitted signal at even short ranges (Figure B.1). Increasing the

number of range steps, though initially leading to some improvement, eventually increased the error suggesting that the error is due to numerical precision of the model. A comparison with MRAMGEO, using identical input parameters (Table B.1) shows significant improvement for a wide range of propagation angles.

Parameter	**Value**
Source Properties	
Source Type	omnidirectional
Source Frequency (kHz)	3
Source Depth (m)	500
Receiver Properties	
Receiver Type	omnidirectional
Slant Range from Source (m)	250
Environmental Properties	
Depth (m)	1500
Sound-speed Profile (m/s)	1500 (constant)
Bottom Density (kg/m3)	1000
Bottom Sound Speed (m/s)	1500
Bottom Attenuation (dB/wavelength)	200
PE Settings	
range step - dr (m)	10
depth step - dz (m)	0.025
number of Padé terms	8

Table B.1 Model parameters for two-way PE 5.5 and MRAMGEO comparison.

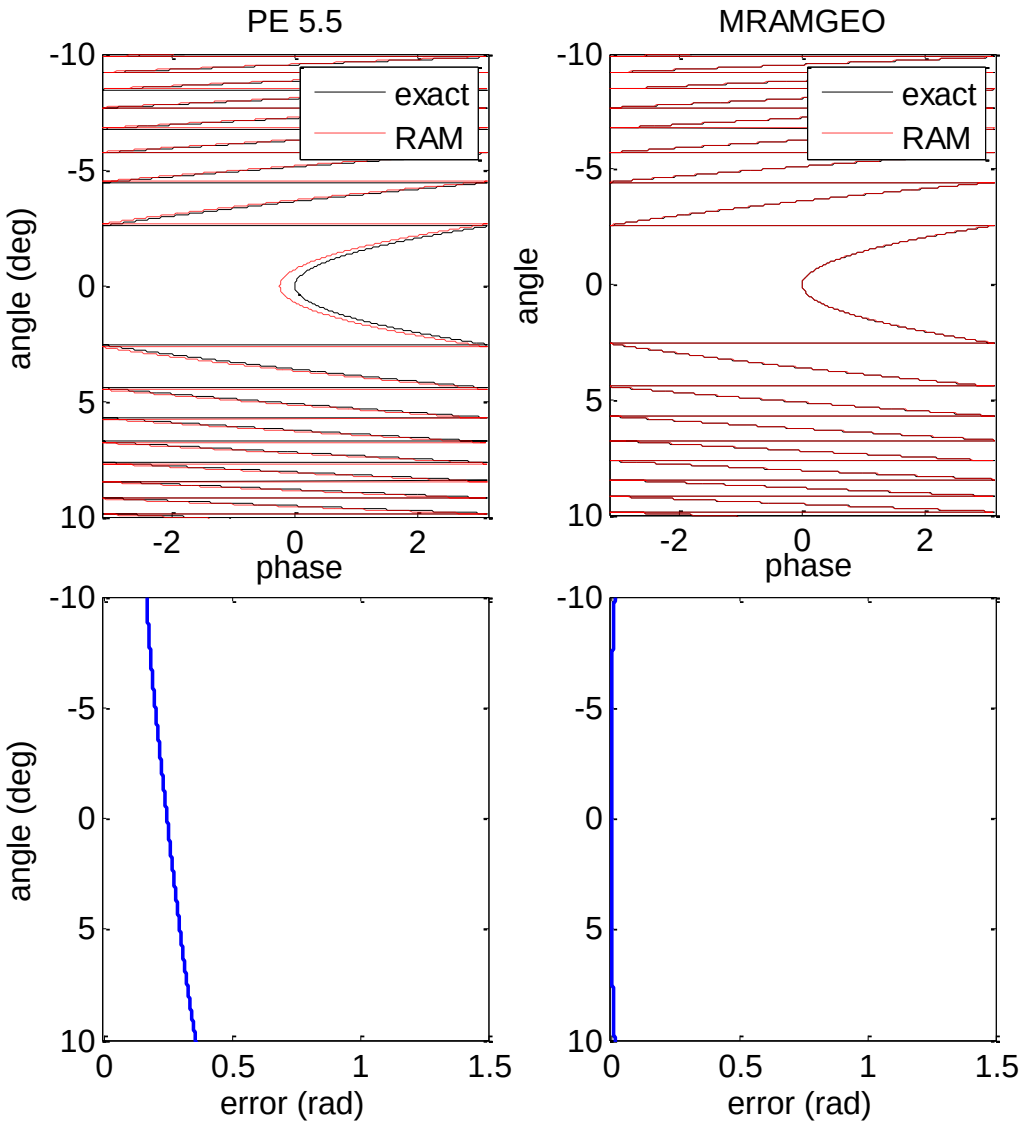

Figure B.1 Comparison between two implementations of RAM, PE 5.5 (left panels) and MRAMGEO (right panels). Predicted signal phase for a range of propagation angles is compared with the exact solution (top panels) with the error shown in the bottom panels. Simulation parameters are identical in both cases (Table B.1).

THIS PAGE INTENTIONALLY LEFT BLANK

APPENDIX C: BENCHMARKING THE TWO-WAY PARABOLIC EQUATION MODEL WITH LLOYD'S MIRROR PATTERN

The Lloyd's mirror pattern, a well-known geometric optics effect, has been applied widely as a benchmark for various ocean acoustics models.[86] This effect occurs in underwater acoustics when a source is placed near a smooth, perfectly reflecting surface. The pattern is a predictable modulation in the intensity of the received signal with depth which arises from the interference of the direct and surface reflected acoustic paths. Similar effects can be seen for both the one-way case (i.e., received intensity versus depth at some arbitrary range from a source) and for the two-way case (i.e., intensity versus depth predicted at the range of a source (r = 0 m) for a signal reflected by a scatterer located at some arbitrary range from the source).

In order to benchmark the two-way PE model used in this study comparisons are made with analytic expressions for the Lloyd's mirror pattern for the one-way and two-way cases. Assuming an acoustic wave of constant wavenumber, k, at a fixed time undergoing spherical spreading, the pressure can be expressed as

$$P = \frac{A}{r} e^{\mathrm{ikr}}. \tag{C.1}$$

For the one-way case with a source at depth, z_s, the intensity at some depth, z_r, and range, R_r, is given by

$$I_r^{\text{one-way}} = \frac{A^2}{r_1 r_2}\left[r_1^2 + r_2^2 - 2r_1 r_2 \cos\left(k\left(r_2 - r_1\right)\right)\right] \tag{C.2}$$

where the ray path lengths are

$$r_1 = \sqrt{(z_s - z_r)^2 + R_r^2} \text{ (direct path), and} \tag{C.3}$$

$$r_2 = \sqrt{(z_s + z_r)^2 + R_r^2} \text{ (surface-reflected path).} \tag{C.4}$$

For the two-way case with a scatterer located at a horizontal range, R_t, and depth, z_t, the intensity at the receiver is given by

$$I_r^{\text{two-way}} = P_a P_a^*, \tag{C.5}$$

where the asterisk denotes the complex conjugate and the acoustic pressure at the receiver is

$$P_a = A\left(\frac{e^{ikr_a}}{r_a} - \frac{e^{ikr_b}}{r_b}\right)\left(\frac{e^{ikr_c}}{r_c} - \frac{e^{ikr_d}}{r_d}\right). \quad \text{(C.6)}$$

The ray path lengths are as follows:

$$r_a = \sqrt{(z_s - z_t)^2 + R_t^2} \text{ (source-to-target direct path),} \quad \text{(C.7)}$$

$$r_b = \sqrt{(z_s + z_t)^2 + R_t^2} \text{ (source-to-target surface-reflected path),} \quad \text{(C.8)}$$

$$r_c = \sqrt{(z_t - z_r)^2 + R_t^2} \text{ (target-to-receiver direct path), and} \quad \text{(C.9)}$$

$$r_d = \sqrt{(z_t + z_r)^2 + R_t^2} \text{ (target-to-receiver surface-reflected path).} \quad \text{(C.10)}$$

In order to test the accuracy of the two-way PE model, predictions were made of the transmission loss pattern for an active system with a receiver co-located in range with a source. Both the source and scatterer were located near the surface inducing a Lloyd's mirror effect. A fluid half-space (i.e., bottomless) environment was simulated in the PE model with a deep, penetrable, and strongly absorbing bottom (Table C.1). The predicted intensity pattern at the receiver matched theory nearly exactly (Figure C.1).

Parameter	Value
Source Properties	
Source Type	omnidirectional
Source Frequency (kHz)	3
Source Depth (m)	25
Receiver Properties	
Receiver Type	omnidirectional
Receiver Depth(m)	0–100
Scatterer Properties	
Number of Scatterers	1
Horizontal Range from Source (m)	750
Frequency Response	1
Environmental Properties	
Depth (m)	1500
Sound-speed Profile (m/s)	1500 (constant)
Bottom Density (kg/m3)	1000
Bottom Sound Speed (m/s)	1500
Bottom Attenuation (dB/wavelength)	200
PE Settings	
range step - dr (m)	0.5
depth step - dz (m)	0.025
number of Padé terms	8

Table C.1 Model parameters for two-way parabolic equation simulation of Lloyd's mirror effect.

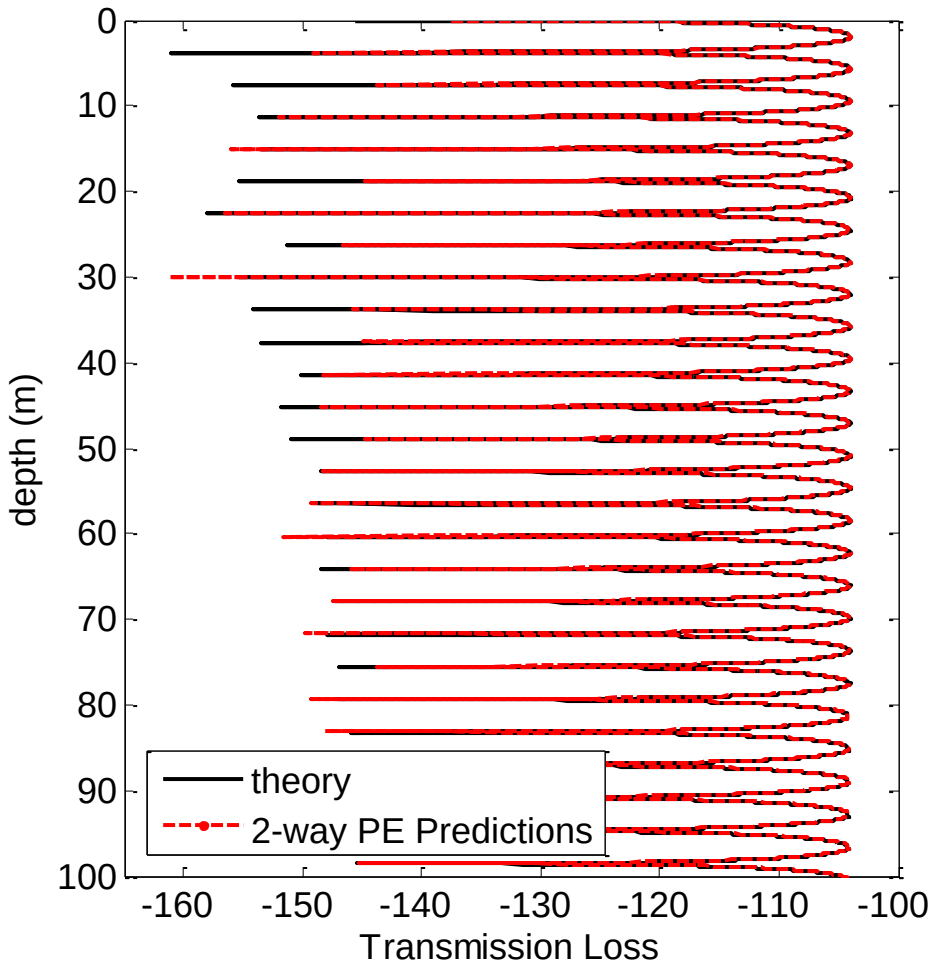

Figure C.1 Two-way PE predictions of Lloyd's mirror effect for a vertical receiver co-located in range with an omnidirectional source (red) compared with theory (black).

APPENDIX D: GENERATION AND STATISTICAL ANALYSIS OF PROBABILITY DENSITY FUNCTIONS OF ECHO ENVELOPES

Probability density functions were generated for two distinct ensembles: the envelopes (i.e., the magnitude) of the pressure field at a fixed range and random depth and the envelopes of the echoes from one or more scatterers located at a fixed range and randomly located in depth. The ensembles are generated by Monte Carlo method with an ensemble size of at least 1000 instances in all cases which was shown to produce good results for the two-way PE model in validation against theory (see Sec II.C.4). PDFs were generated from histograms of envelopes normalized by the root mean square (rms) echo amplitude of the ensemble. A subtle consequence of this is that the single-parameter Rayleigh distribution, with a parameter that is directly related to the rms value, will have a fixed probability distribution when normalized. In contrast the exponential distribution, which has a single parameter representing the mean of the distribution, will vary from normalization to normalization.

Two statistical methods were used in this paper to compare probability density functions, the Lilliefors test and the Kullback-Leibler distance. The Lilliefors test is a goodness-of-fit test used to determine if a given distribution comes from a specific distribution in the normal family.[87,88] The two primary distributions of interest in this study are the Rayleigh distribution and the exponential distribution. The Lilliefors test is used to test goodness-of-fit for the exponential distribution directly. For the Rayleigh distribution, which arises when the modulus is taken of a zero-mean Gaussian random variable, the Lilliefors test is applied independently to the real and imaginary parts of the complex pressure before taking the envelope. These results are presented as *p*-values for both the real and imaginary parts of the complex random variable (e.g., $p_{\text{real}}/p_{\text{imag.}}$ = 0.8/0.9) represents the *p*-value of 0.8 for the real portion and 0.9 for the imaginary portion for the goodness-of-fit to a Gaussian distribution. In this case the high *p* values would indicate that the distribution is Rayleigh distributed.

The Kullback-Leibler distance provides a statistical measure of the difference between two distributions.[89] This measure is given as

$$d_{\mathrm{KL}} = \sum_i \mathrm{p}_1(x_i) \log\left[\frac{\mathrm{p}_1(x_i)}{\mathrm{p}_2(x_i)}\right], \tag{D.1}$$

where the probabilities $\mathrm{p}_1(\cdot)$ and $\mathrm{p}_2(\cdot)$ can represent either a model prediction and a theoretical distribution or two model predictions. This measure emphasizes the mismatch between the high amplitude low probability tails of the distributions.[20]

APPENDIX E: SCATTERING MODEL FOR AGGREGATIONS OF FISH

Overview

A scattering model has been developed for use with a propagation algorithm to simulate volume reverberation by aggregations of fish in a waveguide. The primary goals in development of this model are to produce a computationally efficient, physics-based model, that accurately predicts the statistical nature of echoes from fish when ensonified by a mid-frequency, directional sonar beam. First-order effects included are depth-dependent resonant swimbladder frequency response and realistic aggregation morphology. Multiple scattering and collective resonance are neglected due to the large size and relatively low densities of fish aggregations considered in this study.[17,40] Doppler effects due to relative fish motion, a small effect for these frequencies and fish motion[21], are also neglected here.

In general the scattering model is a free-field model (i.e., no waveguide or boundary effects are included in the scattering model itself) that reduces a very large number of fish to a smaller number of monopole scattering centers assembled in a geometry that represents a realistic fish aggregation. The volume scattering strength of the aggregation is calculated from the depth-dependent frequency response predicted by the resonant scattering model (See Appendix F). This model can be excited by any propagation model which produces the complex pressure field for a three-dimensional (3D) environment. This can include either a true 3D propagation model or by N-azimuths of a two-dimensional propagation (N-by-2D) model.

Scattering Center Methodology

The approach taken here is to model a large aggregation of fish, which might include hundreds or thousands of individual fish, with a collection of scattering centers to improve computational efficiency. In the mid-frequency regime (1–9 kHz) swimbladder-bearing fish of a wide range of sizes can be modeled as isotropic scatterers because the scattering response is dominated by the 0th mode scattering (i.e., the volume resonance or

"breathing mode") of their swimbladder. Taking advantage of this characteristic, an actual spatial distribution of fish can be reduced to a much smaller number of scattering centers. The scattering centers are treated as omnidirectional (monopole) scatterers with a depth-dependent, resonant frequency response. The scattering centers, each with a delta-function distributed scattering response, are randomly distributed with a uniform density within an arbitrary external geometry.

According to the central limit theorem, the sum of contributions from many independent scatterers with random phase results in a zero-mean complex Gaussian signal and thus the magnitude, or envelope, of the signal is Rayleigh distributed. Therefore, in the case of scattering by a large aggregation of fish in the regime where the sonar resolution cell is much smaller than the aggregation but large enough to contain many unresolved fish, it is expected that the echo envelopes are Rayleigh distributed. Knowledge of this property facilitates the reduction in the density of scatterers from that of a realistic fish school to a lower density of scattering centers with an aggregate response that is still Rayleigh-distributed. A numerical simulation was conducted with a directional sonar system (an omnidirectional source and a 32-element horizontal line array receiver) in a direct path environment using a source signal with a center frequency of 3 kHz and a bandwidth of 100 Hz. It was determined, using Kullback-Leibler distance, d_{KL}, for error estimation, that when the number of scattering centers per resolution cell, N_{r}, exceeded 5 the statistics approached a Rayleigh distribution (Figure E.1).

The scattering center approach readily lends itself to an arbitrary shape for the aggregation of scatterers. Once an external morphology is determined, scatterers are randomly distributed with a uniform spatial density within the external boundary. Scattering center density, ρ_{sc}, in scattering centers per m^3 is determined as

$$\rho_{\mathrm{sc}} = \frac{N_{\mathrm{r}}}{V_{\mathrm{src}}}, \tag{E.1}$$

where N_{r} is empirically determined (see above) and the volume of a sonar resolution cell is approximated by the on axis, half-power resolution cell size in a direct path geometry

$$V_{\text{src}} = |\mathbf{r}|^2 \theta_{3\text{dB}} \phi_{3\text{dB}} r_{\text{res}}. \quad \text{(E.2)}$$

The position vector, $\mathbf{r}$, denotes the center of the fish aggregation from the source-receiver couplet in m, $\theta_{3\text{dB}}$ and $\phi_{3\text{dB}}$ are the 3 dB beamwidths in azimuth and elevation of the sonar system, and r_{res} is the range resolution in m determined by the waveform. It is assumed that $r_{res} \ll |\mathbf{r}|$.

Observations of Atlantic Herring measured acoustically using a 400 kHz multi-beam echosounder data[19] are shown to illustrate this method (Figure E.2). Multi-beam data consisting of latitude, longitude, depth coordinates and uncalibrated backscattering amplitude were converted to a uniform x-y-z grid and decimated to the required scattering density. A random 3D vector was then added to the position of each scattering center to prevent artifacts of Bragg diffraction from an artificially-latticed distribution of scatterers.

Frequency Response

The active sonar equation for volume reverberation level, RL_V, in decibels (dB) relative to a reference intensity, $I_0 = 0.67 \times 10^{-18}$ in units of watts per square meter (W/m^2) is given as

$$\text{RL}_V = \text{SL} - 2\text{TL} + \langle S_V \rangle + 10 \log(V_{\text{e}}), \quad \text{(E.3)}$$

where SL, source level, and TL, transmission loss, are both given in dB *re* 1 micropascal (μPa) at 1 m^1. The effective reverberating volume, V_{e}, is dependent on the range between the sonar and the source of reverberation, the range resolution based on the parameters of the waveform, and the beampattern. Finally, the volume scattering strength, $\langle S_V \rangle$, is an ensemble average of the scattering strength of the scatterers causing the reverberation. Importantly, this equation is valid at a single frequency as *SL* and the beampattern (and thus V_{e}) can be dependent on frequency.

In order to apply a frequency response to each scattering center, the last two terms in Eq. (E.3) are considered. The effective volume of a single scattering center is given as[1]

$$V_e = \int_V B_T(f;\theta,\phi) B_R(f;\theta,\phi) dV\,, \tag{E.4}$$

where B_T and B_R are the frequency, f, azimuth, θ, and elevation, ϕ, dependent transmit and receive beampatterns in intensity. This effective volume, for the case where the reverberation volume is small compared to the sonar resolution cell, can be approximated by the product of the volume of a given scattering center, V, and a single beampattern value

$$V_e \approx VB'(f;\theta_0,\phi_0)\,, \tag{E.5}$$

where B' is the combined transmit and receive beampattern value, in intensity, at the location of the scattering center, ϕ_0, θ_0. Substituting Eq. (E.5), for the effective volume, and Eq. (F.2), describing the volume scattering strength for an aggregation of scatterers, into Eq. (E.3) gives the reverberation level for a given scattering center

$$RL_V = SL - 2TL + 10\log(\rho_s \bar{\sigma}_{bs}) + 10\log(V) + 10\log B'(f;\theta_0,\phi_0). \tag{E.6}$$

A frequency response, termed effective backscattering amplitude and given in m, can then be formed by taking the square root of the antilog of the last two terms of Eq. (E.6)

$$\left| f_{bs}^{eff}(f) \right| = \sqrt{\rho_s \bar{\sigma}_{bs}(f) V} \tag{E.7}$$

where ρ_s is the numerical density of the scatterers (in this case fish) in scatterers per m^3 and $\bar{\sigma}_{bs}$ is the ensemble average backscattering cross section in m^2. It should be noted that $\left| f_{bs}^{eff}(f) \right|$ is an ensemble average value and, as indicated, is a real quantity containing no phase information.

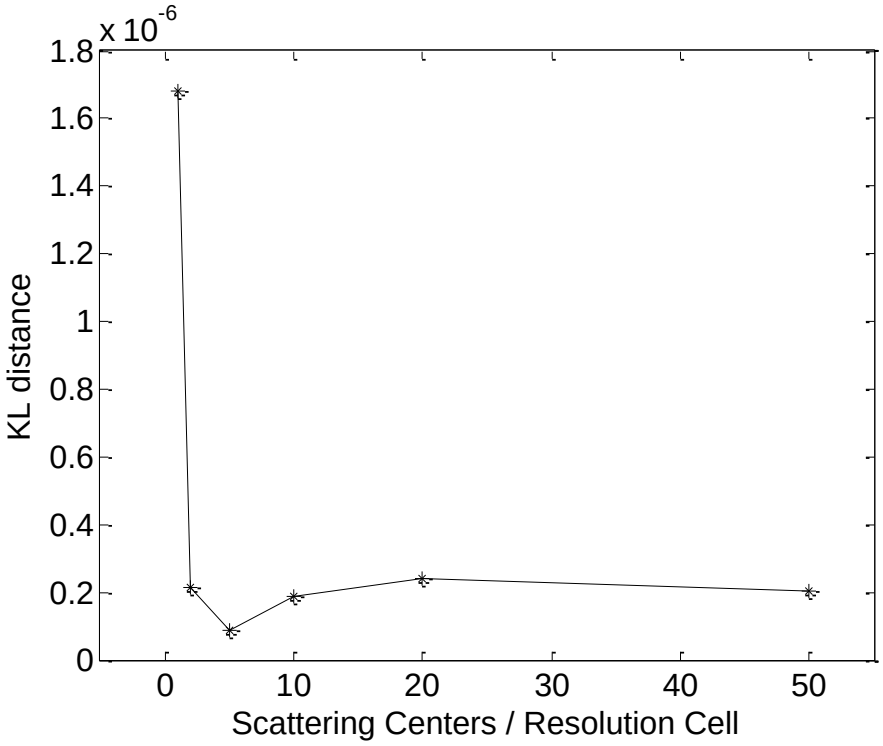

Figure E.1 Kullback-Leibler distances comparing a Rayleigh PDF with normalized echo envelope PDFs from numerical simulations, where the number of scatterers within a sonar resolution cell is varied from 1 to 50.

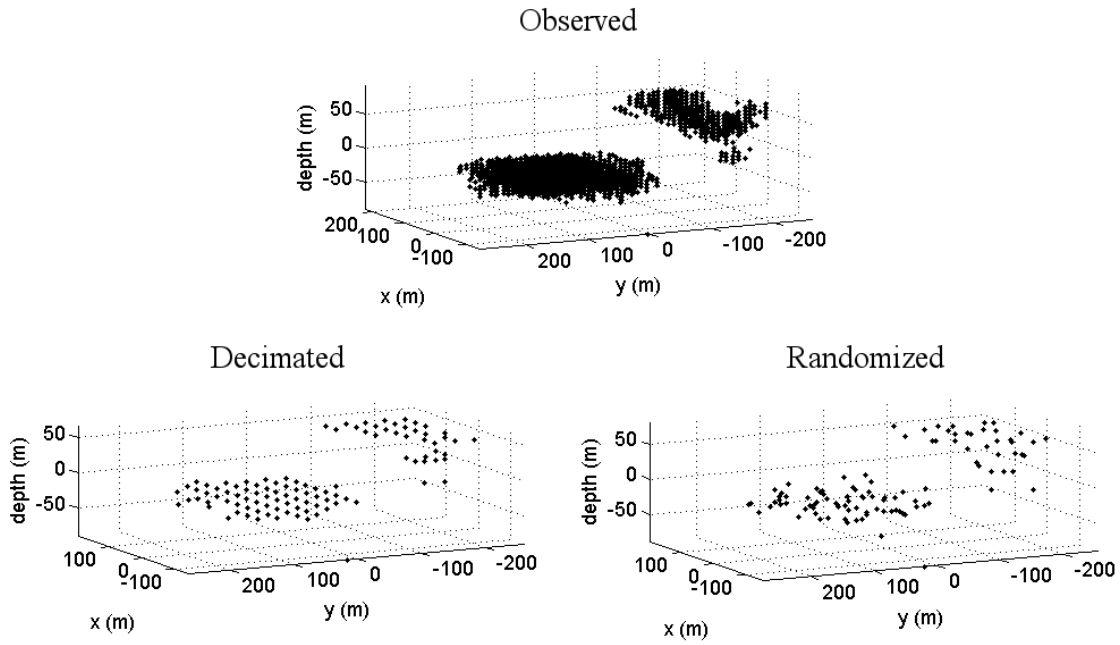

Figure E.2 Mapping observed morphology to scattering centers.

APPENDIX F: ACOUSTIC SCATTERING BY GAS-FILLED-SWIMBLADDER BEARING FISH

Target strength, TS, is the logarithmic measure of a backscattered signal in dB relative to square meters (dB re 1 m^2) and can be expressed as

$$TS = 10\log_{10}(\sigma_{\mathrm{bs}}), \tag{F.1}$$

where $\sigma_{\mathrm{bs}} = |f_{\mathrm{bs}}|^2$ is the differential backscattering cross section in m^2 and f_{bs} is the backscattering amplitude in m. The average volume scattering strength of an aggregation of scatterers with an average differential backscattering cross section of $\bar{\sigma}_{bs}$ and a numerical density in scatterers per m^3, ρ_{S}, then is given in dB relative to m^{-1} (dB re 1 m^{-1}) as

$$\langle S_V \rangle = 10\log_{10}(\rho_{\mathrm{S}}\bar{\sigma}_{\mathrm{bs}}). \tag{F.2}$$

At mid-frequencies (1–9 kHz) a resonance model for acoustic scattering by a fish swimbladder is appropriate for fish with swimbladders of a length similar to the acoustic wavelength (i.e., on the order of 0.1 to 1 m). The Love model[16] is an empirically validated scattering model[24,90] that represents the swimbladder as an gas-filled, viscous, spherical shell. The model, as given by Nero et al. in a simplified form,[90] neglects two terms, thermal damping and swimbladder-wall tension. These terms have been shown by Love to be insignificant. The differential backscattering cross-section is given as

$$\sigma_{bs}(z,\mathrm{f}) = \frac{r_{\mathrm{eq}}(z)^2}{\left(\frac{\mathrm{f}_0(z)}{\mathrm{f}H(\mathrm{f})}\right)^2 + \left[\left(\frac{\mathrm{f}_0(z)}{\mathrm{f}}\right)^2 - 1\right]^2}, \tag{F.3}$$

where $r_{\mathrm{eq}}(z)$ and $\mathrm{f}_0(z)$ are the equivalent spherical radius and the resonance frequency of the swimbladder at depth z. For a fish of length L, in m, the swimbladder volume at the surface, V_0, in m^3 is determined by regression of the fish length as

$$V_0 = A(100L)^{3.35} \times 10^{-6}, \tag{F.4}$$

where A is a species-specific parameter. There are two major classes of gas-filled-swimbladder bearing fish. Physoclists (e.g., silver hake and Acadian redfish) maintain a

constant volume of their swimbladder through gaseous exchange with their bloodstream; whereas, physostomes (e.g., Atlantic herring) are required to take in air above the surface. In the latter case the volume of the swimbladder is subject to a change approximately following Boyle's Law when encountering a change in pressure with depth. The variation of the equivalent spherical radius of the swimbladder, $r_{\mathrm{eq}}(\mathrm{z})$, with depth is thus

$$r_{\mathrm{eq}}(\mathrm{z}) = \begin{cases} r_0 & \text{physoclist} \\ r_0\left(P_0 / P(z)\right)^{1/3} & \text{physostome} \end{cases}, \tag{F.5}$$

where, r_0 is the radius of a sphere of volume V_0, P_0 is the ambient pressure in Pascals (Pa) at the surface, and P is the ambient pressure in Pa at depth z.

The resonance frequency, which is strongly dependent upon the size of the swimbladder and the depth of the fish is given as

$$\mathrm{f}_0(z) = \zeta(z)\sqrt{\frac{3\gamma_\alpha P(z)}{4\pi^2 r_{\mathrm{eq}}^2(z)\rho_{\mathrm{f}}}}. \tag{F.6}$$

where $\gamma_\alpha = 1.4$ is the ratio of specific heats of air at constant pressure and constant volume, $\rho_{\mathrm{f}} = 1050$ kg·m^3 is the density of fish flesh.[16] Combining Eq. (F.5) and Eq. (F.6) it is seen that the pressure dependency of the resonance frequency (and similarly the dependence on depth) is proportional to $P^{1/2}$ for physoclists and $P^{5/6}$ for physostomes. The term ζ is a depth-dependent correction factor for the non-spherical shape of a swimbladder. This term is published with a typographical error in Nero et al., but given correctly by Love as

$$\zeta(z) = \frac{\sqrt{2}\left[1-\epsilon^2(z)\right]^{1/4}}{\epsilon^{1/3}(z)}\left[\ln\left(\frac{1+\sqrt{1-\epsilon^2(z)}}{1-(\sqrt{1-\epsilon^2(z)}}\right)\right]^{-1/2} \tag{F.7}$$

where, ϵ is the ratio of minor to major axes of a prolate spheroid with the equivalent spherical volume, $V(z) = (4/3)\pi r_{\mathrm{eq}}^3(z)$. Following Ona[80] and Nero et al[90] this ratio is determined using a fixed end position of the swimbladder (i.e., constant length of the major axis) and pressure sensitive diameter, (i.e., pressure dependent length of the minor axis) where the length of the swimbladder is taken to be one third the total fish length[90] so that

$$\epsilon = \left(\frac{3V(z)}{4\pi}\right)^{1/2}\left(\frac{L}{6}\right)^{-3/2}. \qquad \text{(F.8)}$$

The term H in Eq. (F.3) is the damping factor given by

$$H(z,f) = \left(\frac{2\pi r_{eq}(z)f^2}{cf_0(z)} + \frac{\xi}{\pi r_{eq}^2(z)f_0\rho_F}\right)^{-1}, \qquad \text{(F.9)}$$

where c = 1500 m/s is a constant sound speed and ξ is the viscosity of fish flesh in Pascal-seconds (Pa·s).

THIS PAGE INTENTIONALLY LEFT BLANK

LIST OF REFERENCES

[1]R. J. Urick, *Principles of Underwater Sound*, 3rd ed. (McGraw-Hill, New York, 1983).

[2]J. M. Fialkowski and R. C. Gauss, "Methods for identifying and controlling sonar clutter," IEEE J. Ocean. Eng. **35** (2), 330–354 (2010).

[3]O. R. Smith, "The location of sardine schools by super-sonic echo-ranging," Comm. Fish. Rev. **9** (1), 1–6 (1947).

[4]P. F. Smith, "Further measurements of the sound scattering properties of several forms of marine life," Deep-Sea Res. **2**, 71–79 (1954).

[5]D. E. Weston, "Fish as a possible cause of low-frequency acoustic attenuation in deep water," J. Acoust. Soc. Am. **40** (6), 1558 (1966).

[6]D. E. Weston and J. Revie, "Fish echoes on a long-range sonar display," J. Sound Vib. **17** (1), 105–112 (1971).

[7]J. S. M. Rusby, *et al.*, "Experimental survey of a herring fishery by long-range sonar," Mar. Biol. **22** (3), 271–292 (1973).

[8]J. B. Hersey and R. H. Backus, "New evidence that migrating gas bubbles, probably the swimbladders of fish, are largely responsible for scattering layers on the continental rise south of New England," Deep-Sea Res. **1** (3), 190–191 (1954).

[9]J. B. Hersey, R. H. Backus and J. Hellwig, "Sound-scattering spectra of deep scattering layers in the western North Atlantic Ocean," Deep-Sea Res. **8**, 196–210 (1962).

[10]J. R. Marshall and R. P. Chapman, "Reverberation from deep scattering layer measured with explosive sound sources," J. Acoust. Soc. Am. **36** (1), 164–167 (1964).

[11]O. Sand and A. D. Hawkins, "Acoustic properties of cod swimbladder," J. Exp. Biol. **58** (3), 797–820 (1973).

[12]J. R. Marshall and R. P. Chapman, "Reverberation from a deep scattering layer measured with explosive sound sources," J. Acoust. Soc. Am. **36** (1), 164–167 (1964).

[13]C. H. Thompson and R. H. Love, "Determination of fish size distributions and areal densities using broadband low-frequency measurements," ICES J. Mar. Sci. **53** (2), 197–201 (1996).

[14]R. W. Nero, C. H. Thompson and R. H. Love, "Low-frequency acoustic measurements of Pacific hake, *Merluccius productus*, off the west coast of the United States," Fish. Bull. **96** (2), 329–343 (1998).

[15]I. B. Andreeva, "Scattering of sound by air bladders of fish in deep sound-scattering ocean layers," Sov. Phy. Acoust. **10** (1), 17–20 (1964).

[16]R. H. Love, "Resonant acoustic scattering by swimbladder-bearing fish," J. Acoust. Soc. Am. **64** (2), 571–580 (1978).

[17]T. K. Stanton, C. J. Sellers and J. M. Jech, "Resonance classification of mixed assemblages of fish with swimbladders using a modified commercial broadband acoustic echosounder at 1–6 kHz," Can. J. Fish. Aquat. Sci. **69**, 854–868 (2012).

[18]F. Gerlotto and J. Paramo, "The three-dimensional morphology and internal structure of clupeid schools as observed using vertical scanning multibeam sonar," Aquat. Living Resour. **16** (3), 113–122 (2003).

[19]T. C. Weber, H. Pena and J. M. Jech, "Consecutive acoustic observations of an Atlantic herring school in the Northwest Atlantic," ICES J. Mar. Sci. **66** (6), 1270–1277 (2009).

[20]T. K. Stanton and D. Chu, "Non-Rayleigh echoes from resolved individuals and patches of resonant fish at 2–4 kHz," IEEE J. Ocean. Eng. **35** (2), 152–163 (2010).

[21]D. V. Holliday, "Doppler structure in echoes from schools of pelagic fish," J. Acoust. Soc. Am. **55** (6), 1313–1322 (1974).

[22]O. Diachok, "Effects of absorptivity due to fish on transmission loss in shallow water," J. Acoust. Soc. Am. **105** (4), 2107–2128 (1999).

[23]D. V. Holliday, "Resonance structure in echoes from schooled pelagic fish," J. Acoust. Soc. Am. **51** (4), 1322–1332 (1972).

[24]T. K. Stanton, *et al.*, "New broadband methods for resonance classification and high-resolution imagery of fish with swimbladders using a modified commercial broadband echosounder," ICES J. Mar. Sci. **67** (2), 365–378 (2010).

[25]D. A. Abraham, "The effect of multipath on the envelope statistics of bottom clutter," IEEE J. Ocean. Eng. **32** (4), 848–861 (2007).

[26]P. Ratilal, *et al.*, "Long range acoustic imaging of the continental shelf environment: The Acoustic Clutter Reconnaissance Experiment 2001," J. Acoust. Soc. Am. **117** (4), 1977–1998 (2005).

[27]J. M. Gelb, R. E. Heath and G. L. Tipple, "Characterization of clutter by class in mid-frequency active sonar," Proceedings of the International Symposium on Underwater Reverberation and Clutter, 303–310 (2008).

[28]J. M. Gelb, R. E. Heath and G. L. Tipple, "Statistics of distinct clutter classes in midfrequency active sonar," IEEE J. Ocean. Eng. **35** (2), 220–229 (2010).

[29]D. Chu and T. K. Stanton, "Statistics of echoes from a directional sonar beam insonifying finite numbers of single scatterers and patches of scatterers," IEEE J. Ocean. Eng. **35** (2), 267–277 (2010).

[30]Y. A. Kravtsov, V. M. Kuz'kin and V. G. Petnikov, "Wave diffraction by regular scatterers in multimode waveguides," Sov. Phy. Acoust. **30** (3), 199–202 (1984).

[31]F. Ingenito, "Scattering from an object in a stratified medium," J. Acoust. Soc. Am. **82** (6), 2051–2059 (1987).

[32]N. C. Makris and P. Ratilal, "A unified model for reverberation and submerged object scattering in a stratified ocean waveguide," J. Acoust. Soc. Am. **109** (3), 909–941 (2001).

[33]R. H. Hackman and G. S. Sammelmann, "Acoustic scattering in an inhomogeneous wave-guide - theory," J. Acoust. Soc. Am. **80** (5), 1447–1458 (1986).

[34]R. H. Hackman and G. S. Sammelmann, "Long-range scattering in a deep oceanic wave-guide," J. Acoust. Soc. Am. **83** (5), 1776–1793 (1988).

[35]M. D. Collins and M. F. Werby, "A parabolic equation model for scattering in the ocean," J. Acoust. Soc. Am. **85** (5), 1895–1902 (1989).

[36]E. T. Kusel and P. Ratilal, "Effects of incident field refraction on scattered field from vertically extended cylindrical targets in range-dependent ocean waveguides," J. Acoust. Soc. Am. **125** (4), 1930–1936 (2009).

[37]P. Ratilal and N. C. Makris, "Range-dependent reverberation modeling with the parabolic equation," J. Acoust. Soc. Am. **114** (4), 2302 (2003).

[38]P. Ratilal, *et al.*, "Range-dependent 3D scattering and reverberation in the continental shelf environment from biology, geology and oceanography," J. Acoust. Soc. Am. **117** (4), 2611 (2005).

[39]M. Andrews, *et al.*, "Assessing fish populations and enhancing biological detection in continental shelf environments with range-dependent scattering and reverberation models," J. Acoust. Soc. Am. **118** (5), 3436 (2006).

[40]M. Andrews, Z. Gong and P. Ratilal, "Effects of multiple scattering, attenuation and dispersion in waveguide sensing of fish," J. Acoust. Soc. Am. **130** (3), 1253–1271 (2011).

[41]D. A. Abraham and C. W. Holland, "Spatially compact clutter," Proceedings of 2008 International Symposium on Underwater Reverberation and Clutter, 247–254 (2008).

[42]E. Jakeman and P. N. Pusey, "A model for non-Rayleigh sea echo," IEEE Transactions on Antennas and Propagation **24** (6), 806–814 (1976).

[43]E. Jakeman and P. N. Pusey, "Significance of K-distributions in scattering experiments," Phys Rev Lett **40** (9), 546–550 (1978).

[44]B. R. La Cour and J. E. Hamann, "Dynamic modeling of discrete biologics for active sonar simulation," IEEE J. Ocean. Eng. **35** (2), 164–174 (2010).

[45]R. C. Gauss, *et al.*, "Broadband models for predicting bistatic bottom, surface, and volume scattering strengths," JUA **51**, 785–826 (2001).

[46]K. D. LePage, "Statistics of broad-band bottom reverberation predictions in shallow-water waveguides," IEEE J. Ocean. Eng. **29** (2), 330–346 (2004).

[47]D. A. Abraham and A. P. Lyons, "Reverberation envelope statistics and their dependence on sonar bandwidth and scattering patch size," IEEE J. Ocean. Eng. **29** (1), 126–137 (2004).

[48]J. A. Fialkowski, R. C. Gauss and D. M. Drumheller, "Measurements and modeling of low-frequency near-surface scattering statistics," IEEE J. Ocean. Eng. **29** (2), 197–214 (2004).

[49]T. K. Stanton, *et al.*, "Physics-based interpretation of echo statistics of three distinct clutter classes measured with a midfreqency active sonar," (in manuscript).

[50]J. K. Horne, "Acoustic approaches to remote species identification: A review," Fisheries Oceanography **9** (4), 356–371 (2000).

[51]J. W. Goodman, *Statistical Optics* (John Wiley and Sons, New York, 1985).

[52]B. F. Cron and W. R. Schumacher, "Theoretical and experimental study of underwater sound reverberation," J. Acoust. Soc. Am. **33** (7), 881–888 (1961).

[53]D. A. Abraham and A. P. Lyons, "Guest editorial: Non-Rayleigh reverberation and clutter," IEEE J. Ocean. Eng. **29** (2), 193–196 (2004).

[54]J. A. Colosi and A. B. Baggeroer, "On the kinematics of broadband multipath scintillation and the approach to saturation," J. Acoust. Soc. Am. **116** (6), 3515–3522 (2004).

[55]J. E. Ehrenberg, "A method for extracting the fish target strength distribution from acoustic echoes," Proceedings of the International Conference on Engineering in the Ocean Environment, Ocean 72, 61–64 (1972).

[56]J. E. Ehrenberg, *et al.*, "Indirect measurement of the mean acoustic backscattering cross-section of fish," J. Acoust. Soc. Am. **69** (4), 955–962 (1981).

[57]R. Barakat, "First-order statistics of combined random sinusoidal waves with applications to laser speckle patterns," Optica Acta **21** (11), 903–921 (1974).

[58]M. D. Collins, "A split-step Padé solution for the parabolic equation method," J. Acoust. Soc. Am. **93** (4), 1736–1742 (1993).

[59]J. Fabre, (private communication).

[60]R. R. Greene, "The rational approximation to the acoustic-wave equation with bottom interaction," J. Acoust. Soc. Am. **76** (6), 1764–1773 (1984).

[61]C. Garrett and W. Munk, "Space-time scales of internal waves - progress report," Journal of Geophysical Research **80** (3), 291–297 (1975).

[62]C. Garrett and W. Munk, "Space-times scales of internal waves," Geophysical Fluid Dynamics **3** (1), 225–264 (1972).

[63]J. A. Colosi, *et al.*, "Observations of sound-speed fluctuations on the New Jersey continental shelf in the summer of 2006," J. Acoust. Soc. Am. **131** (2), 1733–1748 (2012).

[64]W. H. Munk, "Sound channel in an exponentially stratified ocean, with application to sofar," J. Acoust. Soc. Am. **55** (2), 220–226 (1974).

[65]J. A. Colosi and M. G. Brown, "Efficient numerical stimulation of stochastic internal-wave-induced sound-speed perturbation fields," J. Acoust. Soc. Am. **103** (4), 2232–2235 (1998).

[66]J. A. Colosi, T. F. Duda and A. K. Morozov, "Statistics of low-frequency normal-mode amplitudes in an ocean with random sound-speed perturbations: Shallow-water environments," J. Acoust. Soc. Am. **131** (2), 1749–1761 (2012).

[67]M. F. Arndt, "A method for generating uniform point distributions when the volume integral of a sample has constant integration limits in some curvilinear coordinate system," Nucl Instrum Meth A **580** (3), 1474–1477 (2007).

[68]T. K. Stanton and C. S. Clay, "Sonar echo statistics as a remote-sensing tool - volume and sea-floor," IEEE J. Ocean. Eng. **11** (1), 79–96 (1986).

[69]I. Dyer, "Statistics of sound propagation in ocean," J. Acoust. Soc. Am. **48** (1), 337–345 (1970).

[70]D. A. Abraham and A. P. Lyons, "Reliable methods for estimating the K-distribution shape parameter," IEEE J. Ocean. Eng. **35** (2), 288–302 (2010).

[71]D. A. Abraham and A. P. Lyons, "Novel physical interpretations of K-distributed reverberation," IEEE J. Ocean. Eng. **27** (4), 800–813 (2002).

[72]D. E. Weston and H. W. Andrews, "Seasonal sonar observations of the diurnal shoaling times of fish," J. Acoust. Soc. Am. **87** (2), 673–680 (1990).

[73]D. M. Farmer, M. V. Trevorrow and B. Pedersen, "Intermediate range fish detection with a 12-kHz sidescan sonar," J. Acoust. Soc. Am. **106** (5), 2481–2490 (1999).

[74]N. C. Makris, *et al.*, "Fish population and behavior revealed by instantaneous continental shelf-scale imaging," Science **311** (5761), 660–663 (2006).

[75]Z. Gong, *et al.*, "Low-frequency target strength and abundance of shoaling Atlantic herring (Clupea harengus) in the Gulf of Maine during the Ocean Acoustic Waveguide Remote Sensing 2006 Experiment," J. Acoust. Soc. Am. **127** (1), 104–123 (2010).

[76]J. M. Jech and F. Stroman, "Aggregative patterns of pre-spawning Atlantic herring on Georges Bank from 1999–2010," Aquat. Living Resour. **25**, 1–14 (2012).

[77]R. P. Goddard, "Simulating ocean reverberation: A review of methods and issues," APL-UW TR 9313 (1993).

[78]R. P. Goddard, "The sonar simulation toolset," Proceedings of OCEANS '89 **4**, 1217–1222 (1989).

[79]R. E. Keenan, "An introduction to GRAB eigenrays and CASS reverberation and signal," OCEANS 2000 MTS/IEEE Conference and Exhibition **2**, 1070 (2000).

[80]E. Ona, "An expanded target-strength relationship for herring," ICES J. Mar. Sci. **60** (3), 493–499 (2003).

[81]W. J. Overholtz, *et al.*, "Empirical comparisons of survey designs in acoustic surveys of Gulf of Maine-Georges Bank Atlantic herring," J Northwest Atl Fish Sci **36**, 127–144 (2006).

[82]J. M. Jech, (private communication).

[83]NOAA National Geophysical Data Center, *U.S. Coastal Relief Model*, http://www.ngdc.noaa.gov/mgg/coastal/crm.html.

[84]U.S. Geological Survey, *U.S. Geological Survey East Coast Sediment Texture Database*, (**2011)**, http://woodshole.er.usgs.gov/.

[85]K. L. Williams and D. R. Jackson, "Bistatic bottom scattering: Model, experiments, and model/data comparison," J. Acoust. Soc. Am. **103** (1), 169–181 (1998).

[86]F. B. Jensen, *et al.*, *Computational Ocean Acoustics* (Springer-Verlag, New York, 2000).

[87]H. W. Lilliefors, "On Kolmogorov-Smirnov test for exponential distribution with mean unknown," J. Am. Stat. Assoc. **64** (325), 387–389 (1969).

[88]H. W. Lilliefors, "On Kolmogorov-Smirnov test for normality with mean and variance unknown," J. Am. Stat. Assoc. **62** (318), 399–402 (1967).

[89]S. Kullback and R. A. Leibler, "On information and sufficiency," Annals of Mathematical Statistics **22** (1), 79–86 (1951).

[90]R. W. Nero, C. H. Thompson and J. M. Jech, "In situ acoustic estimates of the swimbladder volume of Atlantic herring (*Clupea harengus*)," ICES J. Mar. Sci. **61** (3), 323–337 (2004).

INITIAL DISTRIBUTION LIST

1. Defense Technical Information Center
   Ft. Belvoir, Virginia

2. Dudley Knox Library
   Naval Postgraduate School
   Monterey, California

3. Professor Mary Batteen, Chairman, Code OC
   Department of Oceanography
   Naval Postgraduate School
   Monterey, California

4. Professor John Colosi
   Department of Oceanography
   Naval Postgraduate School
   Monterey, California

5. Timothy K. Stanton, Senior Scientist
   Applied Ocean Physics and Engineering
   Woods Hole Oceanographic Institution
   Woods Hole, Massachusetts

6. Distinguished Professor Ching-Sang Chiu
   Department of Oceanography
   Naval Postgraduate School
   Monterey, California

7. Professor Lawrence Ziomek
   Department of Electrical and Computer Engineering
   Naval Postgraduate School
   Monterey, California

8. Research Associate Professor D. Benjamin Reeder
   Department of Oceanography
   Naval Postgraduate School
   Monterey, California

9. LCDR Benjamin Jones
   Department of Oceanography
   Naval Postgraduate School
   Monterey, California